博士論文

Generation and diagnostics of gas-temperature-controlled high-pressure plasmas at cryogenic temperatures

（ガス温度を室温以下に制御した高圧プラズマの発生と診断）

東京大学大学院新領域創成科学研究科

物質系専攻

宗岡　均

Table of contents

List of figures

Chapter 1

Chapter 2

Chapter 3

List of tables

Chapter 2

Chapter 3

Chapter 1

Introduction

In this thesis, “cryoplasmas”, whose plasma gas temperature (i.e. the temperature of neutral species in plasmas, T_g) are controlled continuously at lower than room temperature (RT), were investigated. This type of plasmas has been developed recently and reported from 2008 [1–4]. The temperature range is between approximately 300 K, which is a typical value of RT, and around 5 K, which is slightly higher than liquid helium temperature. T_g is one of the most important parameters in plasma science and technology, because T_g affects the plasma chemistry and transportation of heavy neutral species including excited species and radicals, and their interaction with condensed-phase materials. However, up to now, the role of T_g in high-pressure plasmas has not been studied sufficiently, and therefore, T_g can be considered as a kind of a “new” parameter in non-equilibrium plasmas. In the new and exotic T_g region of cryogenic temperatures, both phenomena —peculiar to cryogenic temperatures and showing a continuous variation from conventional temperatures higher than room temperature— are expected to appear. To date, our group has reported experimental results specific to cryogenic temperatures, such as the variation of emission species and self-organized pattern formation, and the possibility of the applications of cryoplasmas for materials processing [1–11]. In this thesis, not only the uniqueness of cryogenic temperatures, but also the fundamental role of the parameter of T_g in non-equilibrium plasma chemistry is discussed using cryoplasmas.

On the other hand, plasmas in high-density fluids, such as high-pressure gases, liquids, and supercritical fluids (SCFs), are expected to become established as novel plasma sources possessing a highly non-equilibrium state. In these fluids, the interactions between molecules cannot be ignored. At high-pressure gases, a mobility of negative charged particles was found to decrease abruptly, probably due to clustering of gas molecules [12]. In liquids, solution plasmas, which are gas plasmas generated in a liquid phase, have been studied intensively [13]. Plasmas in an intermediate state between gas and liquid, namely plasmas in SCF, have been also reported. Moreover, in SCF in the vicinity of the critical point (CP), the fluid structure exhibits high local density fluctuations and various phenomena such as transportation display an anomalous behavior near the CP (critical anomaly). Recently, SCF plasmas, in which the density fluctuations are preserved, have attracted much attention, with expectations to provide a unique reaction field [14]. In this thesis, the fundamental mechanisms of the generation of plasmas in high-density fluids with density fluctuations and the motion of charged particles in local density fluctuations, are discussed.

In this chapter, an introduction of this thesis, particularly about gas temperature and plasma chemistry, is described, while the backgrounds of the plasmas in higher-pressure conditions than atmospheric pressure are introduced mainly in section 3.1. A basic description on various temperatures and classification according to temperatures are described

in section 1.1. Role of T_g, which is the most important plasma parameter in this study, and importance of controlling T_g in high-pressure non-equilibrium plasmas are then shown in section 1.2. As a T_g-controlled plasma below room temperature, a “cryoplasma” which is the plasma source in this study are introduced in section 1.3, followed with the purpose of this thesis, which is explained in section 1.4.

1.1 Temperatures and classification of plasmas

1.1.1 Temperatures in plasmas

A plasma is one of phases of matter and has a high energy enough to keep a quasi-neutral ionized state. Since plasmas can be generated by applying energy to gas, a plasma is considered as a phase next to gas and often called as "a fourth phase of matter" followed with solid, liquid, and gas. Even in such a "high energy" plasmas, plasmas having a low "temperature" can be generated, for example, at room temperature and, furthermore, cryogenic temperatures such as 5 K.

In the region of plasma science and engineering, the term "temperature" should be used carefully, because there are many kinds of species in plasmas and they can have different energies, namely, temperatures. While temporal and spatial distributions of a temperature exist in any phases, in addition to the distributions, many kinds of temperatures are defined simultaneously in plasmas.

Plasmas contain charged particles such as electron and ions, and neutral particles such as atoms, molecules, and radicals. We note that the radical is an atom, molecule, or ion that has unpaired valence electrons in plasmas. The translational temperatures of neutral species [plasma gas temperature (T_g)], ions [ion temperature (T_i)], and electron [electron temperature (T_e)] have been considered. In addition, in molecules there are the rotational and vibrational temperatures (T_r and T_v, respectively).

Plasmas, whose all kinds of temperatures are high (typically more than a few thousands of Kelvin) and in local thermal equilibrium (LTE), are called "thermal plasmas" or "equilibrium plasmas". The thermal plasmas are widely used for the applications using huge thermal energies, such as arc welding, thermal spraying, exhaust gas treatment, and nuclear fusion.

Meanwhile, plasmas in non-equilibrium state, in which only T_e is high (typically more than a few thousands of Kelvin) and other temperatures are low (typically less than 1000 K), can be generated and maintained because the mass of electron is more than one thousand times lighter than that of other species. These plasmas are called "low-temperature plasmas" or "non-equilibrium plasmas" and the relationship of temperatures are typically

$$T_e \gg T_i, T_v > T_r \geq T_g. \tag{1. 1}$$

The low-temperature plasmas are widely applied by using the high reactivity and high non-equilibrium state for the various fields such as electronics, material syntheses, and medicine.

Thus, the "temperature" in the last sentence in the first paragraph in this section indicated T_g, not T_e. Those low-temperature plasmas have a high T_e. Actually, plasmas having low T_e are not impossible, such as the space plasmas and ultracold neutral plasmas [15]. However, the generation of such plasmas is not easy on earth. On the other hand, the non-equilibrium plasmas having low T_g and high T_e can be generated much more easily, and therefore the non-equilibrium plasmas can be used for realistic applications.

1.1.2 Non-equilibrium plasmas in high-pressure condition

Applying energy are necessary to generate and maintain plasmas in conditions on the Earth, and plasmas can be generated typically by applying electric field, laser, or heat. In these, applying electric field is most used way because of high controllability, cheap equipment and availability for large volume. When electric field is applied, electron is accelerated and has high energy at first because of its light mass. Basically, at low density (pressure) conditions, non-equilibrium low-temperature plasmas are generated, because energy transfer from electrons to neutral species is low efficiency due to low collision frequency between electrons and neutral species. On the other hand, at high density (pressure) conditions, equilibrium thermal plasmas tend to be generated. Note that when I simply mention the "density" in this dissertation, it refers to the number density of gas atoms and molecules. The typical dependency of T_g and T_e on pressure [16] and the classification of the plasmas are described in Figure 1.1

However, the non-equilibrium plasmas having low T_g and high T_e similar to those in low-density can be generated at high density (pressure) conditions by spatio-temporal restriction of energy application to plasmas. The high-pressure non-equilibrium plasmas have many advantages. For example, since those can be generated with maintaining environment in almost the same as room environment, those can be used for polymer materials including very heat-sensitive biomaterials and can be generated on/in/with liquids such as water, alcohols, and oils. Moreover, the other advantages of the plasmas (especially at atmospheric pressure) are low in cost, because expensive vacuum and cooling equipment are not necessary, and fast in process speed, owing to their high density. Therefore, the high-pressure non-equilibrium plasmas are expected to expand fields of plasma applications and improve the existing plasma applications. In actual, applications of the high-pressure non-equilibrium plasmas in many fields have been studied so far, for example, medicine, agriculture, and environment.

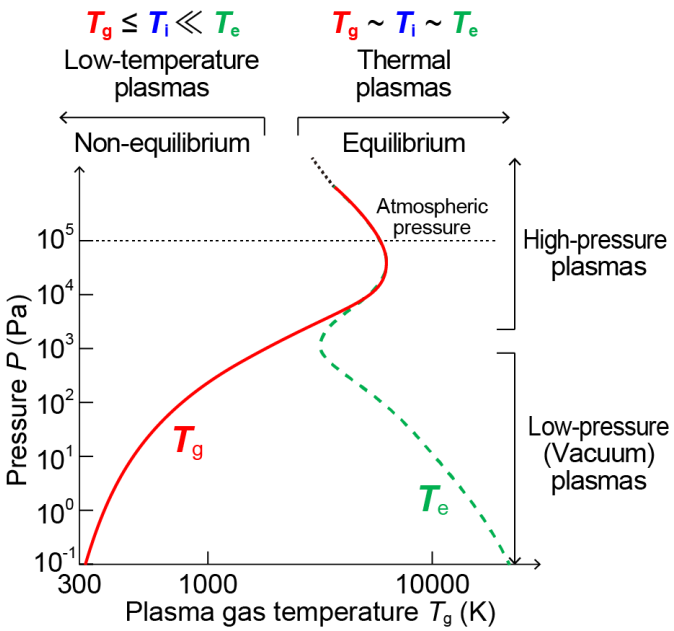

Figure 1.1 The typical dependency of T_g and T_e on pressure and the classification of the plasmas [16].

1.2 Gas temperature in high-pressure non-equilibrium plasmas

At high density (pressure) conditions, the importance of T_g becomes greater compared to that at low density (pressure) conditions. This is due to high collision frequency between neutral species, high total energy of neutral species, and high electron-neutral species collision frequency as shown in Figure 1.2.

In the following, the importance of T_g and the way to control or evaluate T_g are introduced with introducing the effects of the factors mentioned above.

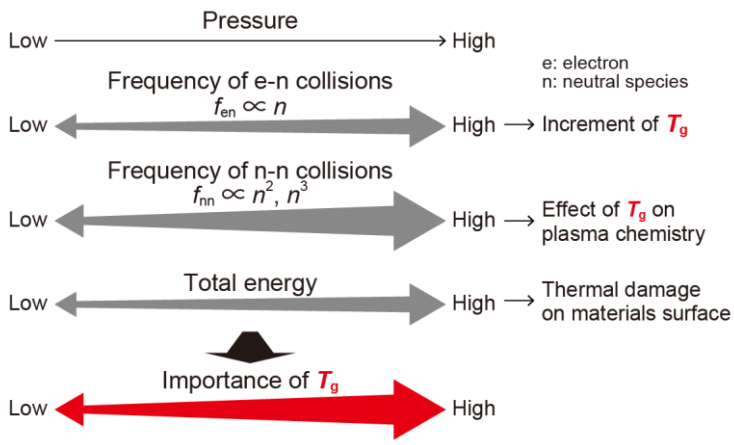

Figure 1.2 Schematic of magnitude of effects of T_g on frequency of electron-neutral species (e-n) collisions, frequency of neutral species-neutral species (n-n) collisions, and total energy depending on pressure. As a result, the importance of T_g in plasma chemistry and processes is significant at high pressure conditions.

1.2.1 Influence of gas temperature on plasma chemistry

Electron temperature T_e has been considered as the most important temperature in various kinds of temperatures in non-equilibrium plasmas. This is because reactions in non-equilibrium plasmas were basically governed by T_e because T_e is much higher than the other temperatures. Figure 1.3 shows electron impact cross sections of various reactions in oxygen (O_2) [17]. Energy to cause inelastic collisions, which accompany a variation of potential energy of collision species, are more than several eV. In O_2, the ionization potential is around 15 eV, energy to cause electron excitations are above approximately 1 eV, vibration excitations are above around 0.2 eV, and rotation excitations are around 0.08 eV. Note that an energy of 1 eV corresponds to a temperature of around 11600 K. When the collision energy is lower than those energies, the collision becomes an elastic collision which do not accompany a variation of potential energy. In the inelastic collisions, mainly the ionization, dissociation, and electron excitation affect a plasma chemistry in whole plasmas. Particles causing these inelastic collisions are in the tail of high-energy side in an energy distribution of high-kinetic-energy particles. In non-equilibrium plasmas, since an average energy of electrons is around 1 eV, there are enough electrons causing inelastic collisions. Therefore, the dependency of the reaction rate

constants on T_e has been taken into account in the estimation of non-equilibrium plasma chemistry and many studies have been conducted to estimate the dependency on T_e so far. On the other hand, there are very few species having enough kinetic energy to cause inelastic collisions other than electron. Particularly, neutral species have low energy in basic, because the neutral species are not accelerated by electric field directly. Therefore, reaction models including T_g in formulas of reaction rate constants are very rare.

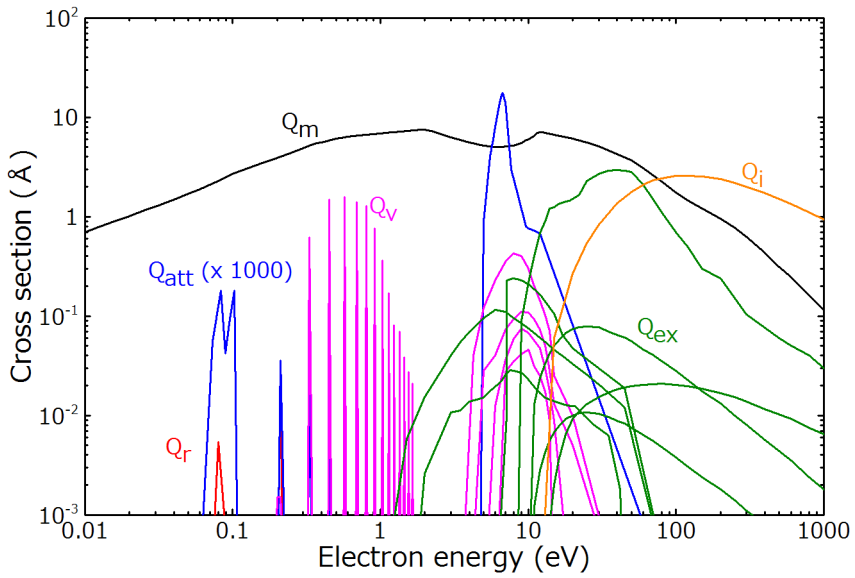

Figure 1.3 Dependency of electron-impact cross sections with O_2 in ground state on electron energy. Data were retrieved from Ref. [17]. The cross sections of momentum transfer (Q_m), rotational excitation (Q_r), vibrational excitation (Q_v), electron excitation (Q_{ex}), electron attachment (Q_{att}), and ionization (Q_i) are indicated.

However, some neutral species, such as radicals, metastable atoms and metastable molecules have a relatively high potential energy (typically several eV to 20 eV) in non-equilibrium plasmas. The atoms and molecules in metastable states show longer lifetime than ordinary excited states because the transition from metastable states to lower levels are optically forbidden. Therefore, these species can be dominant species causing inelastic collisions. At low density (pressure) conditions in conventional low-temperature plasmas, since frequencies of collisions between species having high potential energy and other neutral species are not high, the collision reaction between neutral species are not important. However, the collision frequency between neutral species (f_{nn}) is much higher at higher pressure. Basically, f_{nn} is proportional to 2nd or 3rd power of the number density of neutral species for a two-body collision or a three-body collision, respectively. Therefore, the importance of T_g should not be negligible in high-pressure plasmas. In addition, the high collision frequency of high-energy species with low-energy neutral species can provide a non-equilibrium reaction field. For example, in processes in which reactions are difficult to be stopped on the way to final products once after exceeding activation energy and as a result the reactions occur automatically and quickly in equilibrium state, intermediate products can be obtained by non-equilibrium plasma processes due to the

quick quench reactions of intermediate products. In such plasma reactions, low T_g is important to keep the highly non-equilibrium reaction field.

Therefore, reaction models including T_g in formulas of reaction rate constants should be necessary to describe a non-equilibrium plasma chemistry. However, although such reaction models including the effect of T_g have been developed in ozone generation, almost all reaction models have not included the effect of T_g in high-pressure non-equilibrium plasmas. This is because the effect of T_e is larger than that of T_g in many cases and the breakdown models for high-pressure non-equilibrium plasmas have been developed from those for low-pressure plasmas. However, the effect of T_g can be important to control plasmas precisely and, moreover, T_g can be dominant in some systems such as He-N_2 system. The more detailed discussion about the effect of T_g on plasma chemistry is written in section 2.5.1.

1.2.2 Influence of gas temperature on thermal damage on surface of materials

On the interface of plasmas and solid materials, the materials can be damaged because the energy of plasmas are higher than that of materials. The damages can be divided into mainly three kinds: a damage caused by high kinetic energy of species (mainly charged particles), that by high potential energy of heavy species, and that by low but enough energy of heavy species to damage the material gradually. Of course the first and second damages are important. However, the density of charged particles, which tend to have high kinetic energy, are much lower than that of the heavy species in non-equilibrium plasmas. On the other hand, the third damage is also important at high density (pressure) conditions. This is because even small energy, e.g. less than 1 eV, can affect the solid surfaces, while the energy necessary to cause chemical reactions of dissociation, excitation, and ionization in gases and plasmas are typically more than several eV (see Figure 1.3). For example, the phase transitions in solids such as crystal structure transformation, ferromagnetic transition at Curie temperature, and superconductive transitions occur at low temperatures such as hundreds of kelvins. Moreover, the modification, attachment, detachment etc. of surface bond of polymers can occur around room temperature.

Plasma gas temperature represents the total energy, in other words, enthalpy of high-pressure non-equilibrium plasmas because almost all high-pressure non-equilibrium plasmas have low ionization degree. Whereas the difference of plasma gas temperature and electron temperature in non-equilibrium plasmas is around $10 - 10^3$ times of magnitude, a typical ionization degree in high-pressure non-equilibrium plasmas is low, for example, 10^{-8} for atmospheric-pressure plasma jets. Therefore, although an individual electron has much higher energy than an individual neutral species does, the whole energy of electrons are not dominant in high-pressure non-equilibrium plasmas. This total energy is important in the application of high-pressure plasmas for materials processing, because a heat flux of the neutral species is high because of its high density. Even if the average energy of neutral species, which is indicated as T_g, is too low to damage materials, the accumulation of the energies of neutral species can cause a damage. Moreover, a small proportion of neutral species having a high kinetic energy in statistical energy distribution cannot be ignored owing to a high flux of neutral species to a materials surface. Thus thermal damages on a surface of materials can be brought in contact with plasmas by impacts of neutral species, as well as impacts of low-density high-energy species such as electrons and ions. Importance of the problem of thermal damage depends on materials facing plasmas.

Particularly when the materials are heat-sensitive polymers including biomaterials, the plasma gas temperature is necessary to be controlled precisely. The cooling equipment of substrates and electrodes has been used to prevent the thermal damages in conventional plasma applications, but the approach is not easy to be used for skins or inward organs, and often not enough for heat-sensitive biomaterials. Therefore, the enthalpy of plasmas should be decreased in the applications to biomaterials. In addition, controlling the temperatures of not only substrates but also plasmas may allow us to develop more precisely controlled plasma processes. Plasma is often located enough far from materials to reduce thermal damages. However, in such a geometry, only activation species having a long lifetime can reach materials and this can be a limitation of plasma applications. A problem that the reactive species are easy to be quenched in high-pressure condition because of the short mean free path is important in high-pressure plasma application as a remote plasma source. Moreover, even if we use a high-pressure non-equilibrium plasma as a remote plasma source to prevent the thermal damage to target materials, it may be inevitable to discuss the effect of T_g on chemistry in plasmas as well as that on materials surface.

1.2.3 Control of gas temperature

At high pressure, since the collision frequency between electron and neutral species (f_{en}) are higher (f_{en} is approximately proportional to the number density of neutral species in constant electron density conditions), the energy that electrons initially have can transform to neutral species easily and therefore, T_g tends to increase and neutral species having high energy such as radicals can be generated easily.

When power is introduced into high-pressure plasmas continuously, T_g increases rapidly to more than 1000 K and plasmas become thermal plasmas. The heat flux of thermal plasmas can beyond an order of W/cm^2 or kW/cm^2 [18] and these values corresponds to the heat flux of the artificial satellite in re-entry to the Earth, for example, that of the Japanese space probe Hayabusa in re-entry was estimated as more than 1.5 kW/cm^2 [19]. Therefore, in the application using the high thermal energy, the efforts such as reducing an input power, setting a large-size cooling equipment, and confining plasmas, are necessary to prevent the thermal damage.

The most effective way to reduce the inclement of T_g in high-pressure plasmas is restricting input power temporally, when such high thermal energy are not necessary in the application. To generate high-pressure non-equilibrium plasmas, pulse power sources are often utilized and/or the self-power-confinement geometry such as dielectric barrier discharge (DBD) in which one or more dielectric layers are inserted between electrodes. Microplasmas are also used to prevent T_g increase. Here, microplasmas are defined as plasmas which are spatially confined to dimensions of 1 mm or less [20]. In microplasmas, thermal energy can escape from plasmas easily due to their large specific surface areas. In addition, forced gas flows and cooling electrodes are used. At atmospheric pressure plasmas, T_g can be controlled on some level [21] as shown in Figure 1.4. As a result, T_g can be restricted less than around 1000 K. While an approximate T_g control are necessary to prevent a thermal damage to not heat-sensitive materials in conventional low-temperature plasma applications, a strict control of T_g has not been conducted so far. However, as mentioned in previous sections, controlling T_g becomes important to apply high-pressure plasmas to heat-sensitive materials or to achieve more precise control of plasma processes. To do that, the above methods should be

pursued and the evaluation of T_g is also necessary.

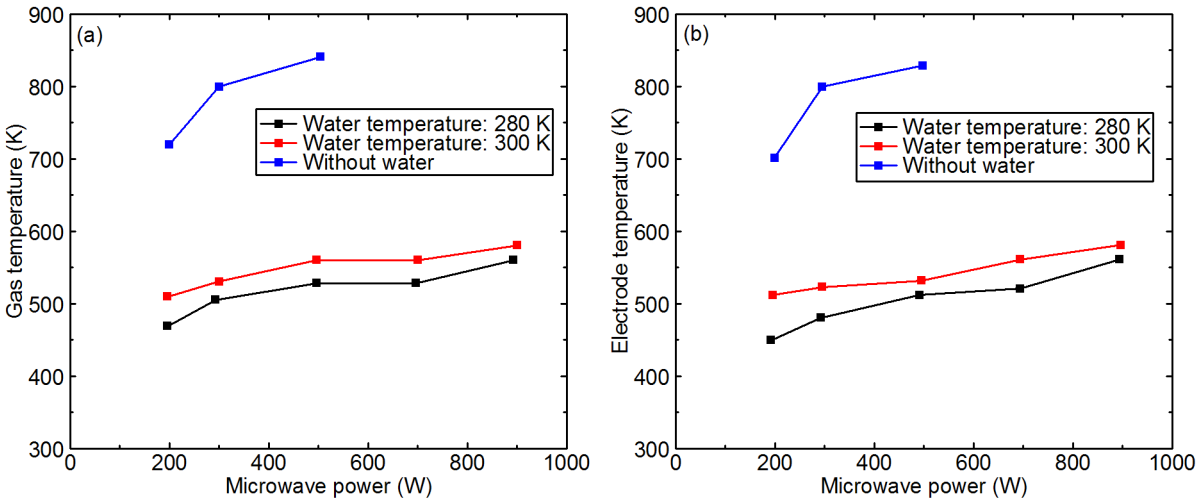

Figure 1.4 (a) Dependency of T_g and (b) dependency of electrode temperature on microwave power. Both temperatures depends on the temperature of coolant water. The small difference between both temperatures implied that T_g can be controlled in the order of a few kelvins by monitoring electrode temperature [21].

1.2.4 Evaluation of gas temperature

To achieve a precise control of T_g, restriction of an increase of T_g within an allowable range or evaluation of the increase of T_g are necessary. To evaluate T_g, many methods have been used and in this section, combination of contact-type thermometers and thermal simulation, analyses of optical emission of plasmas, and laser metrologies are introduced.

(a) Contact-type thermometers and thermal simulations

Since almost all high-pressure non-equilibrium plasmas are the microplasmas, the direct measurement of T_g without disturbing plasmas is difficult. Therefore, the combinations of the measurements of gas temperature by contact-type thermometer and thermal simulations have been widely used. This method is used in this study and introduced in section 2.2.2.1.

(b) Analyses of optical emission spectroscopy (OES)

For high-pressure plasmas having relatively high-T_g, T_g may be measured by infrared radiation thermometer. However, the resolution of the measurement is not high compared to other methods and the radiation thermometer is difficult to be used for relatively low T_g plasmas because the energy flux of thermal radiation are proportional to T^4 (Stefan-Boltzmann law) and the number density of plasmas are much lower than the solids behind the plasmas. In

addition, the measurement of T_g can be done by analyzing atomic or molecular emission peaks. For the relatively high-T_g plasmas, evaluation of Doppler broadening is simple method, but the resolution are not elaborate, similar to infrared radiation thermometers. The most widely used evaluation method of T_g for high-pressure non-equilibrium plasmas are evaluation of rotation temperature of diatomic molecules by analyzing rotation distributions of molecular spectrum. In high-pressure plasmas, rotation temperature T_r are regarded as almost equilibrium to translational temperature T_g and the optical emission spectroscopy is easy to be measured. However, at cryogenic temperatures, the assumption of equilibrium between T_r and T_g may not be valid, although our group has tried to use this method. The resolution of T_g in this method depends on the equipment of spectroscopy and the focused emission peak. The resolution is, for example, reported to be ± 20 K for N_2 (337 nm, $C\ ^3\Pi_u - B\ ^3\Pi_g$) in the equipment with wavelength resolution of $\Delta\lambda$ = 0.015 nm, ± 10 K for OH (308 nm, $A\ ^2\Sigma^+ - X\ ^2\Pi$) with $\Delta\lambda$ = 0.04 nm [22].

(c) Laser metrologies

Similar to OES, T_g can be estimated by Doppler broadening in the signal of an interaction of laser and plasmas in relatively high T_g plasmas. Moreover, the value of T_g can be estimated by laser interferometry (LI). LI can measure the refractive index of plasmas, and the refractive index varies with both electron density and gas density. Therefore, laser interferometry can measure both electron density and gas density. The method of LI is introduced in section 2.2.1.1.

1.2.5 T_g variation keeping pressure or density

The variation of T_g causes the variation of pressure with keeping constant density or the variation of density with keeping constant pressure. The operation of the variations of both pressure and density to keep another parameter such as n-n collision frequency f_{nn} is also considerable. The relationship among T_g, n, and P are described in the state equation, for example,

$$P = nkT_g \tag{1. 2}$$

for ideal gases. In this section, Equation (1. 2) is used to make discussion simple. What operation is the best to investigate the influence of the variation of T_g depends on the purpose of the study. With the variation of T_g, both the kinetic energy of the neutral species and the velocity (leading to collision frequency between neutral species) vary. In addition, a state of an ambient fluid changes with T_g due to the phase change and the variation of vapor pressure.

Three operations of T_g variation are discussed. Basically the parameters other than those varying with T_g, such as electric field, electron density and electron temperature, are constant in the following discussion.

(1) Constant density (n: constant, $P \propto T_g$)

In this condition, the substantive f_{en} does not change because of constant n, and the substantive collision energy between electron and heavy species does also not change due to much higher T_e than T_g. The electron swarm parameters are normalized with the reduced electric field (E/n) and, in this condition, E/n can maintain easily at different T_g conditions by keeping E constant. These mean that the collision between electron and neutral species are normalized.

On the other hand, the collision frequency and energy between neutral species vary with the variation of T_g. In addition, a breakdown voltage (U_B) can be constant in the same electrodes because it is normalized to a product of n and d in parallel plate electrodes (see section 3.1.4.1).

(2) Constant n-n collision frequency (f_{nn}: constant, $n \propto T_g^{-0.5}$, $P \propto T_g^{0.5}$)

To achieve the constant f_{nn}, both n and P should vary with T_g variation. The collision frequency f_{nn} are expressed as [23]

$$f_{nn} = nv\sigma(v) \tag{1. 3}$$

where v is the velocity of the neutral species and $\sigma(v)$ is the collision cross section of the n-n collision depending on v. Since v is approximately proportional to $T_g^{0.5}$, n should be proportional to $T_g^{-0.5}$ to keep $n \times v$ constant. In constant $n \times v$ conditions, the variation of σ depending on T_g can be discussed.

In addition, when E changes as proportional to $T_g^{-0.5}$, E / n is also constant, which means that the collision between electron and neutral species are normalized. However, the value of U_B changes in this condition because n changes with T_g variation.

(3) Constant pressure ($n \propto T_g^{-1}$, P:constant)

While the control of pressure does not have a large meaning in plasma physics and chemistry, it is important in the interaction of materials or liquids, particularly for those affected by pressure such as compressive materials such as biomaterials, piezoelectric materials, and liquids having high vapor pressure. In addition, in the application, when the pressure is atmospheric pressure, the operation is easy.

In this study, in order to investigate the T_g effect on the plasma chemistry with a constant reduced-electric-field (E/n) condition, we chose the density-fixed operation in Chapter 2.

1.3 Cryoplasmas

1.3.1 Definition and properties of cryoplasmas

The typical T_g range of the conventional high-pressure non-equilibrium plasmas has been from room temperature (~300 K) to 1000 K. Since this temperature range was approximately 0.5 order of magnitude, the effect of variation in T_g has not been easy to be detected clearly. Therefore, T_g range was tried to be expanded in this study to discuss and clarify the effect of T_g in high-pressure non-equilibrium plasmas. While plasmas are thermalized and become thermal plasmas in the T_g range higher than that of conventional non-equilibrium plasmas, plasmas are still non-equilibrium in lower T_g range.

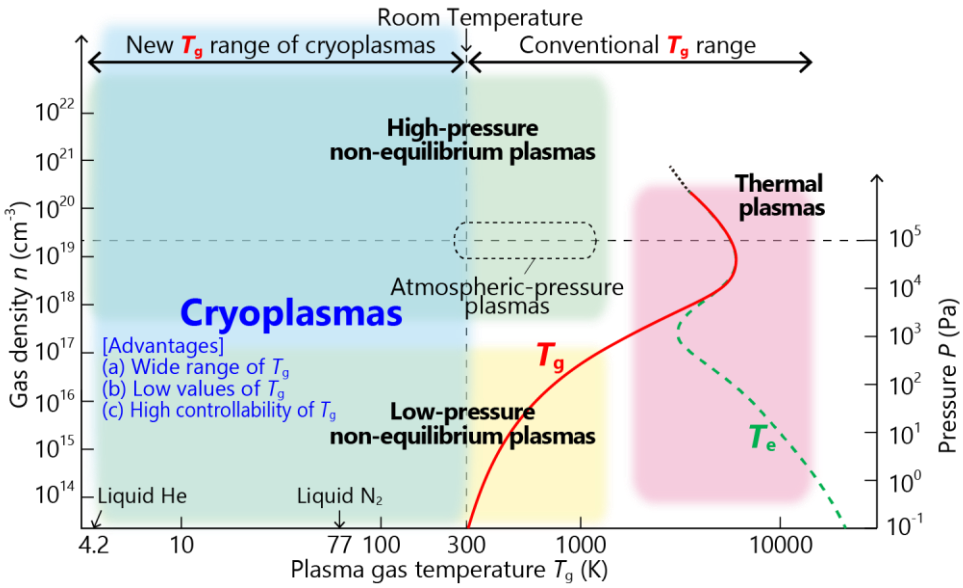

Figure 1.5 The temperature and gas density region of cryoplasmas with the conventional plasmas of high-pressure non-equilibrium plasmas including atmospheric-pressure plasmas, low-pressure non-equilibrium plasmas, and thermal plasmas. Cryoplasma covers the new T_g range for plasma processes, and the advantages of cryoplasmas are also indicated. Cryoplasma is a class of non-equilibrium plasmas. The right axis indicates the pressure corresponding to the gas density at 300 K and the relationship between gas density n and pressure P varies depending on T_g. The linearity between n and P are not valid at high pressures in which the assumption of ideal gas are not valid.

In this study, cryoplasmas were used as plasmas having T_g in such a lower temperature range. Cryoplasmas are defined as plasmas whose T_g can be controlled below room temperatures (RT). The temperature range of cryoplasmas and conventional plasmas are indicated in Figure 1.5. The T_g range are almost two orders of magnitude. As a prototype of cryoplasmas, Figure 1.6 shows that the photographs of the dielectric-barrier-discharge (DBD) atmospheric-pressure microplasma jet near RT and the prototype cryoplasma jet, and the indications of RT and T_g of them measured by the

thermocouples [1]. The cryoplasma was covered by frost because the electrodes were opened to atmosphere. The cryoplasmas have been generated from 5 to 300 K of T_g. Although there have been the studies on the plasmas below cryogenic environment below RT which conducted around specific coolant temperatures such as 4.2 K of liquid He from the view point of fundamental physics such as atomic and molecular physics, there have been no other plasmas whose T_g can be controlled continuously below RT so far. Therefore, the cryoplasma's T_g range (5 – 300 K) can be considered as the novel and third T_g range following to the T_g range of thermal plasmas (> 1000 K) and that of low-temperature plasmas (300 – 1000 K).

Cryoplasmas have advantages related to T_g, such as (a) wide range, (b) low values, and (c) high controllability of T_g. Due to (a) the wide range of T_g, the effects of T_g on various phenomena can be discussed by varying T_g dynamically in cryoplasmas. It is expected that the effects of variations unique in (b) the low temperature range emerge, such as quantum effects and phase transitions such as gas-liquid phase transitions at boiling temperature and the transition of superconductivity. Moreover, by using (c) the controllability of T_g, heat-sensitive phenomena such as density fluctuations near the gas-liquid critical point can be generated. In addition to the basic study, the applications using these advantages are expected.

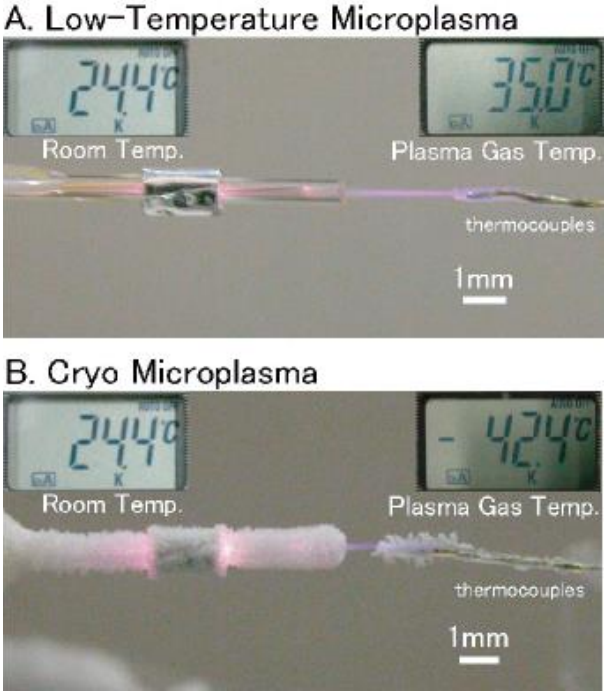

Figure 1.6 Photographs of (a) the dielectric-barrier-discharge (DBD) atmospheric-pressure microplasma jet near RT and (b) the prototype of cryoplasma jet [1]. The upper-left of each photographs shows the indications of room temperature (Room Temp.) and the upper-right are T_g of each plasma jet, measured by the thermocouples located approximately 3 mm from the front edge of glass tube.

1.3.2 Previous studies of cryoplasmas

Cryoplasmas are expected to hold promise for new plasma processes based on their advantages, e.g. for the treatment of heat sensitive materials such as biomaterials, nano-porous structures having a large surface area, and frozen materials. For example, it has been reported that the effective reduction of T_g reduces the damage due to penetrations of oxygen radicals in nano-porous low-*k* materials during ashing process [8]. Figure 1.7 shows the distributions of the ratio of carbon atom to oxygen atom and the density increase in the low-*k* substrates treated by oxygen plasmas. They were measured by (Scanning Transmission Electron Microscope – Electron Energy Loss Spectroscopy: STEM-EELS) and (X-ray refractivity: XRR), respectively. The low ratio of C/O and the large increase of density mean that the low-k materials were damaged. These were caused by the displacement of alkyl to atomic oxygen due to the attack of atomic oxygen radicals and the densification due to the relaxation of the nano-porous structures. In addition, the region, where there is no data at small normalized depth, means that the shrinkage of the low-*k* material due to the densification and etching due to the plasma treatment. In conclusion, Figure 1.7 indicates that, although the damage degree of the surface of the low-*k* material was higher, the damage depth of low-*k* materials caused by oxygen atom radicals in plasmas could be suppressed one-third at T_g = 200 K compared to that at T_g = 300 K. Figure 1.8 shows the schematic of the mechanism of the damage reduction in cryoplasma ashing process [24]. The reduction of the damage is caused by the effective trapping and recombination of oxygen radicals near the interface between low-*k* materials and plasmas, due to the high sticking probability and low diffusion coefficient on the surface in the low temperature. It is suggested that the ease of the penetration of atomic oxygen into nano-porous materials and its T_g dependency could be evaluated using a non-dimensional parameter of Thiele modulus [8].

Not only from the engineering view point, but also from the fundamental plasma physics and chemistries, cryoplasmas have been investigated. The fundamental studies of cryoplasmas are useful to understand the effect of T_g on plasma chemistry of not only cryoplasmas, but also high-pressure non-equilibrium plasmas in general. This is because the T_g range of non-equilibrium plasmas can be expanded from 0.5 order to 2 – 3 order by using T_g.

The cryoplasmas have been developed using jet-type and parallel-plate-type DBD electrodes. In jet-type DBD plasmas, the increase of T_g have been estimated to be below a few Kelvins in a low voltage conditions by a thermal simulation as shown in Figure 1.9(a) [1]. Moreover, by reducing the size of plasmas, the increase of T_g can be smaller, allowing us to control T_g more strictly. For example, Figure 1.9(b) presents that, when the radius of the plasma jet was 0.8 mm and the input power was 48 mW/cm^3, the maximum increase of T_g was estimated to be less than around 1 K even at 5 K, where the T_g can increase easily due to the small specific heat [25].

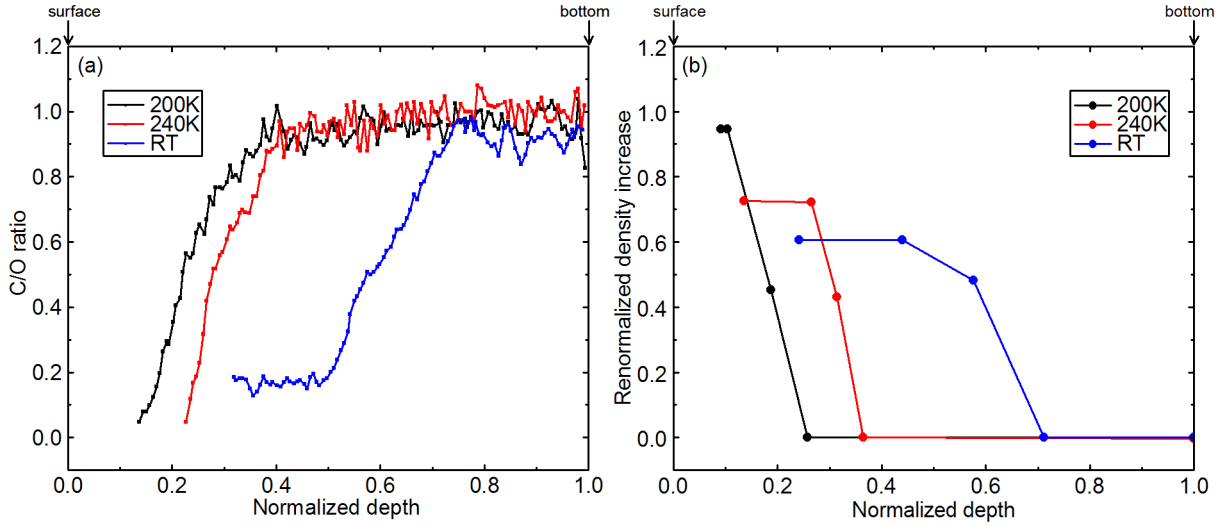

Figure 1.7 Distributions of (a) ratio of carbon atom to oxygen atom (C/O) and (b) density increase in the low-*k* substrates treated by oxygen plasmas. They were measured by Scanning Transmission Electron Microscope – Electron Energy Loss Spectroscopy (STEM-EELS) and X-ray refractivity (XRR), respectively. The low ratio of C/O and the large increase of density mean that the low-*k* materials were damaged. The zero of horizontal axis means the location of the surface of pristine. The region where there is no data at small normalized depth (at left side of the figures) means that the thickness of the substrates decreased, owing to the shrinkage of the low-*k* material due to the densification, and to the etching by plasmas.

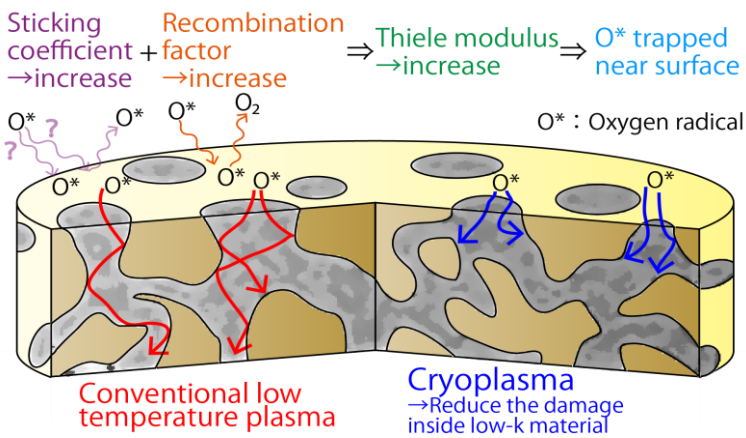

Figure 1.8 Schematic of the mechanism of the damage reduction in cryoplasma ashing process. The yellow porous materials indicates a nano-porous material and the penetration of the atomic oxygen radical (O*) into the material at conventional low temperature plasma process near or higher than room temperature and cryoplasma process are described. [24]

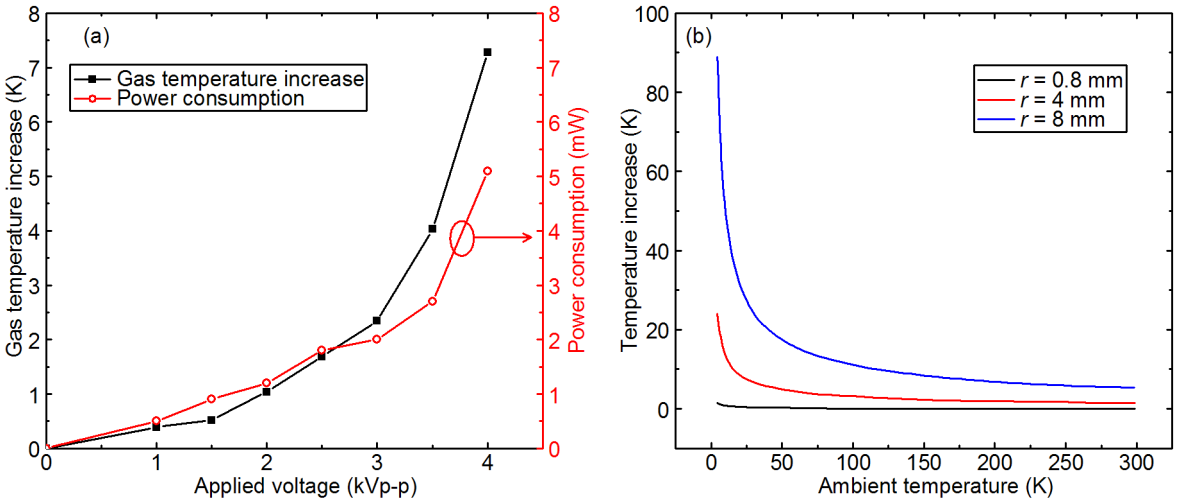

Figure 1.9 (a) Dependencies of gas temperature increase and power consumption on applied voltage in atmospheric pressure jet at room temperature [1]. The geometry of the electrodes and the thermocouples were the same as Figure 1.6. The temperature increase was estimated by thermal simulation using the measured temperature by thermocouples located from 3 mm from the edge of the glass tube. (b) T_g increase from the ambient temperature in cryoplasma jet indicated in Figure 1.11, and its dependency on the inner radius of the glass tube [25]. The input power density was fixed at 48 mW/cm^3, which was typical value of the cryoplasma jet.

The cryoplasmas have been investigated by the observation of physical appearance and the measurements of current (I) and voltage (U) waveforms and optical emission spectroscopy (OES). From the measurement of I and U waveforms, the dependency of electron density (n_e) and T_e at atmospheric-pressure (isobaric) conditions were estimated [7]. The results indicated that average n_e and T_e were $10^9 - 10^{11}$ cm^{-3} and 1 – 15 eV [1,7] as shown in Figure 1.10, respectively, and they were equivalent to the conventional non-equilibrium plasmas. The difference between T_e and T_g was 2 – 4 digits and it was at most two digits larger than conventional non-equilibrium plasmas. Therefore, cryoplasmas were confirmed to be in significantly non-equilibrium state. In the studies, the Coulomb coupling parameter (Γ) was also estimated and the values of Γ increased double digit below 60 K, although the values were still within the range of "weakly-coupled plasmas". The parameter Γ is defined as the ratio of Coulomb energy to thermal energy in the interaction between charged species, and the plasmas are called as "weakly-coupled plasmas" when the former is smaller than the latter. In the region increasing Γ, it is implied from the discussion on the second virial coefficient that Van der Waals interaction cannot be ignored [7].

The variation of discharge modes in DBD electrodes depending on T_g have been confirmed by measurements of I and U waveforms and OES. The discharge modes in helium were changed with decreasing T_g [2,5]. Although the transition temperature were not the same in different papers, the transition order was almost the same, i.e., with decreasing T_g, discharge modes transited from filamentary discharge mode around RT, to atmospheric-pressure glow discharge, and to atmospheric-pressure Townsend discharge.

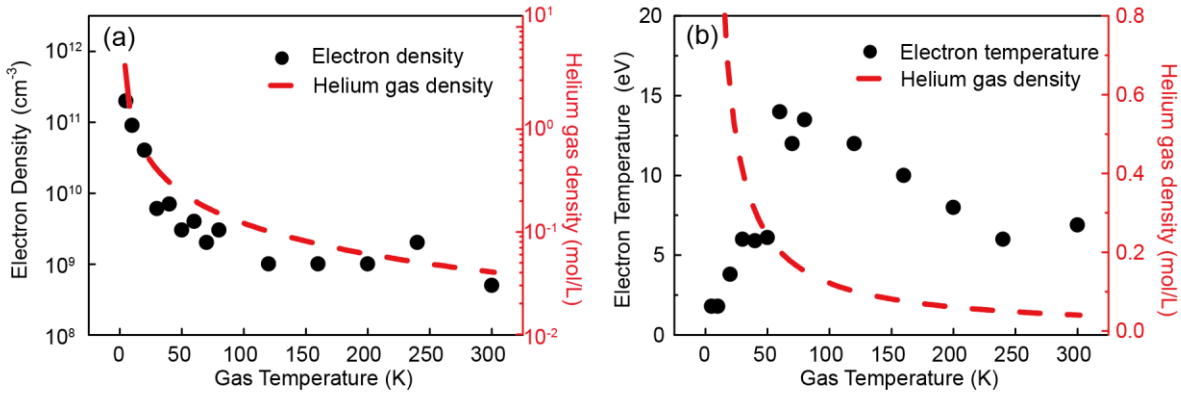

Figure 1.10 (a) Electron density (n_e) and (b) electron temperature (T_e) in cryoplasma jet with helium gas density at each plasma gas temperature which is almost the same as the ambient temperature [7]. The values of n_e and T_e were estimated from measured current and voltage waveforms and swarm parameters of electron (see section 2.5.3). The helium gas density increased with decreasing T_g due to constant pressure of the atmopheric pressure.

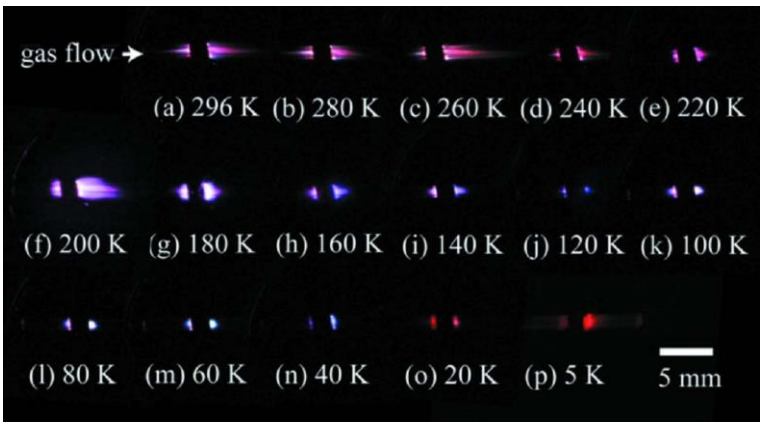

Figure 1.11 Images of generated helium cryoplasma jet at temperatures ranging from 5 to 296 K at the atmospheric pressure [3]

It has been reported that the emission colors of cyoplasmas varied depending on T_g (Figure 1.11) [3]. The emission color is ruled by the emission spectra of plasmas. In OES, drastic variations of emission species depending on T_g was observed as shown in Figure 1.12 [7]. This was mainly owing to the variation of vapor pressures of air impurity species. Below 40 K, air impurities such as N_2 and O_2 were almost condensed and, as a result, the emissions only from He and He_2 existed. This indicates that the He plasmas including impurities changed to the extremely pure He plasmas below 40 K. In addition, not only the species but also the strength of optical emissions varied with T_g. Therefore, it is implied that the variation of species in plasmas and/or the variation of reaction rate constants lead to the variation of plasma chemistry. Moreover, from time-resolved OES (TR-OES), the timings showing maximum in the emission strength of impurity species were different from those of He species only at cryogenic temperatures (Figure 1.13) [6]. This implied that the variation of plasma chemistry occurred due to the variation of reaction rate constants with T_g.

In addition, the unique self-organized pattern formed depending on T_g in the studies using parallel-plate DBD electrodes. There have been two types of cryoplasma studies, depending on whether we fix the gas pressure P [operation (1) in section 1.2.5] or gas number density n [operation (3)] during the T_g decrease, and our cryoplasma chambers can be operated in both. The self-organized pattern formation in the cryoplasma was investigated in both pressure-fixed [2,4,5] and density-fixed [9,11] operations. While the self-organization in DBD electrodes attract much attention as an example of dissipative structure, the transition between ordered phase and homogeneous phase owing to T_g was reported for the first time in cryoplasmas. Moreover, the unique pattern formation consisting of self-organized dark spots, which was hardly observed at RT, was reported in extremely pure He cryoplasmas below 40 K, as indicated in Figure 1.14.

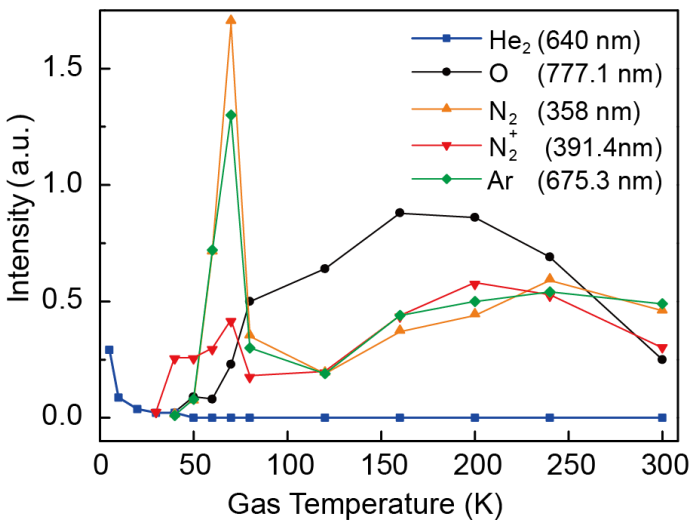

Figure 1.12 Emission intensities of He_2 (640 nm), O (777.1 nm), N_2 (358 nm), N_2^+ (391.4 nm), and Ar (675.3 nm) as a function of T_g [7]. The emission intensities were normalized with respect to the emission intensity of He (706.5 nm) [7].

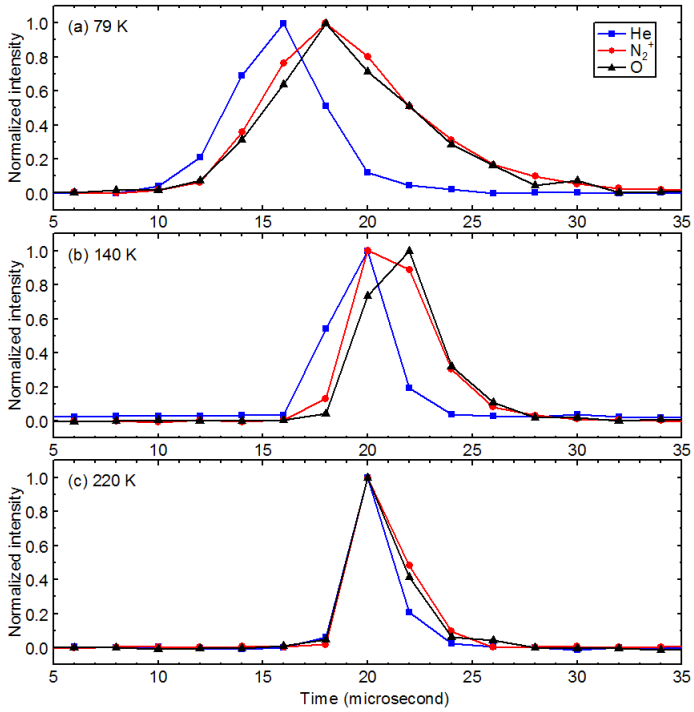

Figure 1.13 Time-resolved optical emission intensities of He cryoplasma including small amount of impurities with parallel-plate dielectric barrier discharge at (a) 79 K, (b) 140 K, and (c) 220 K [6]. The vertical axes are normalized intensity with respect to the maximum of each emission peak.

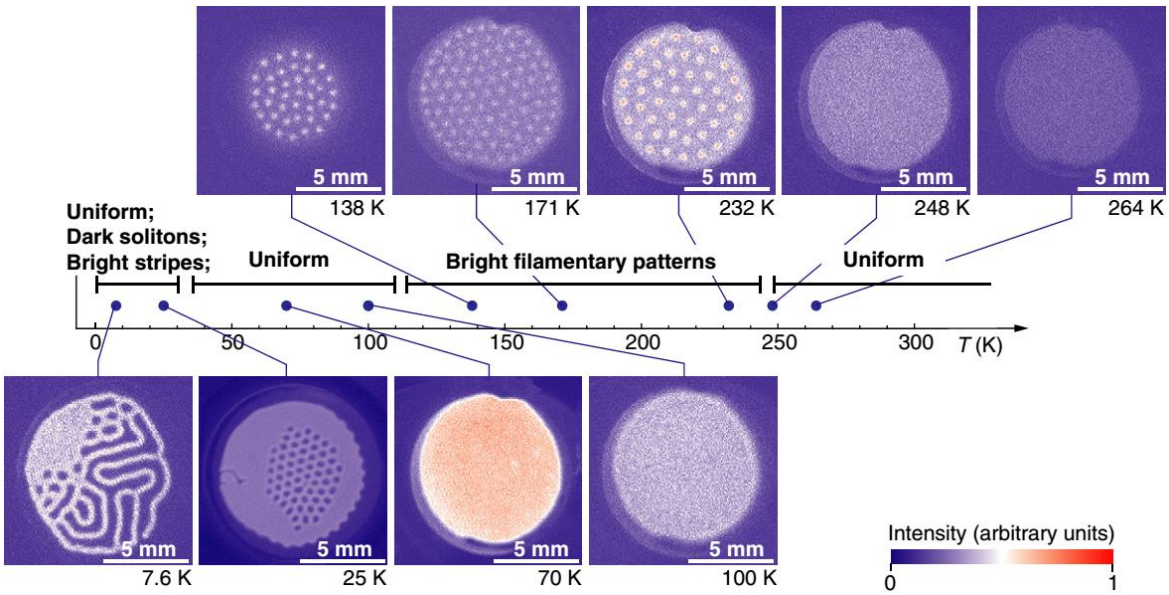

Figure 1.14 Images of cryoplasmas generated at temperature ranging from 264 to 7.6 K. The intensities in the original black-and-white images are mapped to a color lookup table, which allows us to improve the visibility of the features of the different discharges [11].

1.3.3 Remained issues in cryoplasma study

As introduced above, various T_g-dependent phenomena have been confirmed. The influence of the phase change of ambient gases due to varying the ambient temperature on cryoplasma physics and chemistry has been discussed qualitatively, for example, the drastic variations of plasma colors and emission species were suggested to be caused by phase change of impurity species. However, the mechanisms of the T_g-dependencies have not been investigated in detail so far. In particular, the influence of the variation of T_g itself, such as the variation of kinetic energy and the collision frequency, has not been discussed in detail. Therefore, the influence of the variation of T_g and the accompanying phenomena such as the phase change are expected to be discussed more in detail.

In addition, the fundamental studies in another field using the characteristics of cryoplasmas have not been conducted. Since cryoplasmas allow controlling the T_g, temperature-sensitive phenomena such as the density fluctuations near the CP can be maintained in cryoplasmas. Moreover, the development of cyoplasmas using other gases than He and the applications of cryoplasmas to materials processing have been expected.

1.4 Purpose

The purposes of the studies in this thesis are (A) to investigate the role of T_g in plasma chemistry, and (B) to clarify the role of the high-density condition and the density fluctuations in electrical breakdown, which precedes the generation of plasmas in such conditions. By accomplishing these goals, a better understanding of high-pressure non-equilibrium plasma chemistry and a more precise control of plasmas in high-density fluids is expected to be realized. I think that these points are important for realizing applications based on high-pressure non-equilibrium plasmas for materials processing or other fields, as well as answering fundamental questions related to plasma physics and chemistry.

For these purposes, the advantageous properties of the cryoplasmas were utilized. Ranges of the plasma gas temperature T_g and gas density n for each chapter are indicated in Figure 1.15. The advantage of cryoplasmas, "the wide range of T_g [(a) in Figure 1.15]" was used in Chapter 2 to discuss the variation of plasma chemistry, and "high controllability of T_g [(c) in Figure 1.15]" was used in Chapter 3 to generate plasmas in the conditions near the CP in gas, liquid, and supercritical fluids (SCFs). Both in Chapter 2 and 3, the helium (He) was used because of many advantages: (i) it is one of the most widely used gases for high-pressure plasmas, (ii) the temperature range in its gas phase (> 4.2 K) is the largest, (iii) it is easy to be modeled because of monatomic, (iv) the extremely pure condition without any impurity gases can be obtained, and (v) due to its light mass the experiments were conducted without damages on the electrode surface.

In Chapter 2, to achieve the purpose (A), diagnostics of cryoplasmas were conducted using laser metrologies and OES at first. Then, a reaction model taking into account the dependency of elemental reactions on T_g was developed. Finally, the model was used to discuss the mechanisms of the experimental results and the plasma chemistry. The goals were to show the importance of T_g and how important in non-equilibrium plasma chemistry, and to pull the trigger of further studies on non-equilibrium plasma chemistry taking into account T_g for other gas compositions.

In Chapter 3, to accomplish (B), the generation of plasmas in such high-pressure and/or density-fluctuating fluids were investigated. At first, elaborate experiments of breakdown voltage (U_B) measurements were conducted, and then, electrical breakdown models were developed. Plasmas in high-density fluids and plasmas in fluids with high-density fluctuations has been expected to be applied for new plasma applications [14]. In this chapter, He (critical temperature: T_c = 5.2 K [26]) was used to conduct elaborate experiments without damages of electrodes. Therefore, the cryoplasma technique was essential to conduct the experiments in Chapter 3. The goals of this topic were to reveal the electrical breakdown mechanisms in high-pressure gases, liquids, and SCFs for further better control of plasmas in such fluids, and to make a model describing electron motion in fluids with high-density fluctuations for revealing reaction dynamics in density-fluctuating fluids.

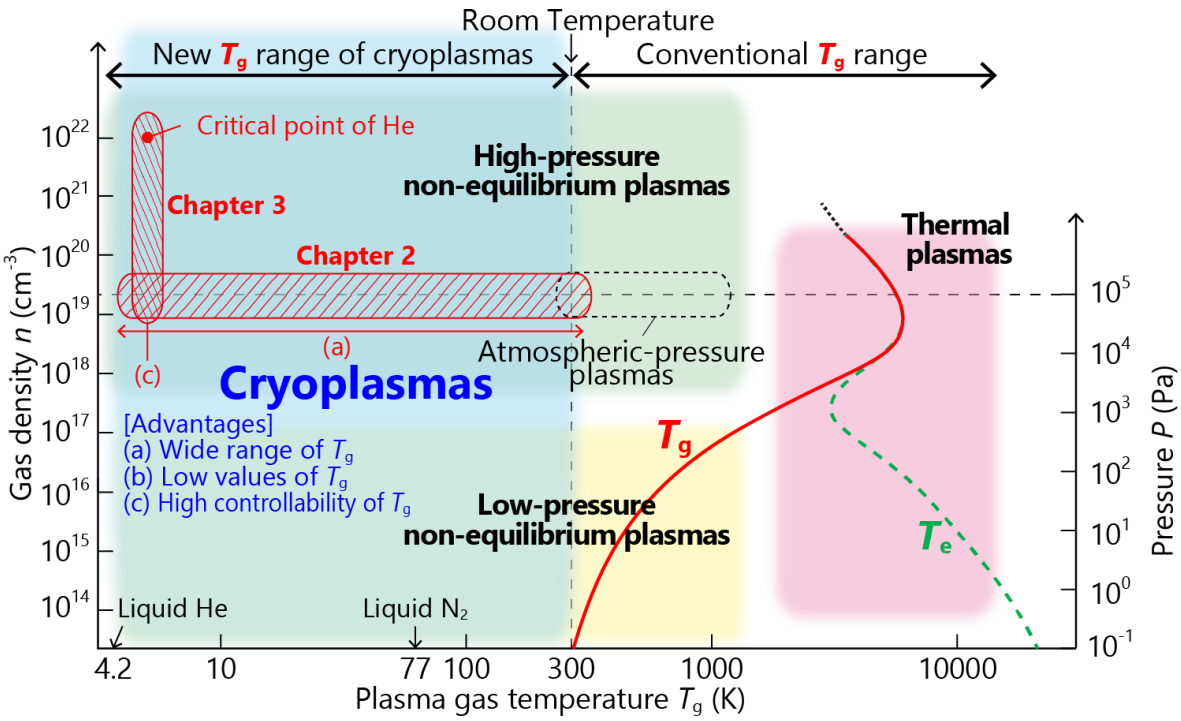

Figure 1.15 Plasma gas temperature and gas density domains of chapters 2 and 3 with the T_g-n diagram indicated in Figure 1.5.

Chapter 2

Gas-temperature-dependent plasma chemistry

In this chapter, to investigate the role of T_g in plasma chemistry, fundamental diagnostics of He cryoplasmas and discussion using my developed reaction model are presented. In the investigation of cryoplasmas in wide T_g range from 5 to 300 K, both the drastic variation of plasma chemistry due to phase changes (the boiling temperatures for impurity species and characteristic temperatures are shown in Figure 2.1) and the gradual variation due to continuous variations of collision parameters (collision frequency, collision cross section, etc.) and kinetic energy are expected. The results and discussions of this study allowed us to describe the dependency of plasma chemistry on T_g not only in cryoplasmas, but also in high-pressure non-equilibrium plasmas widely.

At first, the experimental setup and conditions are introduced in section 2.1. In this study, two chambers and three kinds of electrodes were used. The values of T_g in cryoplasmas for each electrodes were evaluated by a laser heterodyne interferometry (LI) and a thermal simulation in section 2.2. Then, experimental procedures and results of diagnostics using optical emission spectroscopy (OES) and laser absorption spectroscopy (LAS) are introduced in sections 2.3 and 2.4, respectively. In section 2.3, two types of OES, i.e., time-integrated optical emission spectroscopy (TI-OES) and time-resolved OES (TR-OES) were conducted. Changes in emission species depending on T_g and time-dependent phenomena related to emission intensities peculiar to cryogenic temperatures were observed. The diagnostics of LAS were conducted to measure the density and the lifetime of metastable He atom (He^m, 2^3S_1) in section 2.4. In section 2.5, the 0-dimensional reaction model developed in this study is introduced. The feature of the reaction model is that it includes the term of T_g in reaction rate constants of elemental reactions and diffusion coefficients. The discussions using the reaction model for the results of OES and LAS are presented in section 2.6.1 and section 2.6.2, respectively. In addition, the dynamic variations of plasma chemistry in He/N_2 and quench reactions of He^m in $He/N_2/O_2/H_2O$ depending on T_g are discussed in section 2.6.3. Finally, in section 2.7, the results and discussions on T_g-dependent plasma chemistry are summarized.

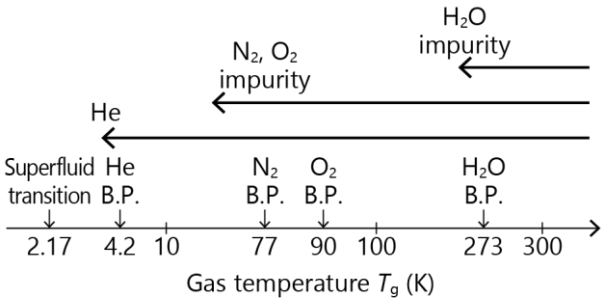

Figure 2.1 Diagram of temperature ranges for the experimental conditions of cryoplasma generation with information of boiling point (B.P.) temperatures for impurity molecules and characteristic temperatures for He.

2.1 Experimental setup and conditions

2.1.1 Plasma chamber

In this study, we used He because it is one of the most widely used gases for high-pressure plasmas and the temperature range in its gas phase (> 4.2 K) is the largest. In addition, the reactions are relatively simple compared to other species due to monatomic and light weight atom.

We used two types of plasma chambers, namely "LN_2 cryoplasma chamber (LN_2 chamber)" and "4 K cryoplasma chamber (4 K chamber)". These chambers allowed us to control the temperature inside the chambers at cryogenic temperatures precisely (better than ± 0.5 K in LN_2 chamber and ± 0.1 K in 4 K chamber). The main differences between them were in the system of cooling and the temperature range.

2.1.1.1 LN_2 cryoplasma chamber

The schematics and the photograph of the plasma chamber are presented in Figure 2.2. Figure 2.2(a) shows a schematic of the cryostat system that consists of a plasma cell, a thermal-insulating vacuum system, a gas temperature control system, the electrodes, and the position-control system. The photograph of the outward appearance of LN_2 chamber is shown in Figure 2.2(b). A top view of the plasma cell is shown in Figure 2.2(c). Electrodes were placed in a plasma cell (inner volume: ~90 cm^3) inside a vacuum chamber without a radiation shield. The vacuum layer was evacuated by a scroll pump (pressure: < 10^{-1} Pa). The temperature inside the plasma cell was measured by a platinum resistance thermometer, located 15 mm from the electrodes and 15 mm from the chamber wall, and adjusted by temperature controllers (DB1000, CHINO) by controlling the output current of a 125 W heater on the wall outside the chamber and a 33 W heater between the inner chamber and a heat bath. The temperature inside the cell could be reduced to around 78 K by liquid-N_2 in the heat-bath.

Pirani and cold cathode vacuum gauges (PKR251, Pfeiffer) and four-digit capacitance gauge (Model 628B, MKS) were used to monitor the gas pressure in the plasma cell located in the outlet line. He gas (purity: >99.99995%, TAIYO NIPPON SANSO Corp.) was inlet to the chamber and the inlet flow rate was controlled by MFC. In this chamber, there was a baking system and the impurity gas could be reduced compared to the 4 K chamber. Meanwhile, the low temperatures enough to ignore the effect of impurities could not be achieved due to the cooling system.

The position of this chamber was controlled by X-Y stage (TAM-1202C-M6, SIGMA KOKI) to be able to conduct laser interferometry at the center of the electrodes. In the LN_2 chamber, LI measurements could be conducted because plasma cell was fixed to outer chamber rigidly.

This chamber was used for laser interferometry measurements with Metal-1 electrodes above 100 K (Electrodes are introduced in section 2.1.2).

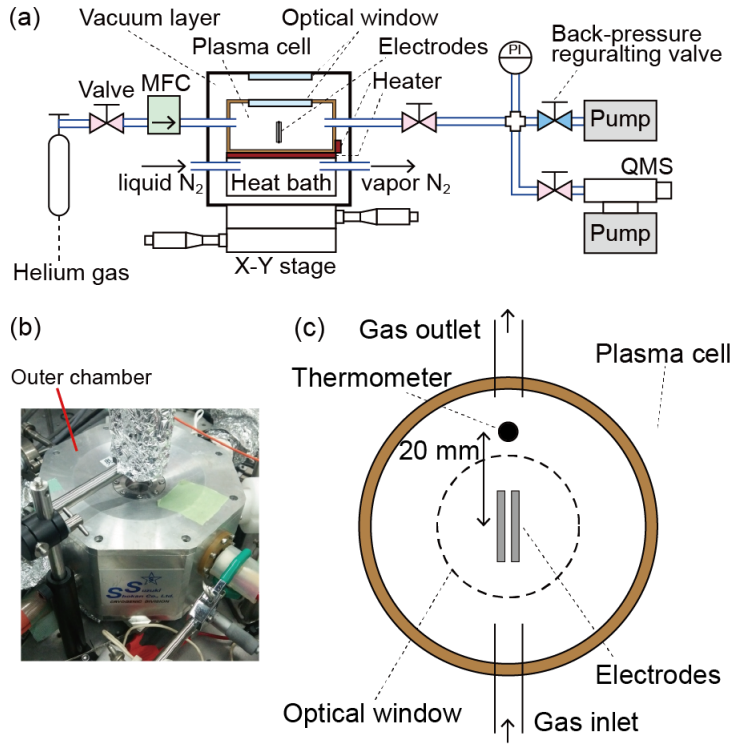

Figure 2.2 Schematic diagrams of the cryoplasma generation system used in this study. (a) Cryostat cell system consisting of plasma cell, thermal-insulating vacuum system, and gas temperature control system. (b) Photograph of the LN_2 chamber. (c) A top view of the geometry inside the plasma cell. The electrodes were set vertically and the thermometer located 20 mm from the center of the electrodes.

2.1.1.2 4 K cryoplasma chamber

The schematics and the photograph of the plasma chamber are presented in Figure 2.3. Figure 2.3(a) shows a schematic of the cryostat system that consists of a plasma cell, a thermal-insulating vacuum system, a gas temperature control system, and electrodes. The photograph of the chamber inside the outer chamber is shown in Figure 2.3(b). A schematic of a top view of the plasma cell is shown in Figure 2.3(c). Electrodes were placed in a plasma cell (inner volume: ~250 cm^3) inside a vacuum chamber and a radiation shield made of brass to allow precise control of the temperature. The vacuum layer was evacuated by a turbomolecular pump (pressure: < 10^{-3} Pa). The temperature inside the plasma cell was measured by a platinum resistance thermometer (detector temperature: T_d), located 20 mm from the electrodes and 10 mm from the chamber wall, and adjusted by a temperature controller (Model 331, Lakeshore) by controlling the output current of a 50 W heater on the wall outside the chamber. The temperature inside the cell could be reduced to 4.5 K by a Gifford-McMahon refrigerator (RDK-205D and CKW-21, Sumitomo Heavy Industries).

A capacitance vacuum gauge (PCR260, Pfeiffer) and three-digit pressure gauge (PG35, Copal) were used to monitor the gas pressure in the plasma cell located in the outlet line. He gas (purity: >99.99995%, TAIYO NIPPON

SANSO Corp.) was inlet to the chamber and the inlet and outlet flow rates were controlled by mass flow controller (MFC). Owing to the large inner volume of the chamber and the geometry, when the flow rate is enough small such as 1 cm^3 min^{-1}, it was found to cause little turbulences inside the fluid. Since there was not a baking system in the chamber, the impurity gas could not be removed perfectly. While the gas at room temperature includes a little impurity, the effect of impurities could be ignored below around 40 K, because all species except He become solid at such a low temperature.

The optical windows were placed only at the top of the chamber to achieve the stable temperature control, therefore, the probing laser beam should be reflected to be measured. Therefore, the mirror was placed under the electrodes for the measurements of LAS.

Since the plasma cell was placed on the pillars of glass-fiber reinforced plastics having low rigidity, the small vibration of plasma cell was inevitable. Therefore, LI measurements could not be conducted in the 4 K chamber, because the vibration of sub-micrometer scale was critical for LI.

This chamber was used for OES measurements in Metal-2 electrodes and both OES and LAS measurements in DBD electrodes.

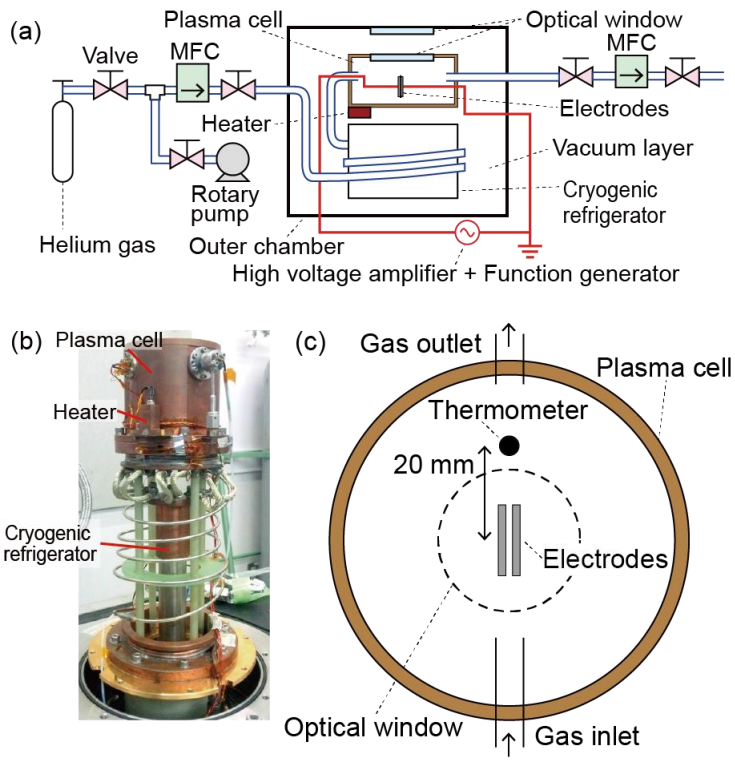

Figure 2.3 Schematic diagrams and a photograph of the cryoplasma generation system used in this study. (a) Cryostat cell system consisting of plasma cell, thermal-insulating vacuum system, and gas temperature control system, (b) Photograph inside the outer chamber and (c) A top view of the geometry inside the plasma cell. The electrodes were set vertically and the thermometer located 20 mm from the center of the electrodes.

2.1.2 Electrodes

We conducted experiments using three kinds of electrodes: metal electrodes with a diameter of 2 mm (Metal-1), metal electrodes with a diameter of 15 mm (Metal-2), and electrodes with dielectric barrier (DBD).

2.1.2.1 Metal electrodes with a diameter of 2 mm (Metal-1 electrodes)

Figure 2.4(a) indicates the small-diameter electrodes using for LI measurements above 100 K in section 2.2.1. The electrodes were made of copper (Cu) and their surfaces and the edges were polished. The diameter of the electrodes were 2 mm, but the surface of the electrodes were reduced to 1.7 mm due to the chamfered edge. The gap distance was 500 ± 100 μm. The silver (Ag) mirror was placed below the gap of the electrodes, in order to reflect the probing laser beam.

2.1.2.2 Metal electrodes with a diameter of 15 mm (Metal-2 electrodes)

Figure 2.4(b) indicates the relatively large-diameter electrodes using for the optical emission spectroscopy below liquid-N_2 temperature (77 K). They were polished metal disk electrodes made of niobium (Nb). The gap distance between the electrodes (diameter: 15 mm, thickness: 1 mm), which had a chamfered edge, was 200 ± 50 μm and the electrodes were placed vertically inside the chamber. Although Nb exhibits superconductivity below 9.2 K, we could not observe any effect of superconductivity on the plasmas during the experiments.

2.1.2.3 Dielectric barrier electrodes (DBD electrodes)

The DBD electrode was a parallel-plate configuration made of stainless steel electrodes with a dimension of 10 × 5 mm^2 and polyimide sheets with a thickness of ~ 0.125 mm placed on the surface of both electrodes, thereby acting as dielectrics [Figure 2.4(c)]. The discharge gas gap between the polyimide sheets was 500 ± 100 μm. The silver (Ag) mirror was placed below the DBD electrodes, in order to reflect the probing laser beam in LAS measurements in section 2.4.

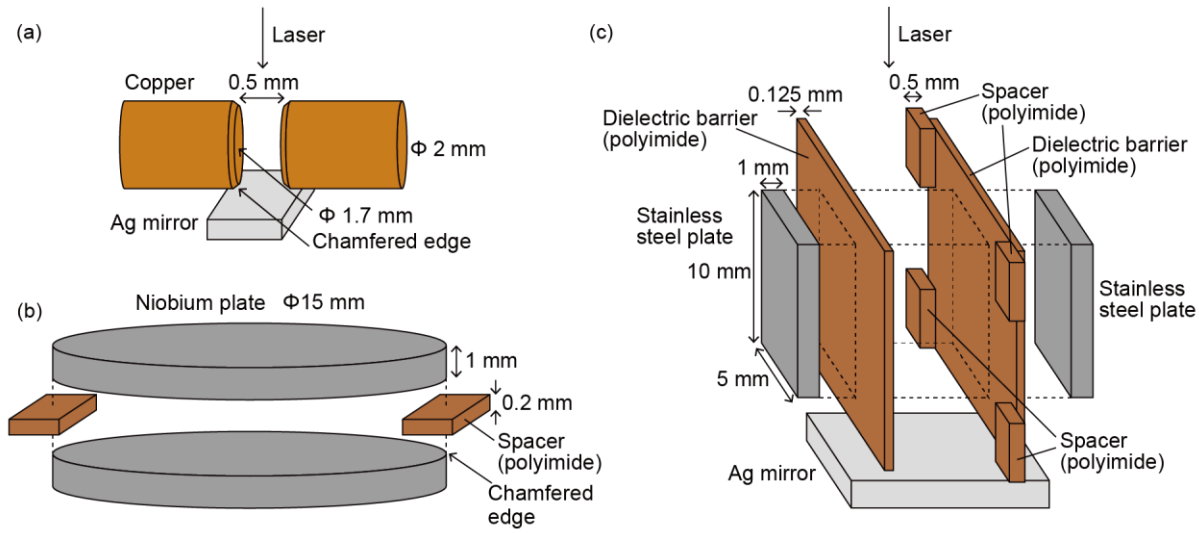

Figure 2.4 Schematics of metal electrodes with diameters of (a) 2 mm (Metal-1 electrodes) and (b) 15 mm (Metal-2 electrodes). (c) Electrodes composed of stainless steels covered by dielectric barriers of polyimide for dielectric barrier discharges (DBD electrodes). The silver (Ag) mirror was placed to reflect the probing laser beam irradiated from the top of the electrodes for Metal-1 electrodes and DBD electrodes.

2.1.3 Plasma-generating and measurement equipment

2.1.3.1 Power supply

An AC sinusoidal high voltage signal (frequency: 20 – 24 kHz, amplitude: 100 - 700 V), which was generated by the combination of a function generator (WF1974, NF Corp.) and a high-voltage amplifier (HVA4321, NF Corp.), was applied to one of the metal electrodes, and the other electrode was connected to the ground. The high-voltage amplifier limited the maximum current to approximately 10 mA, which allowed generating cryoplasmas with only little heating. However, the discharges in this study, the currents were self-limited and the function of the current limitation of the power supply was not used. In metal electrodes, the discharges were controlled below 10 mA due to the positive-resistance characteristics of the discharge mode. In DBD electrodes, the discharge modes were atmospheric-pressure glow or Townsend modes, in which the current was limited due to the surface charges on the dielectric barriers.

2.1.3.2 Current and voltage waveforms measurements (*U* & *I* waveforms)

The voltage U waveforms were the applied voltage between anode and cathode, and the current I waveforms were the current including both components of a discharge current and a displacement current.

In the experiments using Metal-1 and DBD electrodes, a 100:1 high-voltage probe (SS-0170R, Iwatsu) was used for *U* waveform measurement and 10:1 voltage probe (N2890A, Agilent) with 1 kΩ resistance for *I* waveform

measurement. The signals of voltage probes were displayed and saved in an oscilloscope (610Zi, LeCroy) with a band width of 1 GHz.

For Metal-2 electrodes, the U and I waveforms were measured using a 1000:1 high-voltage probe (P3000, Tektronix) and a current probe (CP312 + CPA300A, Tektronix). The signals, averaged over 16 measurements, were recorded by an oscilloscope (DSO5052A, Agilent) with a bandwidth of 500 MHz.

2.1.4 Experimental conditions

Experimental conditions are summarized in Table 2.1 for Metal-1, Metal-2, and DBD electrodes. In the experiments, OES measurements using Metal-2 and DBD electrodes were conducted at first, and then, LAS measurements for DBD electrodes was conducted. Finally, using Metal-1 electrodes, T_g was evaluated by LI measurements.

In OES measurements, at first, Metal-2 electrodes were used because the emission intensity should be higher for the time-resolved OES and the plasma volume was larger at Metal-2 electrodes than at Metal-1 electrodes. However, since the cryoplasmas in low-power discharge mode could not be generated in Metal-2 electrodes above T_d = 45 K, the DBD electrodes were used for the investigation of TI-OES and LAS in wide T_g range.

Then, for LI measurements, the pressure in plasmas should maintain similar to ambient condition in the plasma chamber as explained in section 2.2.1.1. In the DBD electrodes in this thesis, almost all surface area of plasmas faced the dielectric and the surface area facing the ambient gas was not large. Actually, although the LI was also tried for the DBD electrodes, the accuracy of the estimated T_g was difficult to be ensured. Therefore, a plasma source having large specific surface area, which was the ratio of surface area divided by volume, was necessary. It was found that the cryoplasmas could be generated also in electrodes composed of metals above T_d = 45 K, by reducing the diameter of electrodes from 15 to 2 mm and increasing the frequency of applied voltages from 20 to 24 kHz. Therefore, the laser interferometry (LI) was conducted to estimate T_g in cryoplasmas using Metal-1 electrodes having large specific surface area due to their small diameter.

In this thesis, the results of the measurements were introduced in order of LI, TI-OES, TR-OES, and LAS to make discussion clear. In following, other information about experimental conditions was introduced for each electrodes.

2.1.4.1 Metal-1 electrodes

Table 2.2 presents the experimental conditions of LI measurements for Metal-1 electrodes. Experiments were conducted at three T_d conditions (conditions 1A, 1B, and 1C). The plasma gas temperature T_g were the estimated values in section 2.2. The LN_2 chamber, not 4 K chamber, was used for the LI measurement due to the problem of vibration. The plasmas were generated without any gas flow and the number density of the He atoms inside the cell was kept at 2.4×10^{19} cm^{-3}.

Table 2.1 List of experimental conditions of electrode geometries, used chamber, fluid conditions, and conducted measurements for each electrodes.

Electrodes	Metal-1	Metal-2	DBD
[Electrode geometries]			
Material of metal	Cu	Nb	Stainless steel
Material of dielectric barrier	–	–	Polyimide
Shape	Disk	Disk	Rectangle
Size	ϕ 2 mm	ϕ 15 mm	5 × 10 mm
Gap distance	0.5 mm	0.2 mm	0.5 mm
[Chamber]			
Chamber	LN_2	4 K	4 K
[Fluid conditions]			
Temperature (detector) T_d (K)	100, 200, 300	5 – 45 (TI-OES) 5, 40 (TR-OES)	14, 40, 100, 300
Pressure P (kPa)	33.3, 66.7, 100	3.3 – 30 (TI-OES) 3.3, 27 (TR-OES)	4.7, 13.3, 33.3, 100
Density n (cm^{-3})	2.4×10^{19}	4.8×10^{19}	2.4×10^{19}
[Measurements]			
V & I waveforms	○	○	○
LI	○	–	–
Time-integrated OES (TI-OES)	–	○	○
Time-resolved OES (TR-OES)	–	○	–
LAS	–	–	○

In the laser interferometry technique, we do not obtain an absolute value of refractive index but the difference of refractive index from a known refractive index as indicated in equation (2. 8) in section 2.2.1.1. Therefore, applied voltages were in burst mode of power supply, in which an applied voltage is turned ON and OFF repeatedly. At T_d = 100 K, the applied voltages whose frequency was 24 kHz were switched ON and OFF repeatedly with a period of 10 ms (8 ms ON and 2 ms OFF). Figure 2.5 shows the voltage and current waveforms at T_d = 100 K (condition 1A) and the U and I waveforms at conditions 1B and 1C were similar. Figure 2.5(a) and (b) indicate the waveforms of U and I, respectively, and the magnified U and I waveforms from 5.00 to 5.10 ms was indicated in Figure 2.5(c). Figure 2.5(b) indicates that the current gradually increased with some time lag (about 2 ms) from the timing when the voltage began to be applied. In the time lag, the only displacement current flows. The average power consumption P_c at the stable phase, e.g. from t = 1 – 6 ms in Figure 2.5, was 32 mW. At T_d = 200 K (condition 1B), the ON/OFF times were

18 ms / 2 ms and the average power consumption P_c at the stable voltage phase was 15 mW. The reason why the ON time was longer than at T_d = 100 K was that the time lag was longer. The ON/OFF time was 1.8 ms/1.2 ms at T_d = 300 K (condition 1C), and the various P_c conditions were measured to discuss the dependency of T_g on P_c.

Table 2.2 Experimental conditions using Metal-1 electrodes for LAS measurements.

		Condition 1A	*Condition 1B*	*Condition 1C*
Detector temperature	T_d	100 K	200 K	300 K
Plasma gas temperature [a]	T_g	179 K (simulation) 104 K (LI)	230 K (simulation) 202.5 K (LI)	347 K (simulation) 301 – 304 K (LI)
Pressure	P	33 kPa	67 kPa	100 kPa
Number density	n		2.4×10^{19} cm^{-3}	
Introduced gas species	-		He + air impurity	
Frequency	f		AC 24 kHz (Burst mode)	
ON/OFF time (Burst)		8 ms/2 ms	18 ms/2 ms	1.8 ms/1.2 ms
Applied voltage (peak)	U	320 V	332 V	325 – 362 V
Power consumption	P_c	32 mW	15 mW	6.2 – 31 mW

a: T_g was estimated by thermal simulation and laser interferometry.
b: Partial pressure of impurity gases decreased to be approximately sublimation pressures. The ratio of N_2 and O_2 were estimated to be 2.4×10^{-4} and 5.7×10^{-6}.

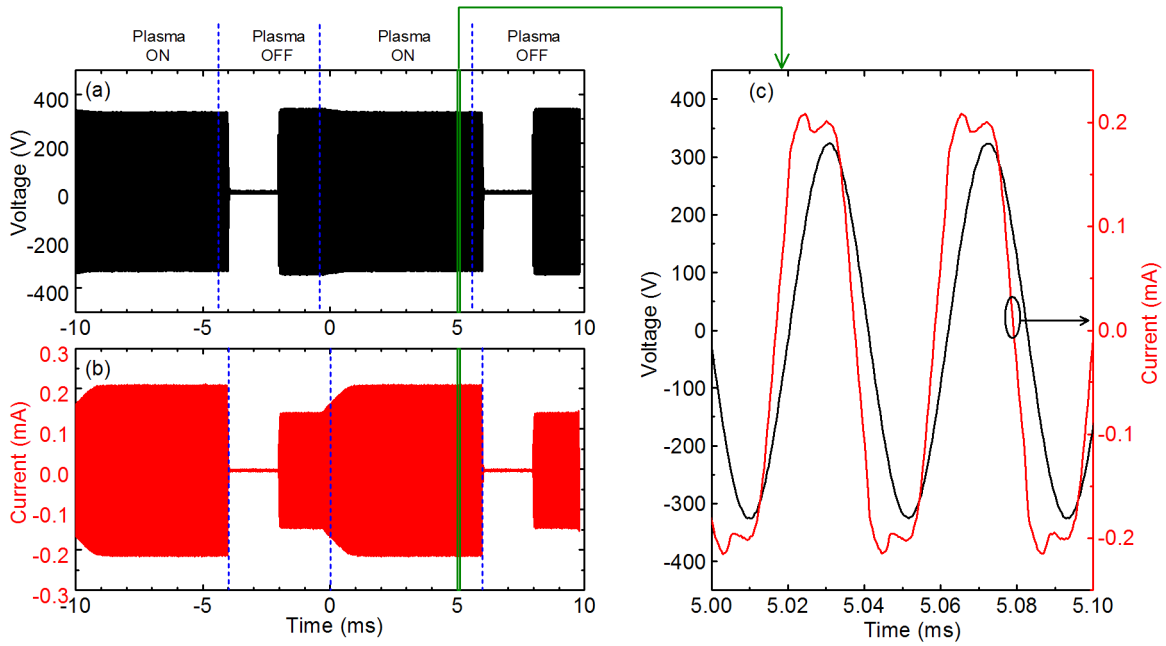

Figure 2.5 Waveforms of (a) voltage U and (b) current I from t = −10 to 10 ms and (c) the magnified view of U and I waveforms from t = 5.00 to 5.10 ms in Metal-1 electrodes at T_d = 100 K. Current gradually increased with some time lag (about 2 ms) from the timing when the voltage began to be applied (t = −2 ms). In the time lag, the only displacement current flows. The average power consumption P_c at the stable phase from t = 1 – 6 ms was 32 mW.

2.1.4.2 Metal-2 electrodes

Using the metal electrodes with diameter of 15 mm (Metal-2), we conducted experiments at the range of T_d = 5 – 45 K (conditions 2TI) for the TI-OES measurements and T_d = 5 and 40 K (conditions 2A and 2B) for TR-OES measurements. The 4 K chamber was used for the experiments. All valves were kept closed during the experiment after the introduction of He gas up to a pressure of 200 kPa at room temperature (296 K); consequently, the plasmas were generated without any gas flow and the number density of the He atoms inside the cell was kept at 4.8×10^{19} cm^{-3}. We did not perfectly purge the cell to remove impurities completely from inside the plasma cell, in order to be able to observe the temperature variations caused by small amounts of air impurities. Therefore, one of the main differences between conditions 2A and 2B was the presence of impurity species, in addition to the difference of T_g. Pure helium gas without any impurity gases could be achieved under condition 2A because of almost complete condensation of impurity species. On the other hand, although the temperature at condition 2B is lower than the boiling points of air impurity species at atmospheric pressure (77 K for N_2 and 90 K for O_2), the presence of impurities cannot be ruled out completely, and the partial pressures of the impurity gases at condition 2B are almost equal to sublimation pressure because of partial condensation. Since the total pressure was 27 kPa and the sublimation pressures of N_2 and O_2 at condition 2B are 6.4×10^{-3} kPa, and 1.5×10^{-4} kPa [54], respectively, the ratio of N_2 and O_2 with respect to He are

estimated to be 2.4×10^{-4} and 5.7×10^{-6} for condition 2B, respectively. Since the ratio of O_2 is low, we assumed that O_2 could be neglected in the reaction model in this study.

Table 2.3 Experimental conditions using Metal-2 electrodes for measurements of time-integrated and time-resolved OES measurements.

		Conditions 2TI	*Condition 2A*	*Condition 2B*
Detector temperature	T_d	5 – 45 K	5 K	40 K
Plasma gas temperature [a]	T_g	18 – 50 K	28 K (simulation)	54 K (simulation)
Pressure	P	3.3 – 20 kPa	3.3 kPa	27 kPa
Number density	n		4.8×10^{19} cm^{-3}	
Introduced gas species	–		He + air impurity[b]	
Actual gas species	–	Pure He, He + air impurity [b]	Pure He	He + air impurity [b]
Frequency	f		AC 20 kHz	
Applied voltage (peak)	U	205 – 244 V	206 V	208 V
Power consumption	P_c	1 – 31 mW	69 mW	65 mW

a: T_g was estimated value by thermal simulation.
b: Partial pressure of impurity gases decreased to be approximately sublimation pressures discussed in section 2.5.1.3. The ratio of N_2 and O_2 were estimated to be 2.4×10^{-4} and 5.7×10^{-6}.

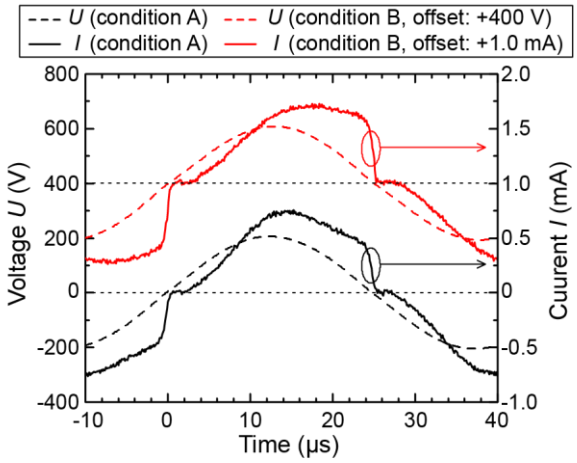

Figure 2.6 Waveforms of applied voltages U (dashed lines) and discharge currents I (solid lines) measured at condition 2A (T_d = 5 K, T_g = 28 K, black lines) and condition 2B (T_d = 40 K, T_g = 54 K, red lines). For the sake of clarity, the U and I curves at condition B are offset by +400 V and +1.0 mA, respectively. The horizontal dotted lines indicate the base lines for each condition. The discharge current was calculated by subtracting the displacement current from the measured current.

Waveforms of the applied voltage U (dashed lines) and discharge current I (solid lines) measured at conditions

2A and 2B were shown in Figure 2.6. The decay of I was slow until just before $U = 0$, and thus, a relatively long (> 20 μs) and moderate (maximum amplitude 0.7 – 0.8 mA) current, not a pulse current, was observed. It was confirmed by optical observation that the discharge was homogeneous and spread over the entire electrode area. The power consumption P_c was estimated from the measurements of voltage and current waveforms shown in Figure 2.6 and, as a result, the values of P_c were 69 mW for condition A and 65 mW for condition B.

2.1.4.3 DBD electrodes

For DBD electrodes, the experiments were conducted at three T_d conditions: 14, 100, and 300 K (conditions 3A – 3C). The experimental conditions were listed in Table 2.4. In this measurement, the 4 K chamber was used. The helium flow was controlled at approximately 100 sccm by the flow controllers with the 4 K chamber. The number density was kept at 2.4×10^{19} cm^{-3} and, thereby, the pressures decreased with T_d decrease. The introduced gas was He with a small amount of air impurity similar to the experiments with Metal-2 electrodes. The applied frequency were AC 10 kHz with the burst mode because it was necessary for the LAS measurements. Applied voltages were fixed at approximately 700 V and power consumptions P_c were around 20 mW for each temperature.

Table 2.4 Experimental conditions using DBD electrodes for time-integrated OES and LAS measurements.

		Condition 3A	*Condition 3B*	*Condition 3C*
Detector temperature	T_d	14 K	100 K	300 K
Plasma gas temperature [a]	T_g	31 K (simulation)	111 K (simulation)	305 K (simulation)
Pressure	P	4.7 kPa	33 kPa	100 kPa
Number density	n		2.4×10^{19} cm^{-3}	
Introduced gas species	-		He + air impurity	
Actual gas species	-	pure He	He + air impurity[b]	He + air impurity[b]
Frequency	f		AC 10 kHz (Burst: 10 ms ON – 10 ms OFF)	
Applied voltage (peak)	U		700 V	
Power consumption	P_c	15.4 mW	24 mW	22.3 mW
Wavelength of probing laser	λ_0	1082.945 nm	1082.910 nm	1083.035 nm

a: T_g was estimated by thermal simulation and laser interferometry.
b: Partial pressure of impurity gases is discussed in section 2.5.1.3.

2.2 Evaluation of plasma gas temperature T_g

The evaluation of T_g is inevitable to generate T_g-controlled plasms such as cryoplasmas. In addition, in order to discuss the dependency of a phenomenon on T_g by experimental methods, the evaluation of T_g is necessary. In this study, T_g was evaluated by laser heterodyne interferometry and thermal simulations. In section 2.2.1, method of laser interferometry are introduced at first, and then the experimental conditions and results are presented. Then, the method and the results of thermal simulations are indicated in section 2.2.2. Finally, the evaluation results of T_g obtained by two methods are discussed in section 2.2.3.

2.2.1 Laser interferometry (LI)

2.2.1.1 Method of Laser interferometry (LI)

In this study, the laser heterodyne interferometry (LI) technique was used to estimate T_g. The phase shift of the probing laser beam which was caused by plasma generation was detected. Then by analyzing the phase shift, the variation of refractive index, which depends on gas density, was calculated. Finally, the value of T_g was estimated from the variation of the calculated gas density in the assumption of equilibrium state.

The optical setup in Mach-Zehnder interferometer is shown in Figure 2.7(a). In this measurement, to achieve sensitive measurement of the phase shift, a heterodyne technique was used. The probing laser was an external-cavity diode laser whose wavelength was 1550 nm. The optical isolator was installed to avoid the intrusion of the reflected laser beam into the diode laser and the polarization plate was to set the polarization direction to perpendicular to the top surface of the optical table. The probing laser-beam was split and the frequency in only one arm was modulated at 110 MHz by acousto-optic modulator (AOM, TEM-110-25-890, Brimrose). The non-modulated arm (zeroth-order light) from the AOM was introduced to the high-speed detector via some mirrors. On the other hand, the modulated arm (first-order light) from the AOM was introduced to the LN_2 chamber and the reflected laser beam from the Ag mirror reached the high-speed detector after the light axes of the both arm was merged each other between the half mirror and the detector. The combination of the half-wave plate, polarizing beam splitter, and quarter-wave plate, instead of a half mirror, were used to reduce the loss of the light intensity at the split of reflected light (from LN_2 chamber) to original light (to LN_2 chamber). To setup the light axis easily, a He-Ne laser beam with a wavelength of 633 nm (HNL008L-JP, Thorlabs) was merged with the first-order light axis. The almost the same setup was used and details of the setup of the LI have been introduced in Ref. [27].

The intensity of the beat signal at the high-speed detector $I(t)$ is indicated using the electric field of the zeroth-order light U_1 and that of the first-order light which passed through the plasma chamber U_2 as

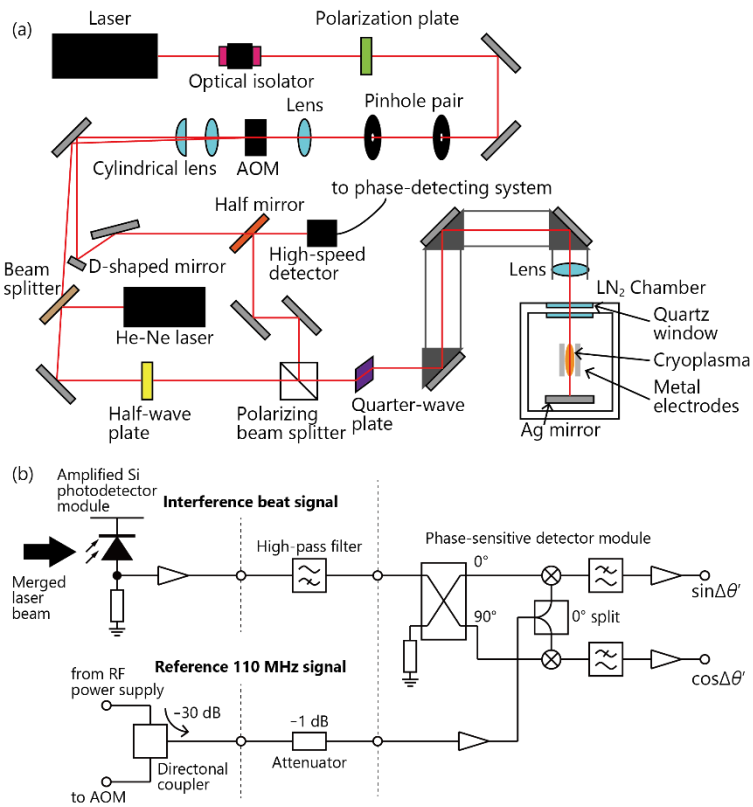

Figure 2.7 Schematics of (a) optical setup and (b) phase detecting system for laser heterodyne interferometry system.

$$U_1(t) = E_1 \exp(i\omega t) \tag{2. 1}$$

$$U_2(t) = E_2 \exp\{i[(\omega + \Delta\omega)t + \Delta\theta(t) + \phi]\} \tag{2. 2}$$

$$I(t) = |U_1(t) + U_2(t)|^2 = E_1^2 + E_2^2 + 2E_1E_2 \cos[\Delta\omega t + \Delta\theta(t) + \phi] \tag{2. 3}$$

where E_1 and E_2 are the maximum electric fields of each light, ω is the angular frequency of the laser light, $\Delta\omega = 2\pi \times 110$ MHz is the modulation frequency, $\Delta\theta$ is the phase shift due to the existence of the plasma, and ϕ is the difference of the phase due to the difference of the lengths of the light paths between zeroth-order and first-order lights.

The detected signal of the high-speed detector was inputted to a phase-detecting system shown in Figure 2.7(b). The phase of interference beat signal and that of reference signal with $\Delta\omega$ from the radio-frequency power supply of AOM were compared at the phase-sensitive detector module. The output signals from the phase-detecting system were $\cos\Delta\theta'$ and $\sin\Delta\theta'$ where $\Delta\theta'$ is the phase difference between the signals. The value of $\Delta\theta'$ was expressed as

$$\Delta\theta'(t) = \Delta\theta(t) + \phi' \tag{2. 4}$$

where ϕ' is the phase difference between the reference signal from AOM driver and the first-order light at no plasma. Although the value of ϕ' was difficult to be estimated directly because the lengths of the light paths were difficult to be measured, the value of ϕ' was constant at identical conditions without vibrational and electrical noises. Therefore,

we estimated the $\Delta\theta$ by comparing the phase at a standard time when the variation of refractive index in plasmas (N_p) was almost relaxed, in other words, N_p was considered as the same value as the refractive index at the ambient gas in the plasma chamber (N_0). However, in the actual measurements, since the value of ϕ' was not an identical constant in each measurements due to the small phase shift due to tiny wind and vibration noises of the measurement systems, these noises was not able to be eliminated perfectly.

The value of $\Delta\theta$ was expressed in Wentzel-Kramers-Brillouin approximation (characteristic lengths of the spatial variation of the refractive index is much longer than the probing-beam wavelength) as

$$\Delta\theta(t) = \frac{2\pi}{\lambda_0}\int\left[N_\mathrm{p}'(t) - N_0\right]\mathrm{d}y \tag{2. 5}$$

where λ_0 is the wavelength of probing laser and y is the position along the laser beam path. The N_p depends on the electron density n_e and the gas density n. The phase shifts due to n_e ($\Delta\theta_{ele}$) and n ($\Delta\theta_{gas}$) are expressed as

$$\Delta\theta(t) = \Delta\theta_\mathrm{ele}(t) + \Delta\theta_\mathrm{gas}(t) = -\frac{e^2\lambda_0}{4\pi\varepsilon_0 m_\mathrm{e}c^2}\int n_\mathrm{e}(t)\mathrm{d}y + \frac{2\pi}{\lambda_0}\int\left[N_\mathrm{p}'(t) - N_0\right]\mathrm{d}y \tag{2. 6}$$

where e is elementary charge, ε_0 is the permittivity of vacuum, m_e is the mass of an electron, c is the speed of light in vacuum, and N_p' is the refractive index of plasma varied due to the gas density. The former component $\Delta\theta_{ele}$ can be introduced by the expression of permittivity in Drude model under first-order approximation and an assumption that imaginary term is ignored. These assumptions are valid for the condition in the values of λ_0, n_e, and n in this experiment [27].

For the situation where the gas composition is uniform and the absorption line profile does not change along the laser path (length: l), equation (2. 6) is expressed as

$$\Delta\theta(t) = -\frac{e^2\lambda_0 l}{4\pi\varepsilon_0 m_e c^2}n_\mathrm{e}(t) + \frac{2\pi l}{\lambda_0}\left[N_\mathrm{p}'(t) - N_0\right]. \tag{2. 7}$$

In this study, the values of λ_0 and l were 1.55 μm and 3.4 mm, respectively, and the resolution of $\Delta\theta$ was approximately 0.01 – 0.1 degree. Table 2.5 shows the relationship among $\Delta\theta$, n_e, and $\Delta N_p \equiv N_p' - N_0$. In this study, since the values of n_e was below 10^{12} cm^{-3}, the $\Delta\theta_{ele}$ was too small to be detected. Finally, $\Delta\theta$ was expressed as

$$\Delta\theta(t) = \frac{2\pi l}{\lambda_0}\Delta N_\mathrm{p}(t). \tag{2. 8}$$

The experiments were conducted at the ambient temperatures inside the plasma chamber of 100, 200, and 300 K at the number density corresponding to the atmospheric condition. Generally, the refractive index depends on n, and n depends on T_g and P. For the calculation of ΔN_p, the value of P in the plasma was assumed to keep the same value as that in the ambient gas. In addition, the refractive index depends also on λ_0 generally. However, the dispersion relation was ignored in this study, and the values of N_p were calculated as a square root of the relative permittivity with an

assumption of a constant magnetic permeability. This assumption is discussed in section 2.2.3. The data of the relative permittivity were retrieved from the NIST database of thermophysical properties "REFPROP" [26], and the relationship between T_g and the difference of refractive index ΔN_p at constant P are indicated as Table 2.6.

Table 2.5 Electron density n_e in the component of $\Delta\theta_{ele}$ and difference of refractive index ΔN_p in the component of $\Delta\theta_{gas}$ at the phase shift $\Delta\theta$ which were the almost minimum values to be detected.

$\Delta\theta$ (degree)	n_e (cm^{-3})	$\Delta N_p \equiv N_p' - N_0$
0.01	1.18×10^{13}	1.27×10^{-8}
0.1	1.18×10^{14}	1.27×10^{-7}

Table 2.6 Relationship between plasma gas temperature T_g and difference of refractive index at constant pressure P at three conditions at T_d = 100, 200, and 300 K at the number density n in plasma chamber which corresponds to that at ambient air. The data were calculated by a square root of the relative permittivity, and the values of the relative permittivity were retrieved from REFPROP [26].

Ambient condition: T_d = 100 K, P = 0.033 MPa, N_0 = 1.00003109.		Ambient condition: T_d = 200 K, P = 0.067 MPa, N_0 = 1.00003109.		Ambient condition: T_d = 300 K, P = 0.1 MPa, N_0 = 1.00003109.	
Temperature T_g (K)	Difference of refractive index at constant P ΔN_p ($\times 10^{-7}$)	Temperature T_g (K)	Difference of refractive index at constant P ΔN_p ($\times 10^{-7}$)	Temperature T_g (K)	Difference of refractive index at constant P ΔN_p ($\times 10^{-7}$)
100	0.0	200	0.0	300	0.0
101	−3.1	201	−1.5	301	−1.0
102	−6.1	202	−3.1	302	−2.1
103	−9.1	203	−4.6	303	−3.1
104	−12.0	204	−6.1	304	−4.1
105	−14.8	205	−7.6	305	−5.1
106	−17.6	206	−9.1	306	−6.1
107	−20.3	207	−10.5	307	−7.1
108	−23.0	208	−12.0	308	−8.1
109	−25.7	209	−13.4	309	−9.1
110	−28.3	210	−14.8	310	−10.0
111	−30.8	211	−16.2	311	−11.0
112	−33.3	212	−17.6	312	−12.0
113	−35.8	213	−19.0	313	−12.9
114	−38.2	214	−20.3	314	−13.9
115	−40.5	215	−21.7	315	−14.8
116	−42.9	216	−23.0	316	−15.7
117	−45.2	217	−24.3	317	−16.7
118	−47.4	218	−25.7	318	−17.6
119	−49.6	219	−27.0	319	−18.5
120	−51.8	220	−28.3	320	−19.4

In the measurement, the issue of noises was critical. There were mainly three kinds of noises in this measurement, i.e. electrical noises having high frequency components, vibrational noises due to vibrations of ambient equipment and winds, and noises with the integral multiple of 50 Hz which corresponds to commercial frequency. To reduce the noises, the measured signal was averaged in two ways. At first, the electrical noises having high-frequency components were reduced by averaging the adjacent 20 data points in each output waveforms of phase detecting system: $\cos\Delta\theta'(t)$ and $\sin\Delta\theta'(t)$. Meanwhile, the vibrational noises were reduced by averaging the signals at the same timing among waveforms $\Delta\theta'(t)$ which had been transformed from the measured waveforms of $\cos\Delta\theta'(t)$ and $\sin\Delta\theta'(t)$, because the vibrational noises affected not the electrical signal but the phase shift directly. The measurements were repeated more than 5000 times to reduce the vibrational noises on the measured signal at each condition. To reduce the effect of the inevitable noises of 50 Hz, the time length of measured waveforms had better be much smaller than a period of commercial frequency of 20 ms. However, although the period of ON/OFF time was similar as the commercial frequency at $T_d = 100$ and 200 K, the effect of the noises from commercial frequency were enough reduced by averaging a lot of (more than 5000) measured data.

Concerning the ON/OFF times in the burst mode of the applied voltage, the times were determined as following. During ON time, the refractive index N_p' decreased due to the expansion of the plasma gas due to heating. The ON time was set to be enough to let the refractive index stable. Similarly, the OFF time was determined to satisfy that the refractive index N_p' became stable at the almost same value as N_0, i.e. $\Delta N_p \sim 0$. The period of the burst mode at $T_d = 300$ K was shorter than other conditions because the time which was necessary to become stable in OFF time was shorter than lower temperatures.

2.2.1.2 Results

Figure 2.8 shows the results of LI at $T_d = 100$ K, which were averaged in 10000 times. The U and I waveforms have already been indicated in Figure 2.5. The variation of refractive index $\Delta N_p = N_p' - N_0$ in plasma ON time was around 12×10^{-7} as shown in Figure 2.8, which corresponds to the increase of T_g about 4 K (see Table 2.6). The temporal evolution of ΔN_p in one cycle of applied frequency of 24 kHz was lower than detecting limit. In the calculation of ΔN_p, it was assumed that the phase shift was caused by the homogeneous refractive index in plasma region with the length of 3.4 mm, which was twice of diameter of electrodes because laser passed through the plasma twice. Therefore, at the center of the plasmas, the increase of T_g might be larger than 4 K. While we could not evaluate the distribution of T_{inc} in this LI measurement, the distribution of T_{inc} is discussed in the thermal simulation in section 2.2.2. Concerning the noises, the vibration with a frequency of approximately 100 Hz existed in ΔN_p. This was probably due to the commercial frequency of 50 Hz and the actual refractive index did not have a frequency component of 100 Hz.

Figure 2.9(a) indicates a temporal evolution of ΔN_p at various power consumption P_c at $T_d = 300$ K. Although the starting timing of the decrease of ΔN_p were various, the values of ΔN_p became stable before the applied voltage turned OFF. The right vertical axis indicates the approximate values of T_{inc}. As shown in the relationship between ΔN_p and T_{inc} presented in Table 2.6, the parameters are in approximately proportional relation within small T_{inc} (< 20 K). The

increase of T_g as a function of power is presented in Figure 2.9(b). The values of ΔN_p are the average values within the temporal range between t = 1.33 – 1.65 ms in Figure 2.9(a). Its regression line, which was calculated in the assumption that Y-intercept was zero, is also presented in Figure 2.9(b). Here, if T_{inc} was assumed to be proportional to P_c, the proportionality coefficient (C_{TP}) was approximately 0.14 K mW^{-1}, which was estimated from the proportionality coefficient between ΔN_p and P_c in Figure 2.9(b) and the relationship between ΔN_p and T_{inc} in Table 2.6. Although the linear assumption is not accurate in wide P_c range, the assumption can be used for small P_c (< 50 mW) as discussed in section 2.2.2.2.

At T_d = 100 K, in the linear assumption, the C_{TP} was approximately 0.13 K mW^{-1}, which was calculated from T_{inc} ~ 4 K and P_c ~ 32 mW. At T_d = 200K, P_c was 15 mW estimated from U and I waveforms as shown in Table 2.2. From LI measurement, ΔN_p was approximately -0.27×10^{-7} and, as a result, T_{inc} was approximately 2.5 K. Therefore, the proportionality coefficient C_{TP} was 0.17 K mW^{-1}.

In conclusion, the proportionality coefficient C_{TP} at T_d = 100, 200, and 300 K were approximately 0.13 K mW^{-1}, 0.17 K mW^{-1}, and 0.14 K mW^{-1}. The ratio of $\Delta N_p / P_c$ at each measured point shown in Figure 2.9(b) was 0.17×10^{-7} mW^{-1} at highest and 0.13×10^{-7} mW^{-1} at lowest. This implies that the values of C_{TP} for T_d = 100, 200, and 300 K was within the error bar and the dependency on temperature could not be discussed.

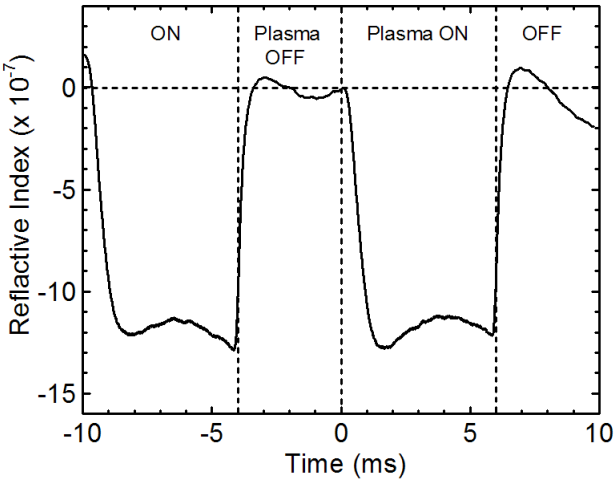

Figure 2.8 Temporal evolution of the difference of refractive index of plasma region from ambient region ($\Delta N_p = N_p' - N_0$) at T_d = 100 K, which were calculated from the output signals of phase-detecting system. The horizontal axis corresponds to that in Figure 2.5(a).

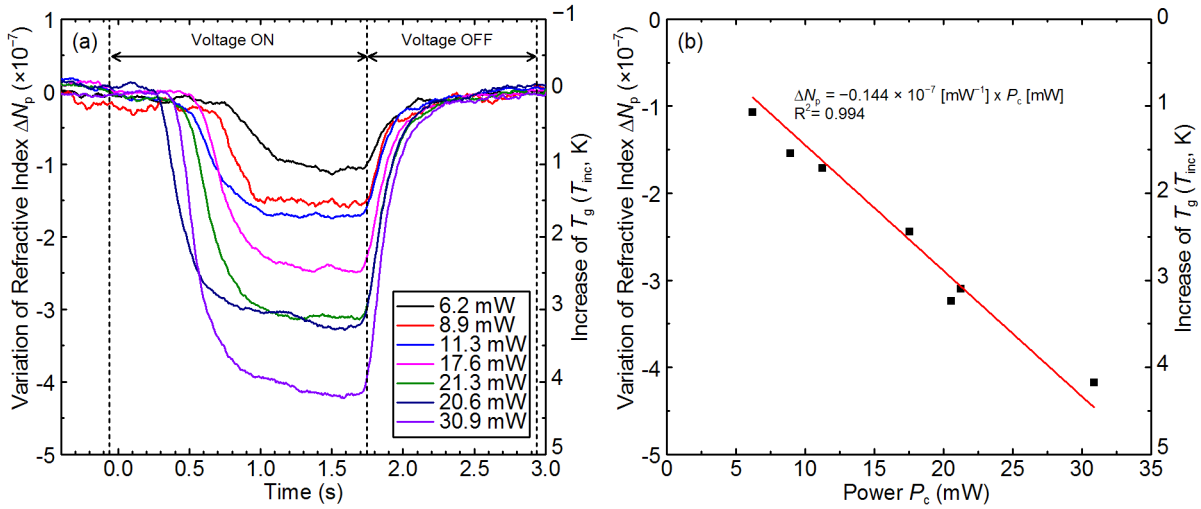

Figure 2.9 (a) Temporal evolution of ΔN_p at various power consumption P_c at T_d = 300 K. The voltage ON and OFF time were indicated and the times when plasma began to be ignited were different at each condition. The right vertical axis indicate the approximate values of increase of T_g (T_{inc}). The relationship between ΔN_p and T_{inc} is presented in Table 2.6. (b) ΔN_p as a function of P_c at T_d = 300 K with regression line calculated by least-square technique. The values of ΔN_p were the average values within the temporal range between t = 1.33 – 1.65 ms in (a). In the calculation of regression line, Y-intercept was fixed as zero.

2.2.2 Thermal simulation

2.2.2.1 Simulation method

In this section, we estimated T_g from the balance of the thermal energies between the discharge area (plasma gas), the ambient gas inside the chamber, and the electrodes, using a heat conduction equation in an axisymmetric cylindrical coordinate system.

$$\rho C_P \frac{\partial T_g}{\partial t} = \lambda_{therm}\left(\frac{\partial^2 T_g}{\partial r^2} + \frac{1}{r}\frac{\partial T_g}{\partial r} + \frac{\partial^2 T_g}{\partial z^2}\right) + \frac{P_h}{Ad}, \tag{2. 9}$$

where ρ is density, C_p is the isobaric specific heat, t is the time, λ_{therm} is the thermal conductivity, r is the radial coordinate, z is the axial coordinate perpendicular to the electrode surface, and P_h is the power contributing to thermal heating of plasma gas. For the calculation we only took into account He atoms, assuming that other species such as charged or excited species, He molecules, and impurity species can be neglected because of the low ionization degree.

The values of T_g were estimated by an explicit finite difference method for the cylindrical geometry shown in Figure 2.10. The lengths in Figure 2.10 are indicated in Table 2.7. It was assumed that the temperature distribution was axisymmetric with respect to the central axis of the electrode disks and plane-symmetric with respect to the center plate of the electrode. REFPROP database [26] was referred for the thermophysical properties of He. The adopted values of

thermophysical properties of solids facing to the plasma in this study were listed in Table 2.7. The values were approximate values for the references [28,29] without considering the variation depending on temperature. Although the variations of the properties of gas depending on temperature affect the simulation results considerably, that of solids were confirmed not to affect the simulation results seriously (less than 1 K).

At the initial condition, all grid nodes had a homogeneous temperature of T_d. The outside boundary along the lines at $r = r_{area}$ and $z = z_{area}$ satisfied the Dirichlet boundary condition and was maintained at T_d, because we successfully maintained a constant temperature of the thermometer at the location 20 mm from the center of the plasma. The lines of $r = 0$ and $z = 0$ were set to special Neumann (adiabatic) boundary conditions, because of the simplified geometry under the assumption of axis symmetry. The lengths indicated in Table 2.7 were not always accurate for the actual geometries, for example, r_{plasma} in DBD electrodes was determined as the area of the plasma with circle shape in the calculation geometry (50.2 mm^2) was similar to that with rectangle shape in the experiment (50 mm^2).

To estimate the heat transfer coefficient h of the boundary between He and electrode materials, we assumed that the Nusselt number (Nu) was 4, which was estimated as follows: Under the conditions of the vertical thin plates, the average Nu can be estimated by the following equation [30]:

$$Nu \equiv \alpha L/\lambda = 0.473 + 0.502Ra^{1/4}\,, \tag{2. 10}$$

where

$$Ra = Gr \times Pr = g\beta\Delta T\frac{d^3}{\nu^2} \times Pr. \tag{2. 11}$$

Here, Ra, Gr, and Pr are the dimensionless Rayleigh, Grashof, and Prandtl numbers respectively, g is the acceleration due to gravity, β is the coefficient of volume expansion, ΔT is the difference between the wall and gas temperatures, d is the typical length of the system, and ν is the dynamic coefficient of the viscosity. Pr, β, and ν were calculated by REFPROP [26]. The calculation was conducted with introducing a homogeneous power density in the plasma region ($r \leq r_{plasma}$ mm, $z \leq z_{plasma}$).

The P_h is represented as $P_h = \eta P_c$ where η is the energy efficiency for plasma gas heating ($0 \leq \eta < 1$). The η is generally smaller than 1, because there must be some energy loss due to, for instance, radiation and energy conduction to the electrodes from the species other than He atoms, such as electron having high kinetic energy and metastable species having high chemical energy. Since the estimation of η is not easy, we assumed $\eta = 1$ in this study.

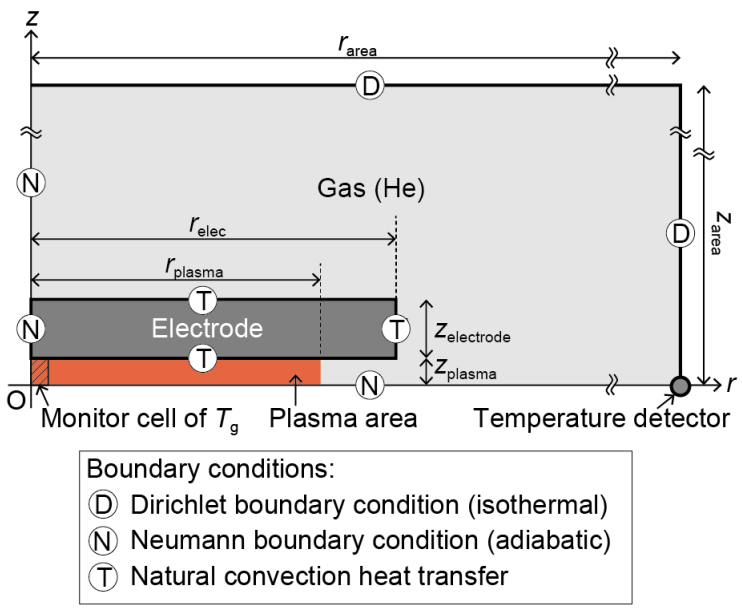

Figure 2.10 Axisymmetric cylindrical geometry of the domain for the numerical estimation of T_g. Since the geometry in our experiments could be assumed to be symmetric with respect to r = 0 and z = 0, the calculation domain was limited to a quarter of the complete experimental volume.

Table 2.7 Lengths in the geometries shown in Figure 2.10 and thermophysical properties of solids for each electrodes in the thermal simulations.

	Metal-2	Metal-1	DBD
[*Geometry*] (unit: mm)			
r_{area}	20	15	15
z_{area}	20	2	2
r_{solid}	7.5	1	10
z_{solid}	1	1.75	1.75
r_{plasma}	7.5	0.85	4 [a]
z_{plasma}	0.1	0.25	0.25
[*Thermophysical property of electrodes*]			
Material of solid facing plasma	Nb	Cu	Polyimide
Thermal conductivity λ_{therm} (W m^{-1} K^{-1})	200	400	0.29
Isobaric specific heat C_p (J kg^{-1} K^{-1})	270	350	1.13
Density ρ (g cm^{-3})	8.57	8.94	1.47
Refrence	[29][a]	[29][b]	[28][c]

a: r_{plasma} in DBD electrodes was determined as the area of the plasma with circle shape in the calculation geometry (50.2 mm^2) was similar to that with rectanble shape in the experiment (50 mm^2).

2.2.2.2 Simulation results in metal electrodes with diameter of 2 mm (Metal-1)

The experimental conditions using Metal-1 electrodes are indicated in section 2.1.4.1 in detail. As mentioned in section 2.1.4.1, P_c were 32 mW for T_d = 100 K (condition 1A), 15 mW for T_d = 200 K (condition 1B), and from 6.2 to 31 mW for T_d = 300 K (condition 1C).

The simulation results of the spatial distribution of the increase of plasma gas temperature ($T_{inc} = T_g - T_d$) after 0.1 s from plasma ignition is indicated in Figure 2.11. The values of T_g in the region of plasma are relatively increased, while T_g at the edge of the calculation area at $z = z_{area}$ is kept at T_d. Concerning a time evolution of T_g, although a gradual increase of T_g continues after 0.1 second, a drastic increase just after plasma ignition were within 0.1 s. The time evolution of T_g is discussed in section 2.2.2.3. The distribution of T_{inc} on r axis was indicated in Figure 2.11(b). Inside the plasma region, there was a distribution of T_g, for example, T_{inc} at the edge of the plasma region (r = 0.85 mm) was about 0.7 times of T_{inc} at the center of the plasma (r = 0). In following, the values of T_g and T_{inc} for each condition are those at the center of the electrodes at r = 0 and z = 0.

The simulation results at experimental conditions 1A (T_d = 100 K) and 1B (T_d = 200 K) were T_g = 179 K and 230 K, respectively. The simulation results for various P_h at T_d = 300 K are shown in Figure 2.12. The results at condition 1C are indicated in Figure 2.12(a) and in more wide range of P_h are in Figure 2.12(b). Although the T_g were not proportional to P_h strictly, the assumption of proportionality between them might be valid for small P_h range at lower than 50mW. The proportionality coefficient C_{TP} between T_g and P_h at T_d = 100, 200, and 300 K obtained from the thermal simulations were approximately 2.5 K mW^{-1}, 2.0 K mW^{-1}, and 1.6 K mW^{-1}, respectively.

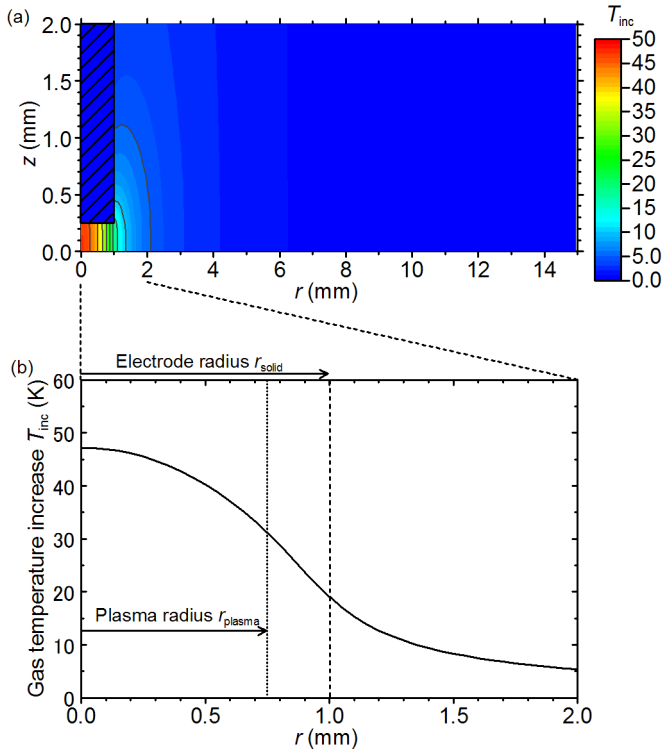

Figure 2.11 (a) Contour plot of increase of T_g (T_{inc}) compared to T_d = 300 K at 1 s after plasma ignition in Metal-1 electrodes (P_h = 31 mW, condition 1C). The shaded portion indicates the region of the electrodes. The gray lines indicate the border lines at every 5 K. (b) Spatial distribution of T_{inc} at z = 0.

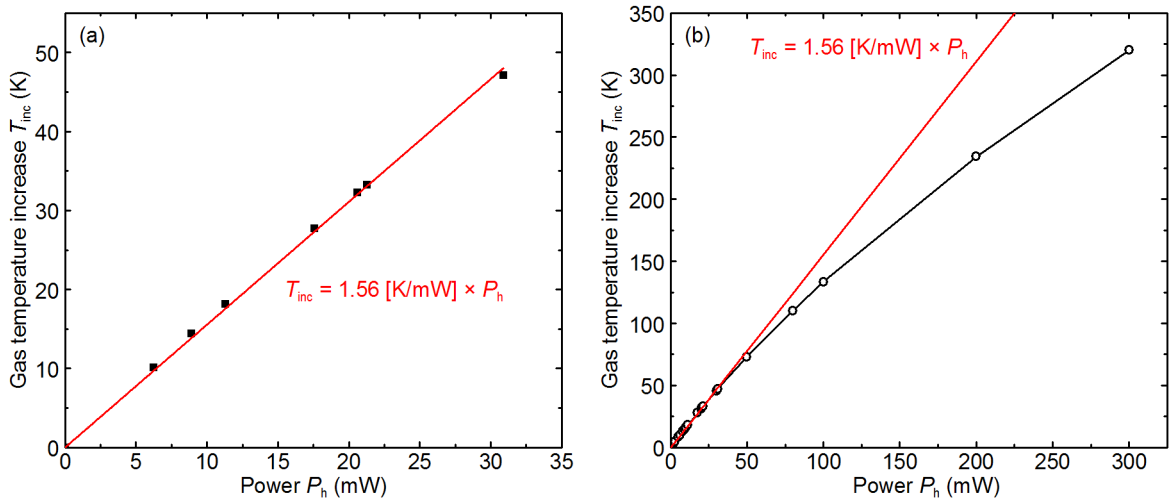

Figure 2.12 (a) Dependency of T_{inc} calculated in the thermal simulation as a function of P_h at T_d = 300 K in P_h range of experimental condition 1C with regression line. (b) That in wide P_h range with extrapolation of the regression line in (a).

2.2.2.3 Simulation results in metal electrodes with diameter of 15 mm (Metal-2)

Using Metal-2 electrodes, the experiments of time-resolved OES were conducted at two T_d conditions: T_d = 5 K(condition 2A) and 40 K (condition 2B). The power consumption P_c was estimated from the measurements of voltage and current waveforms shown in Figure 2.6 and, as a result, the values of P_c were 69 mW for condition 2A and 65 mW for condition 2B. The experimental conditions are indicated in section 2.1.4.2 in detail.

Figure 2.13 shows the contour plot of calculation results of the increase of plasma gas temperature ($T_{inc} = T_g - T_d$) at 5 K with the power P_h of 69 mW. The contour plot and the dependency of T_{inc} on the radius r at the line of $z = 0$ implied that T_{inc} was considerably high while the temperature at the boundary of the calculation area kept constant at T_d. The increment of T_g at the edge of the plasma was estimated to be approximately 30 – 40% lower than that at the center of the plasma. The temporal variation of T_{inc} at the center of the plasma region was plotted at Figure 2.14. The rapid increase of T_g occurred at the shorter time than 0.1 s and, after that, T_{inc} increased linearly with time. The almost all measurements conducted within 100 s and the increment of T_g from 0.1 to 100 s was within 20% of that from ignition to 0.1 s.

For the geometries of Metal-1 electrodes, the thermal simulations were conducted at several conditions, not only at the experimental conditions 2A and 2B, because the time-integrated OES was conducted at several conditions. From the simulation, the dependency of T_{inc} on P_h and T_g. Figure 2.15 shows the calculation results of T_{inc} at four T_d conditions (T_d = 5, 20, 40, and 60 K). The figure implied that the T_{inc} was larger at lower T_g. This is due to the isobaric specific heat and the thermal conductivities are smaller at lower T_g.

In this study, T_g was obtained at the center of the plasma 0.1 s after plasma ignition. At η = 1, the estimated T_g for conditions 2A and 2B are 28 K and 54 K, respectively.

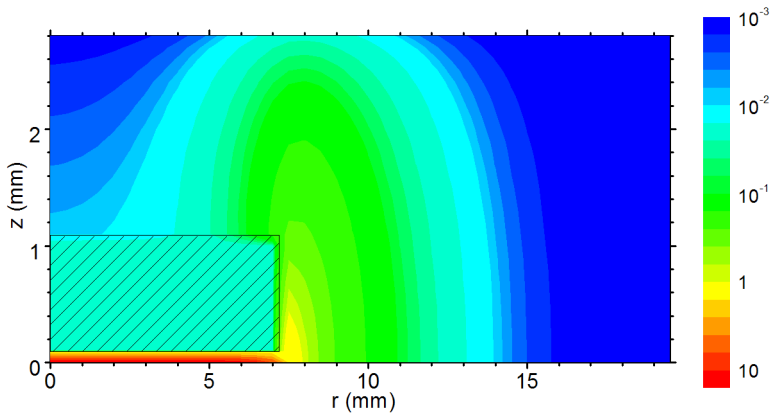

Figure 2.13 Contour plot of increase of T_g (T_{inc}) compared to T_d = 5 K at 1 s after plasma ignition in Metal-1 electrodes. The legend of colors are indicated in the right side of the figure (unit: K) and note that the scale is logarithmic. The shaded portion indicates the region of the electrodes.

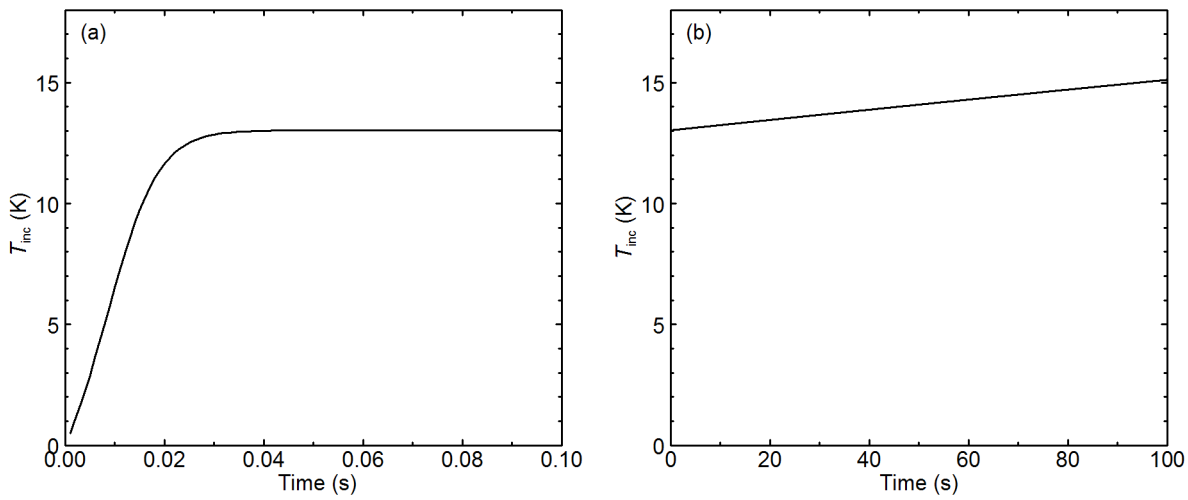

Figure 2.14 Time variation of T_{inc} at T_d = 5 K (a) from plasma ignition (time t = 0) to t = 0.1 s, and (b) from t = 0 to 100 s.

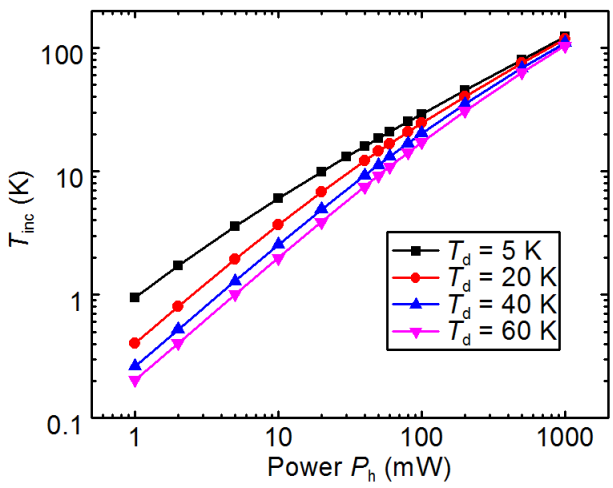

Figure 2.15 T_{inc} at T_d = 5, 20, 40, and 60 K as a function of power P_h in Metal-2 electrodes.

2.2.2.4 Simulation results in DBD electrodes

The U and I waveforms in the DBD electrodes at 14 K (condition 3A) were shown in Figure 2.16(a). Figure 2.16(b) indicates the Lissajous figures at three temperatures of the experimental conditions 3A, 3B, and 3C. The areas of the Lissajous figures indicate the energy consumption in one cycle of the applied frequency and the power consumptions P_c were estimated as 15.3, 24, and 22 mW for 14, 100, and 300 K, respectively. The experimental conditions are introduced in detail in section 2.1.4.3.

The thermal simulation results of T_{inc} were indicated as a contour plot in Figure 2.17. When we assume that all

electric power contributes exclusively to the increase of the gas temperature (i.e. $\eta = 1$), the calculation results of T_g at the center of the plasma and 0.1 s after the ignition were $T_g = 31$ K at $T_d = 14$ K, $T_g = 114$ K at $T_d = 100$ K, and $T_g = 307$ K at $T_d = 300$ K. Therefore, the T_g ranges for each T_d condition were identified in our target ranges of pure He ($T_d = 14$ K), He with N_2 and O_2 impurities ($T_d = 100$ K), and He with N_2, O_2, and water impurities ($T_d = 300$ K) in the experiments shown in Figure 2.1.

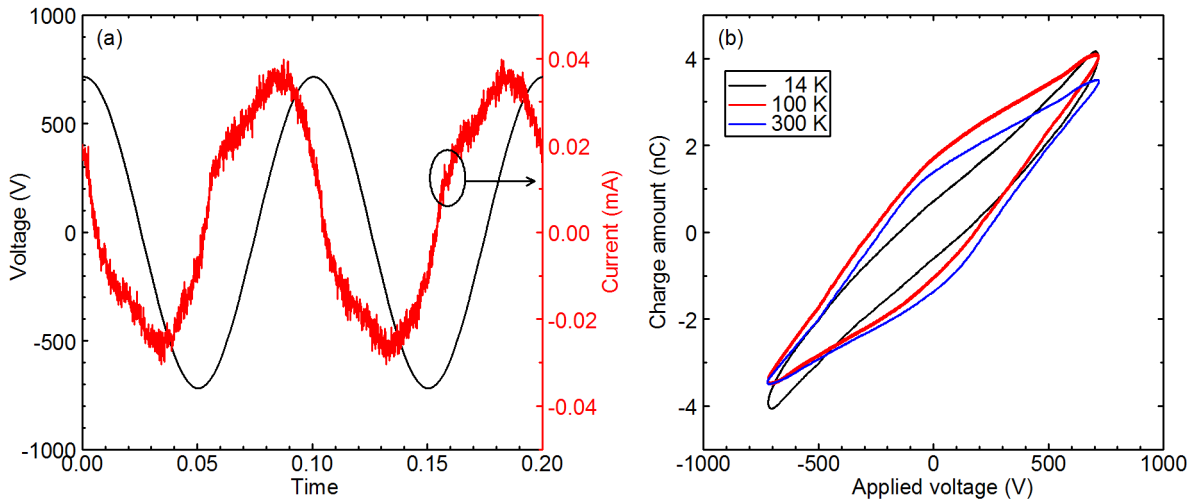

Figure 2.16 (a) Voltage and current waveforms at 14 K and (b) Lissajous figures at 14, 100, and 300 K.

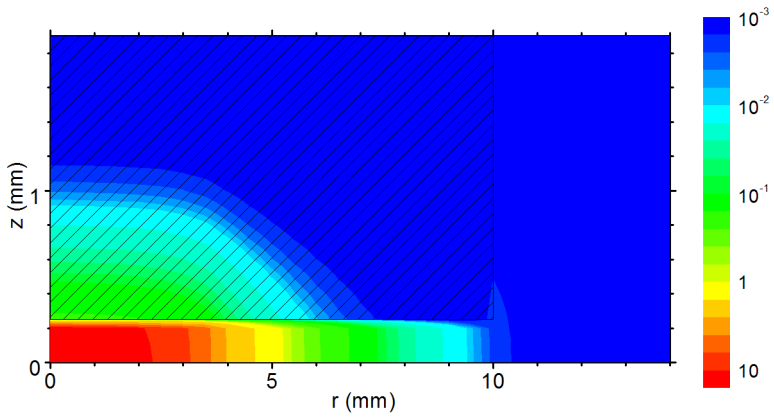

Figure 2.17 The contour plot of the increase of T_g (T_{inc}) at 14 K on the calculation geometry. The shaded portion was the region of the electrodes.

2.2.3 Discussion on evaluation of T_g from LI and thermal simulation

The results of the LI and the thermal simulations are discussed in this section. The discussion are for Metal-1 electrodes in which both LI and simulation were conducted. The values of T_g for conditions 1A, 1B, and 1C (of P_h = 31 mW) were evaluated as 104, 202.5, 304.2 K by LI, and 179, 230, and 347 K by the thermal simulation, respectively. The values of C_{TP} were 0.13 K mW^{-1}, 0.17 K mW^{-1}, and 0.14 K mW^{-1} by LI, and 2.5 K mW^{-1}, 2.0 K mW^{-1}, and 1.6 K mW^{-1} by the thermal simulation, respectively.

There were a large difference between the values of T_g estimated by two methods. Here, the problems and issues of each methods are discussed. In the LI measurements, (a) the assumption of identical pressures inside and outside plasmas, (b) the assumption of the homogeneous spatial distribution of T_g, and (c) the assumption of the constant refractive index independent of λ_0 (dispersion relation was ignored), were adopted.

Regarding the assumption (a), the difference of pressure between inside and outside plasmas should become to decrease to almost zero after an enough time passed from plasma ignition. In the measurements, the phase shift was stable within ON time. In the preliminary measurements with longer ON time, the magnitude of phase shift did not show significant change. In addition, the variation of phase shift of laser beam within a cycle of applied sinusoidal voltage were lower than the detecting limit. Moreover, since discharge currents were continuous and did not show a drastic temporal change such as pulse (spike) discharges, the fluid pressure is almost stable in the period of the applied voltage. Therefore, I conclude that, although the assumption (a) might not be strictly valid, the error due to the assumption should be less than twice. To evaluate the assumption quantitatively, the numerical fluid simulation will be necessary.

Then, concerning the assumption (b), the temperatures were calculated using l = 3.4 mm, which was twice as the diameter of the electrodes. As shown in section 2.2.2.2, there should be a distribution of T_g in plasma region as estimated by the thermal simulation and the difference of T_g between the center and the edge of the plasma was about 1.5 times of magnitude. In the assumption of homogeneous distribution, the estimated value of T_g indicates approximately the average value within the plasma region. Although the difference between the estimated value in LI and the simulation can be caused by this averaging treatment, it was not enough to explain the difference obtained in this study. The length of laser beam passed in plasma, l = 3.4 mm in this study, might not be accurate, although the appearance of the plasmas generated in Metal-1 electrodes was confirmed to be homogeneous by a photograph and the plasma was spread to the edge of the electrodes. In addition, the position of the laser beam was confirmed to be a center of the cryoplasma by scanning the position of it using X-Y stage. However, even if the value of l = 3.4 mm was not accurate for the evaluation of average T_g because the actual radius of plasma did not fully filled between electrodes, the value of l should not be much smaller than 3.4 mm. For example, while it might be possible that a half of 3.4 mm should be used, 1/10 of 3.4 mm should not be suitable for this experiment obviously. If the half value was used for l, the difference of refractive index ΔN_p would became twice, which means that T_{inc} became almost twice. In addition, if the diameter of laser beam had been comparable or larger than the size of plasmas, the signal would have been unreliable. But the diameter of laser beam (less than a few hundreds of μm) was enough small compared to the size of

plasmas (ϕ 1.7 mm × 0.5 mm).

For the assumption (c), the dependency of N_p can be approximated as $N_p \propto 1 + B_{DR} / \lambda_0^2$ where B_{DR} is a constant that depend on the gas species, and for He, B_{DR} is reported to be 2.3×10^{-15} m^{-2} [31]. On the other hand, the values in Table 2.6 are calculated from the square root of relative permittivity in the database of REFPROP [26]. If the calculated N_p values from REFPROP are for the standard wavelength of 589 nm, which is the emission peak of sodium (Na), then the refractive index for λ_0 = 1550 nm is only ~1.006 times lower than that for 589 nm. Therefore, for the calculation of ΔN_p, it is concluded that the effect of the dispersion relation was not dominant.

Therefore, I conclude that the difference between the evaluated T_{inc} by LI and thermal simulation could not be explained by the problems of the LI measurement, although the values of T_{inc} which were evaluated by LI might be a few times larger or smaller than the shown values in section 2.2.1.2.

On the other hand, in the thermal simulation, a heat transfer due to convection was excluded and $\eta = 1$ was assumed. If the effect of convection was taken into account, the T_{inc} should be smaller because the heat transfer between inside and outside plasmas were enhanced. Concerning the energy efficiency η, other ways to consume applied energy were a radiation loss, an electrode heating not via heating of plasma gas and dissipation of high-potential-energy species to ambient gases. While the effects of these components were difficult to be estimated, the effect of convection should be included in the simulation model and the value of η might be an order of 0.1. Therefore, the thermal simulation in this study was useful to estimate the maximum possible value of T_g, but the actual T_g was probably around quarter of the estimated T_{inc} by the thermal simulation or less.

As a result, the results of the thermal simulation indicate the maximum possible T_{inc}, and the actual T_{inc} was closer to the estimated T_{inc} by LI. The more accurate estimation of T_{inc} for cryoplasmas still needed to be developed.

In following, the values of T_g evaluated by thermal simulation were used because the evaluation by LI could not conduct for Metal-2 and DBD electrodes, and note that T_g imply the maximum possible values.

2.3 Dependency of spectra and temporal variation of optical emission

We conducted both time-integrated OES (TI-OES) and time-resolved OES (TR-OES) measurements. Optical emission spectra were measured using a spectrometer (SpectraPro 300i, Acton Research) and an intensified charge-coupled device camera (PI-MAX 512, Princeton Instruments). In TI-OES, we observed the wavelength range from 300 to 800 nm with an exposure time of over 1 ms. In contrast, in TR-OES, the emission intensities of specific species were measured every 0.5 μs at a total of 100 points in each sinusoidal cycle, with an exposure time of 0.5 μs.

First, the main characteristics of the emission spectra were investigated by TI-OES measurement, and then the time variations of the peak intensity of specific emission peaks were measured by TR-OES. As presented in Table 2.1, TI-OES was conducted for Metal-2 and DBD electrodes, and TR-OES was conducted for only Metal-2 electrodes.

2.3.1 Time-integrated OES (TI-OES)

2.3.1.1 Variation of TI-OES for DBD electrodes in wide T_g range

For understanding the basic properties of the DBD cryoplasma, we took photographs (Figure 2.19) and spatio-temporally averaged optical emission spectra (Figure 2.18). The T_d conditions for the discharge images were T_d = 300 K [Figure 2.19 (a)], T_d = 100 K [Figure 2.19 (b)], and T_d = 14 K [Figure 2.19 (c)], all images having been acquired with a 0.01-s shutter speed. Figure 2.19(d) shows the electrode and plasma structures taken at T_d = 300 K with a 1-s shutter speed. As T_d decreased, we could observe that the plasma color changed between purple [at T_d = 300 K, Figure 2.19 (a)], blue [T_d = 100 K, Figure 2.19 (b)], and red [T_d = 14 K, Figure 2.19 (c)] and the plasma structure and its stability were similar for the three T_d conditions.

The color change with the T_d decrease suggested a change of major emissive excited species generated in the plasma, as shown in Figure 2.18. At T_d = 300 K, we observed OH [309 nm ($A\,^2\Sigma^+ - X\,^2\Pi$)] and N_2 [337.1 nm ($C^3\Pi - B^3\Pi$, second positive system)] molecular emissions in the near ultraviolet range, in addition to visible N_2^+ ($B^2\Sigma_u^+ - X^2\Sigma_g^+$, first negative system) molecular and He I atomic emission lines [32,33]. The OH and N_2 emissions disappeared and near infrared O I ($3^5P_{1,2,3} - 3^5S_2$) emission at 777 nm became strong in the spectrum taken at T_d = 100 K. A reason for the absence of OH emission at T_d = 100 K is the freezing of water impurities in such a low T_d condition. When we decrease T_d sufficiently lower than the boiling temperatures of N_2 and O_2 (77 K for N_2 and 90 K for O_2 [34]), as shown in the data taken at T_d = 14 K, only emission lines of the He atom [707 nm ($3^3S_0 - 2^3P_{0,1,2}$), and 728 nm ($3^1S_0 - 2^1P_1$)], and the He_2 dimer ($d^3\Sigma_u^+ - b^3\Sigma_g^+$, 640 nm) in the red region could be observed. The relationships of the gas temperature, the boiling points of He and air impurities, and the T_d conditions used in this study are summarized in Figure 2.18 (e).

The variations of colors and emission spectra of cryoplasmas depending on T_g have been discussed in the previous studies [3,7] and the behavior in this study was similar to them.

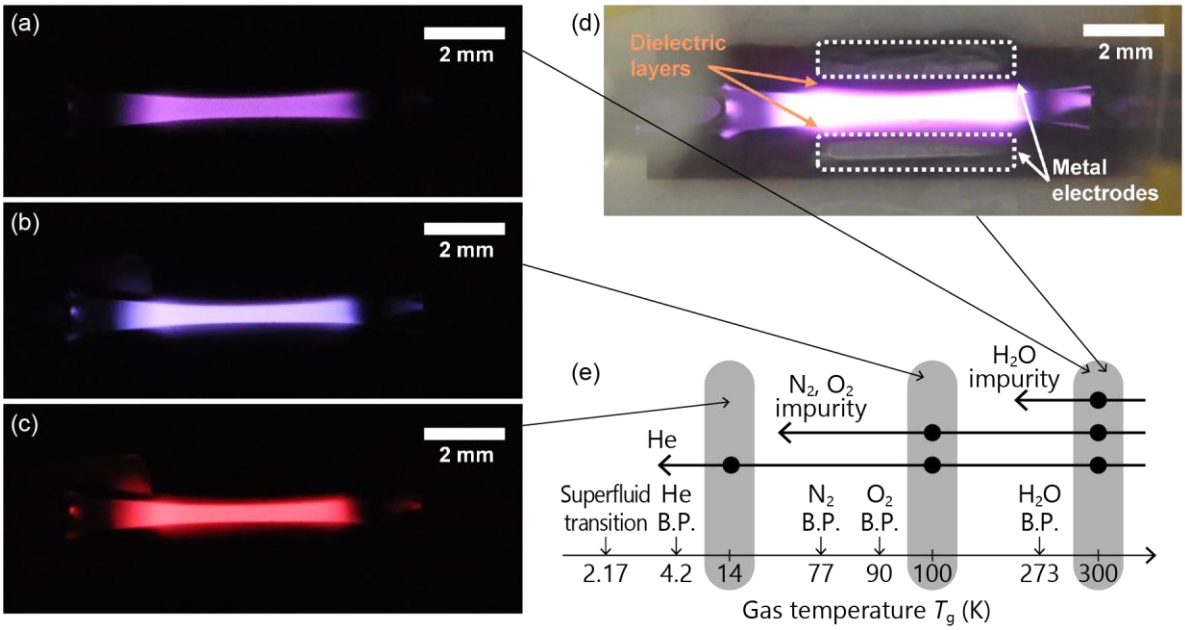

Figure 2.19 Photographs of the discharge emissions recorded by a digital camera at (a) T_d = 300 K, (b) T_d = 100 K, and (c) T_d = 14 K, and (d) structure of the parallel-plate DBD electrode placed in the cryoplasma chamber. The exposure times for each photograph were 0.01 s for (a), (b), and (c), and 1 s for (d), respectively. (e) Temperatures, where the photos were taken, added to Figure 2.1.

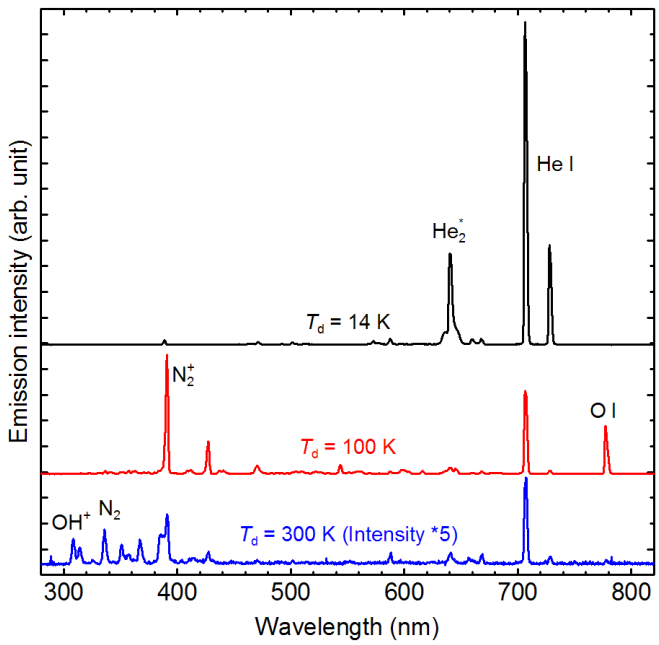

Figure 2.18 Spatio-temporal integral optical emission spectra in the wavelength range from 300 to 800 nm measured at T_d = 300 K (bottom blue line), T_d = 100 K (middle red line), and T_d = 14 K (top black line). The spectra at T_d = 100 and 14 K are offset and that at T_d = 300 K is enlarged five times for ease of comparison.

2.3.1.2 Variation of TI-OES of Metal-2 electrodes below 50 K

Figure 2.20 shows time-integrated optical emission spectra measured at T_d = 5 K (T_g = 18 K, P_c = 28 mW, thick black line) and T_d = 40 K (T_g = 41 K, P_c = 2 mW, thin red line) in condition 2TI in Table 2.3. Although the experimental condition of Figure 2.20 differed from conditions 2A and 2B such as T_g and P_c, the shapes of the spectra in conditions 2A and 2B should be similar to those in Figure 2.20. At T_d = 5 K, all emission peaks originated from He or He_2, for instance, the emission peaks at 728.1 nm (He), 706.5 nm (He), and 640.0 nm (He_2). These strong emission peaks were in the near infrared or red. On the other hand, at T_d = 40 K, there were many emission peaks from air impurity species such as at 391.4 nm (N_2^+), 337.1 nm (N_2), and 777.1 nm (O). These peaks from N_2 or O were generated by impurities remaining after incomplete elimination and mainly have shorter wavelengths (300 – 500 nm), which emit in the blue or purple. This difference in the emission intensity of N_2 and N_2^+ caused a color change of the plasmas: red at T_d = 5 K and blue or purple at T_d = 40 K.

The variation of relative emission intensities of He_2, N_2^+, N_2 and O compared to He emission peak are indicated in Figure 2.21. Below 35 K, the emissions from impurity species were not observed. At T_d = 35 K, the emission of N_2^+ appear. Then at T_d = 40 K, the emissions of N_2 and O_2 began to be observed, however, the emission intensity of O_2 was still small at 45 K. The difference of T_d which appear N_2^+ and O_2 were probably due to the difference of sublimation pressures of N_2 and O_2 (see Figure 2.29). The dependency of relative emission intensity of He_2 showed a maximum around T_d = 15 K, but the reason for this was not clarified.

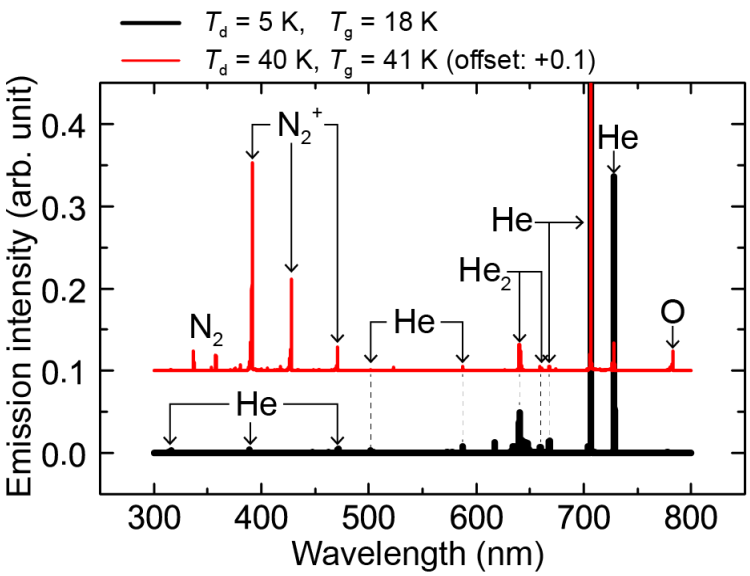

Figure 2.20 Time-integrated optical emission spectra of cryoplasmas at T_d = 5 K (T_g = 18 K, black line) and T_d = 40 K (T_g = 41 K, red line). The emission intensities were normalized with respect to the He emission line at 706.5 nm and the spectra at T_d = 40 K was offset by +0.1.

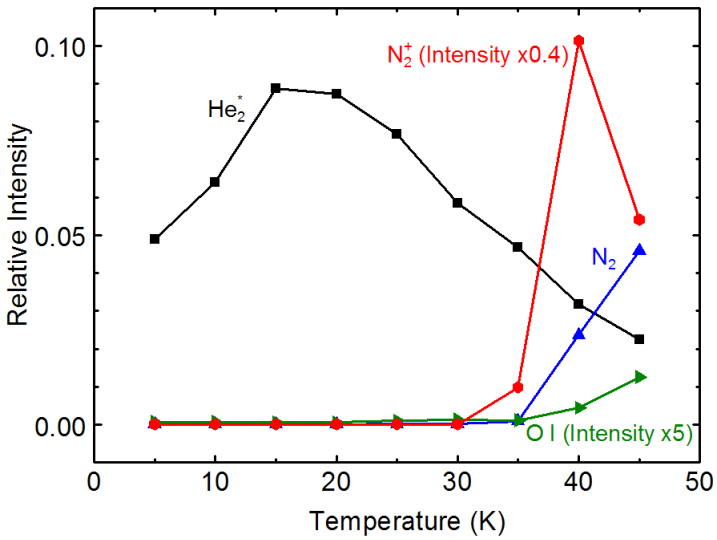

Figure 2.21 Relative time-integrated optical emission intensity of He_2 (640.0 nm), N_2^+ (391.4 nm), N_2 (331.7 nm), and O (777.1 nm) as a function of T_d. The emission intensities were normalized with respect to the He emission line at 706.5 nm.

2.3.2 Time-resolved OES (TR-OES)

The time variations of the relative emission intensities at condition 2A (T_d = 5 K, T_g = 28 K) and condition 2B (T_d = 40 K, T_g = 54 K) are shown in Figure 2.22(a) and Figure 2.22(b), respectively, along with the waveforms of the discharge current (black line). The emissive species shown in Figure 2.22 are He (706.5 nm, solid red line) and He_2 (640.0 nm, dotted blue line), and that in Figure 2.22(b) are He (706.5 nm), He_2 (640.0 nm), and N_2^+ (391.4 nm, short dashed green line).

Under condition A [Figure 2.22(a)], the He and He_2 emission peak intensities increased with *I*; however, the He peak intensity decreased more rapidly than *I*. In other words, in spite of there being no emission, *I* lasted until the voltage reached almost zero. This result will be discussed in section 2.6.1.1.

For condition B [Figure 2.22(b)], when the current started increasing, the He emission at 706.5 nm increased with the current. On the other hand, the N_2^+ emission started increasing in intensity with a delay of approximately 8 μs relative to the peak He emission. With the sudden decrease in the current, the N_2^+ emission intensity decreased; however, it did not reach zero and still persisted with an intensity of 1/2 – 1/3 of the maximum intensity. We discuss the delay of the N_2^+ emission on the basis of a numerical model in section 2.6.1.2.

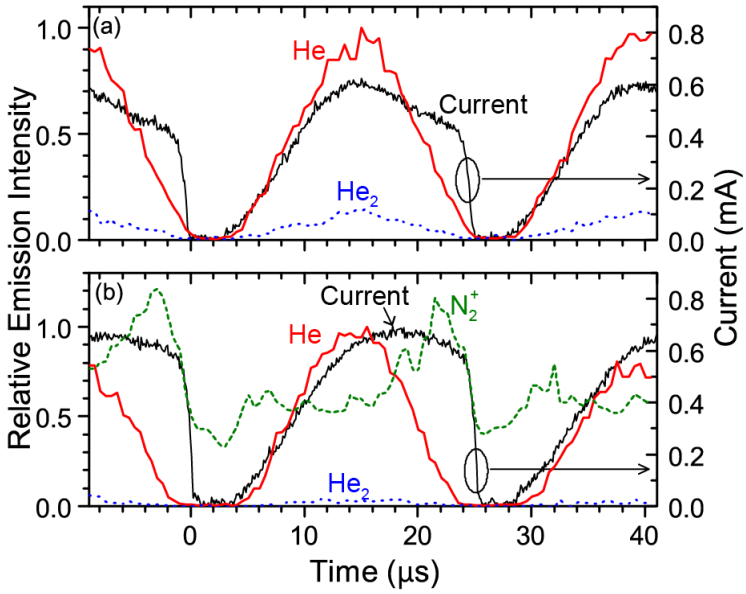

Figure 2.22 Time variations of relative emission intensities of He (706.5 nm, solid red line), He_2 (640.0 nm, dotted blue line), and N_2^+ (391.4 nm, short dashed green line) measured at (a) condition A (T_d = 5 K, T_g = 28 K) and (b) condition B (T_d = 40 K, T_g = 54 K). In addition, the absolute values of the discharge current of each temperature are shown as thin black lines. The emission intensities were normalized with respect to the maximum intensity of He emission at 706.5 nm. The zero point of the time scale is defined where U = 0.

2.4 Density measurements of helium metastable atom by laser absorption spectroscopy (LAS)

2.4.1 Laser absorption spectroscopy (LAS)

We used the LAS method to measure temporal density variations of He^m atoms in the 2^3S_1 state inside the DBD mainly for the discussion of He^m quenching processes. The LAS setup is shown in Figure 2.23. A probing laser beam at a wavelength around 1083 nm from an external-cavity diode laser was absorbed in the $2^3S_1 - 2^3P_J$ (J = 0, 1, and 2) transition. In our LAS measurement for the He^m atoms, the values of the wavelength λ_0 and the identical frequency ν_0 for He $2^3S_1 - 2^3P_J$ (J = 0, 1, and 2) transitions are 1082.909 nm and 276840 GHz for J = 0, 1083.025 nm and 276810 GHz for J = 1, and 1083.034 nm and 276808 GHz for J = 2, respectively [32]. The laser wavelength was monitored by a wavelength meter and controlled by a piezo actuator installed in the external cavity. An optical isolator was placed in the laser beam axis to prevent return light and to enable stable laser oscillation. The laser beam was aligned with a visible red diode laser with its axis set to the same as the probing laser beam. The probing beam passing through a half-mirror cube was inserted into the plasma cell and focused on a mirror behind the DBD electrode. The reflected laser beam was picked up at the half-mirror cube and focused on to an InGaAs photodetector with a response speed of ~10 ns. The reflection configuration was necessary for the laser spectroscopic diagnostics of the cryoplasma since the plasma cell used for the cryogenic T_g operation had only one small optical port to prevent heat influxes.

In the LAS measurement, the laser-beam absorbance, $-\ln(I_T/I_0)$, where I_T and I_0 are the transmitted and the incident probing laser-beam intensities, respectively, is proportional to the line-integrated density of He^m along the laser path based on Lambert-Beer's law. We calculated the absolute He^m density from the measurement results of absorbance and broadening parameters, similar to previous studies [35,36].

The absorbance is related to the absorption coefficient k, which depends on the position along the laser beam path (y) and the laser frequency (ν), as shown in the following equation (Lambert-Beer law),

$$-\ln\left(\frac{I_T(\nu)}{I_0(\nu)}\right) = \int_0^l k(y,\nu)dy \tag{2. 12}$$

where l is the length of the plasma along the laser beam path. For the LAS measurements of He^m around the wavelength of 1083 nm, the absorption coefficient k is the sum of the absorption coefficient of three transitions of $2^3S_1 - 2^3P_J$ (J = 0, 1, and 2). Among the absorption coefficients owing to the transition of $2^3S_1 - 2^3P_J$ (k_J), k_J is proportional to the statistical weight of the upper f state of 2^3P_J [$g_f(J)$ = 1, 3, and 5 for J = 0, 1, and 2, respectively]. Therefore, the value of k is expressed as

$$k(y,\nu) = \sum_{J'=0}^{2} k_{J'}(y,\nu) = \frac{\sum_{J'=0}^{2} g_f(J')}{g_f(J)} k_J(y,\nu) = \frac{9}{g_f(J)} k_J(y,\nu). \tag{2. 13}$$

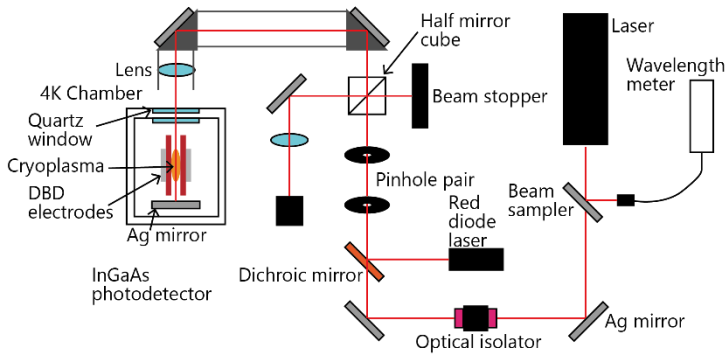

Figure 2.23 Experimental setup of laser absorption spectroscopy (LAS) for the dielectric barrier discharge (DBD) cryoplasma. The probing external-cavity diode laser beam was at a wavelength of 1083 nm and the beam axis was set using another visible laser beam that merged at a dichroic mirror. The probing beam passed through the plasma source twice before and after reflection at a mirror placed behind the electrode. The probing laser beam returning from the DBD cryoplasma chamber was separated from the forward beam at a half mirror cube and its intensity was measured by an InGaAs photodetector.

The absolute density of He^m (2^3S_1) atoms (n_m) is expressed as

$$n_{\mathrm{m}}(y) = \frac{c}{h\nu B_{if}(J)} \int k_J(y,\nu)d\nu \tag{2. 14}$$

where c is the speed of light, h the Planck constant, λ_0 the wavelength of light, and $B_{if}(J)$ is the Einstein coefficient for photo absorption transition of 2^3S_1–2^3P_J, which can be expressed as [23]

$$B_{if}(J) = \frac{\lambda_0^3}{8\pi h}\frac{g_f(J)}{g_i}A_{fi} \tag{2. 15}$$

where g_i (= 3) is the statistical weight of the lower i state, A_{fi} the transition probability from upper f state to lower i state which is called as Einstein's A coefficient. The value of A_{fi} for the 2^3S_1–2^3P_J transitions is 1.0216×10^7 Hz [32]. Then, the following equation is obtained from equations from (2. 12) to (2. 15):

$$\int_0^l n_m(y)dy = \frac{8\pi}{3\lambda_0^2 A_{fi}} \int -\ln\left(\frac{I_{\mathrm{T}}(\nu)}{I_0(\nu)}\right) d\nu \tag{2. 16}$$

To calculate the integral of the measured absorbance, the absorption spectrum was fit with Voigt function. In the fitting, only the Doppler broadening, which depends on gas temperature, was considered as the Gaussian component. Note that the pressure broadening is the dominant factor in the Lorentzian component.

For the situation where the gas composition is uniform and the absorption line profile does not change along the laser path, the left component of equation (2. 16) is expressed as $n_m \times l$. In addition, under an identical condition where

both Gaussian and Lorentzian components of spectra broadening does not change, the ratio (C_{abs}) of the absorbance at specific laser frequency to the integral of the measured absorbance can be expressed as a function of the laser frequency ν. Therefore, after once $C_{abs}(\nu)$ is measured in the condition, n_m is calculated by using absorbance at one frequency, without the integral of the absorbance. Finally, the value of n_m is expressed as

$$n_m = -\frac{8\pi}{3l\lambda_0^2 A_{fi}} C_{\mathrm{abs}}(\nu) \ln\left(\frac{I_{\mathrm{T}}(\nu)}{I_0(\nu)}\right) \tag{2. 17}$$

However, for conditions of temperature much lower than RT, we had to consider the saturation effect on the measurement due to the dynamic variation of the He^m lifetime. The details of the discussion on the saturation of absorption for each T_g condition are introduced in section 2.4.3.

2.4.2 LAS in DBD electrodes

Experimental conditions for LAS measurements in DBD were listed in Table 2.4. For the evaluation of He^m lifetimes in the cryoplasmas, we measured the temporal decays of the absorbance $-\ln(I_T/I_0)$ at the three T_d conditions, as shown in Figure 2.24. The difference between Figure 2.24(a) and (b) is the horizontal time-axis scale, while the data for these two Figures are the same. All data are normalized in amplitude, with the time origin set at the starting point of the absorbance decay after the final discharge pulse of the burst operation. The wavelengths of the probing laser for each T_d measurement were 1083.035 nm for T_d = 300 K [green line, plotted only in Figure 2.24(a) because of its short lifetime], 1082.910 nm for T_d = 100 K [blue lines, both in Figure 2.24(a) and (b)], and 1082.945 nm for T_d = 14 K [red lines, both in Figure 2.24(a) and (b)]. The reason why the probing-laser wavelengths are different for each T_d condition is to preserve the linearity between the absorbance and the He^m density at lower T_d conditions (see section 2.4.3). In Figure 2.24(a), it can be seen that the He^m lifetime became significantly longer with decreasing T_d. Since the absorbance decay measured at T_d = 14 K was too slow to fit into one Figure with that at T_d = 300 K, we plotted the absorbance data at T_d = 14 K and that at T_d = 100 K over a longer period in Figure 2.24(b). The decay times of the absorbance t_d, which here is defined as the time length for an absorbance decay from 1 to 1/e, were $t_d = 5.9 \times 10^{-7}$ s for T_d = 300 K, $t_d = 6.5 \times 10^{-6}$ s for T_d = 100 K, and $t_d = 1.8 \times 10^{-4}$ s for T_d = 14 K. Comparing t_d for lower T_d conditions with t_d at T_d = 300 K, t_d became ~10 times longer at T_d = 100 K and ~300 times at T_d = 14 K. This result suggests that the He^m quenching reaction slows drastically by a decrease of T_d, and this dynamic t_d variation cannot be explained only by a change of the collision frequency, which is basically proportional to $T_g^{0.5}$ for two-body reactions.

Figure 2.25 shows the temporal evolution of the absolute He^m density with the applied voltage U and current I. The basic method is explained in section 2.4.1 and the actual calculation of the absolute He^m density considering saturation effect and its possible inaccuracy are explained in section 2.4.3. From the result, the He^m density drastically increased with decreasing T_d, showing a good qualitative agreement with the increase of the He^m lifetime. At T_d = 14 K [Figure 2.25(a)], the maximum and minimum He^m densities were 1.4×10^{12} and 1.0×10^{12} cm^{-3} respectively; whereas, for higher-temperature conditions at T_d = 100 K [Figure 2.25(b)], the He^m density decreases at every cycle much more

rapidly compared to T_d = 14 K, however, it did not reach values below the detection limit during the voltage-ON time in the burst operation. The peak density at T_d = 100 K was 1.8×10^{11} cm^{-3}. At T_d = 300 K, the He^m density reached 5.3×10^{10} cm^{-3} in a very short time and the pulse width of the He^m appearance was shorter than 5 μs [Figure 2.25(c)]. The He^m density decreased below the detection limit just after the rising in each discharge pulse at T_d = 300 K. Due to the long He^m lifetime at lower T_d conditions revealed in Figure 2.24, the absolute He^m density and its temporal evolution varied significantly with the T_d decrease. This result suggests that it is possible to control the absolute He^m density simply by changing the gas temperature, owing to the variation in the He^m lifetime.

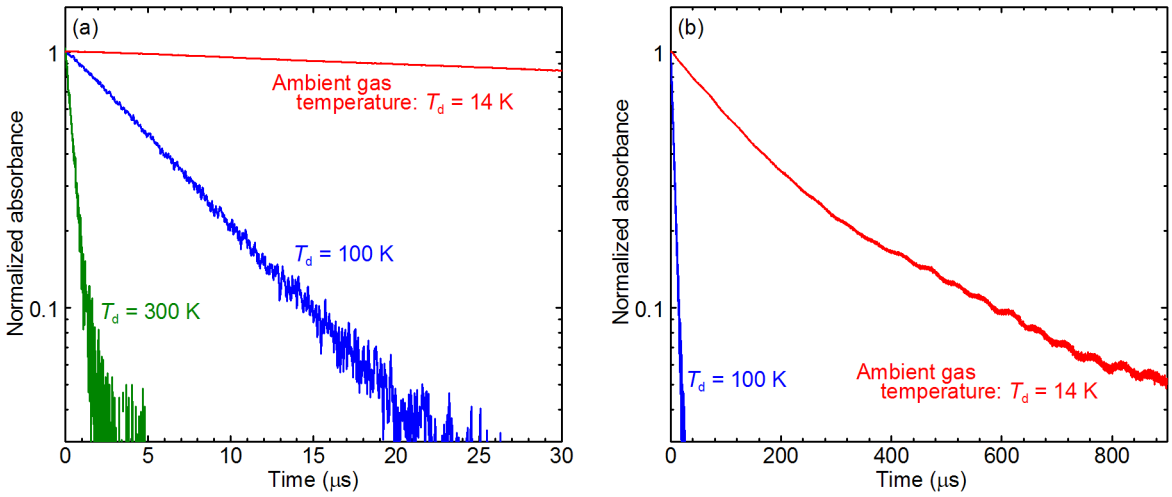

Figure 2.24 Temporal evolution of normalized absorbance in the afterglow of helium metastable 2^3S_1 (He^m) atoms measured at T_d = 300 K (green line), T_d = 100 K (blue line), and T_d = 14 K (red line). (a) shows a short time range for the analysis of T_d = 300 and 100 K, and (b) shows a long time range for T_d = 14 K.

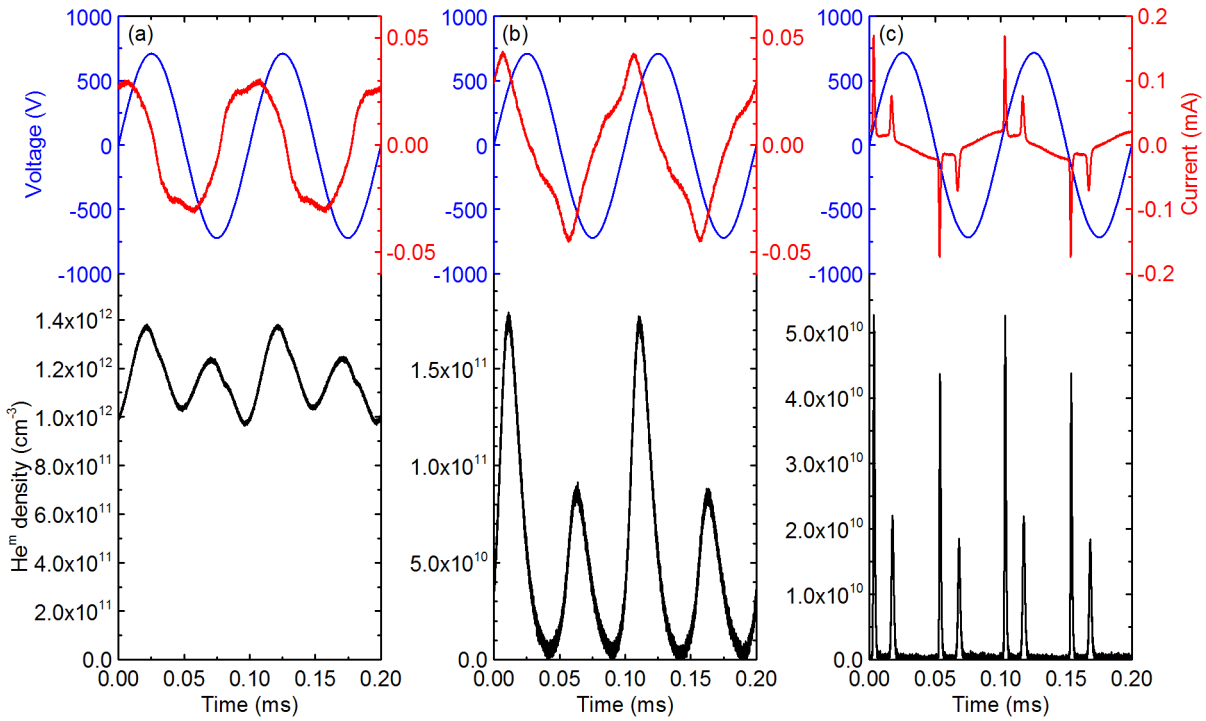

Figure 2.25 Temporal evolution of absolute He^m density, voltage, and current measured in (a) condition 3A (T_d = 14 K), (b) condition 3B (T_d = 100 K), and (c) condition 3C (T_d = 300 K).

2.4.3 Discussion on saturation of absorption

In the LAS measurements, the saturation of absorption occurs when the power of probing laser beam is too high due to a decrease of the density of the lower state. In this section, the treatment of the experimental data considering the saturation of absorption is discussed.

Figure 2.26(a) shows the LAS absorption profile measured at T_d = 300 K and its fit curves using Lorentzian profiles with a full width at half maximum of frequency ($\Delta\nu_L$) of $\Delta\nu_L$ = 13.9 GHz. The profiles for J = 0, 1, and 2 overlapped in such a high-pressure condition; therefore, we had to consider the ratio of absorption for the J = 0, 1, and 2 transitions at a certain frequency, which was used to calculate the absolute He^m density n_m. In the case of T_g = 300 K, we used the absorption at a peak frequency of $2^3S_1 - 2^3P_2$ (J = 2) transition at 276808 GHz for the calculation of n_m. The temporal evolution of n_m shown in Figure 2.25(a) was calculated from the measured temporal evolution of the absorbance at a probing laser frequency of 276808 GHz and under two assumptions. The first was that l = 20 mm (twice the electrode length of 10 mm along the laser path), and the second a homogeneous He^m density distribution.

For the data measured at T_g = 100 K, as shown in Figure 2.26(b), the absorption peak for J = 1 and 2 was smaller than that of a well-fit profile with $\Delta\nu_L$ = 11.0 GHz. This phenomenon is probably due to saturation in the laser absorption. The saturation intensity of the laser absorption I_s is indicated as

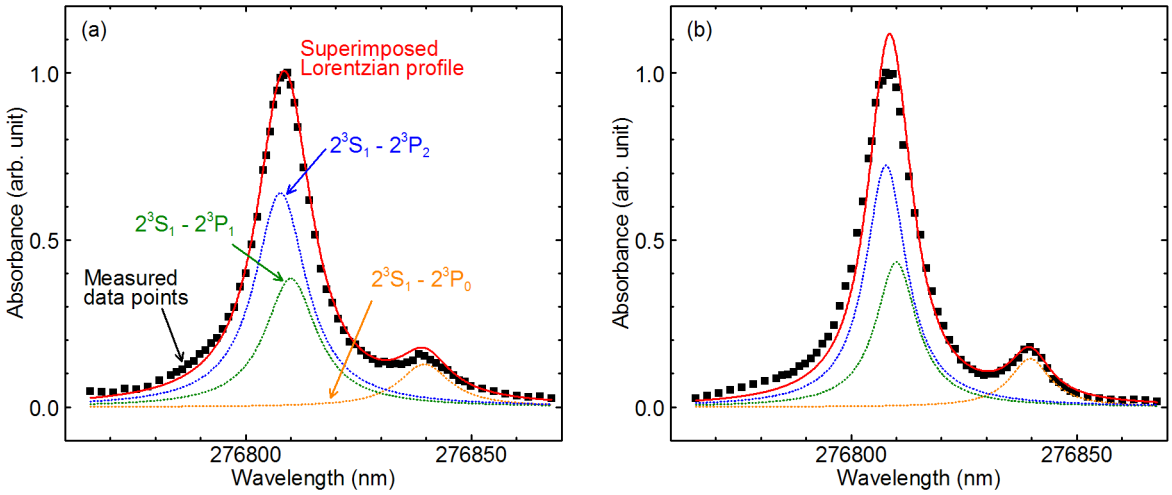

Figure 2.26 Normalized absorption spectra of He 2^3S_1–2^3P_J (J = 0, 1, and 2) transitions measured at (a) T_d = 300 K and (b) T_d = 100 K (black dots). The red solid line is the fitted profile obtained by superposition of the individual Lorentzian profiles of the 2^3S_1–2^3P_0 (orange), 2^3S_1–2^3P_1 (green), and 2^3S_1–2^3P_2 (blue) transitions (indicated by the dotted lines).

$$I_s = \frac{2\sqrt{2}h\nu}{\lambda_0^2}(A_{12} + Q) \tag{2. 18}$$

where Q is the quenching reaction rate of an upper-state atom in the absorption. I_s increases roughly in a proportional fashion with the collision broadening width if it dominates the line profile [37]. In our cryoplasma diagnostics, the quenching rate Q of He^m atom significantly decreased with decreasing T_g as shown in Figure 2.24; therefore, we expect that the I_s for 2^3S_1 – 2^3P_J also decreased with the decrease of T_d, causing a saturation in the cryoplasma measurement. Because of the saturation in the peak for J = 1 and 2, we used the data of the J = 0 peak at 276840 GHz in n_m calculation and its result is shown in Figure 2.25(b). For evaluating the saturation in a quantitative manner, we need data of the quenching rates of the upper state of He 2^3P_J atoms for each measurement temperature; however, this is not possible to be measured in our present experimental setup.

The effect of saturation on the absorption profile became more apparent in the condition at T_d = 14 K. We found that at this temperature, the absorption profiles were affected by the saturation that varied temporally as shown in Figure 2.27(a) and (b), which is different from other higher-temperature conditions, At the time when the voltage reached the peak value [Figure 2.27(a)], we could fit the J = 0 peak with $\Delta\nu_L$ = 7.2 GHz. However, when the applied voltage was around zero [Figure 2.27(b)], the saturation seemed to be affected more significantly even for the J = 0 peak. This temporal change in the absorption profile is due to the temporal change in the gas temperature following the plasma generation. In the case of T_d = 14 K, any small temperature change in the plasma affects much more the quenching rate and the line width, since the temperature doubles for only a 14 K increase. In this paper, for the ease of

calculation, we used only a broadening of 7.2 GHz and the absorbance at 276831 GHz between the J = 0 and 1 peaks avoiding saturation to calculate the absolute He^m density in Figure 2.25(c).

Because of the saturation effect on the absorption profile, the calculated results of the absolute He^m density shown in Figure 2.25 should have corresponding errors of several tens of percent at maximum for lower-temperature conditions, since the measured absorption coefficient k is smaller than the actual value under the saturating condition, and we did not consider the temporal change of the absorption profile at lower temperatures. However, the variation of the calculated absolute densities of He^m atoms for each T_d condition was sufficiently large in comparison to the possible inaccuracy of the LAS measurement; therefore, we conclude that the dynamic signal variation in the LAS measurement when decreasing T_d was caused by the change of lifetime and absolute density of He^m atoms and not by measurement inaccuracies due to saturation. For more accurate measurements avoiding the effects of saturation, it is necessary to set the probing-laser intensity to considerably lower levels than in the present setup, and to install a highly sensitive detecting method of the probing laser intensity, for instance amplitude modulation with a lock-in measurement system, for detecting a probing laser of lower intensity.

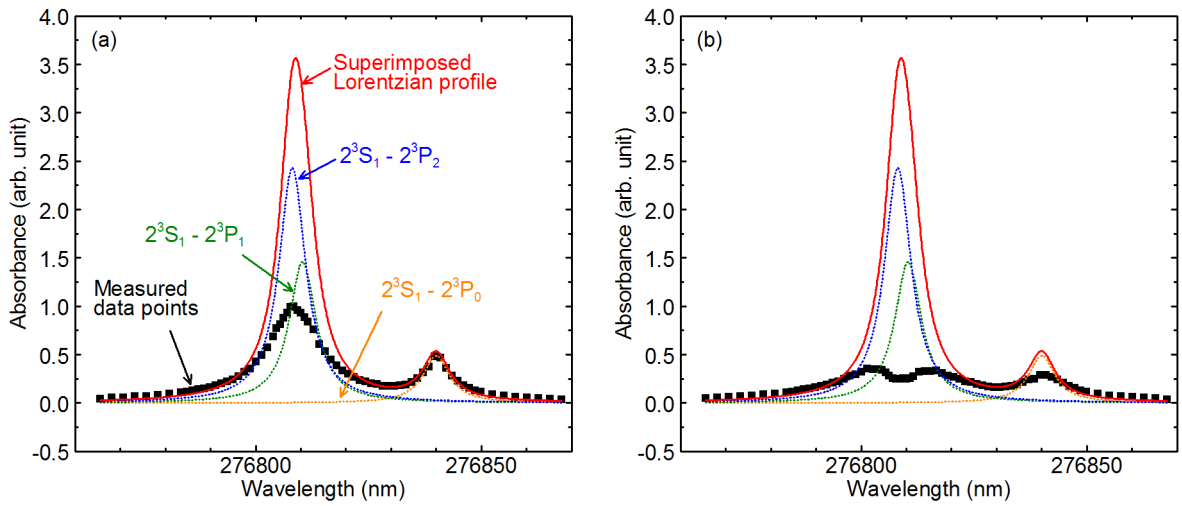

Figure 2.27 Normalized absorption spectra of the He 2^3S_1–2^3P_J (J = 0, 1, and 2) transitions measured at T_d = 14 K (black dots). (a) displays the measured profile at the timing of the positive peak voltage [at 0.02 and 0.12 ms in Figure 2.25(c)], and (b) is at the timing of zero voltage after the positive peak [at 0.05 and 0.15 ms]. The red solid line represents the fitted profile obtained by superposition of each Lorentzian profile of the 2^3S_1–2^3P_0 (orange), 2^3S_1–2^3P_1 (green), and 2^3S_1–2^3P_2 (blue) transitions, respectively, indicated by the dotted lines.

2.5 Gas-temperature dependent reaction model

2.5.1 Basic ideas

In high-temperature plasmas, since chemical reactions in plasmas can be approximated as local equilibrium state, the densities of species and the ratio between each reactions are indicated as a function of T_g (approximately equal to T_e). Meanwhile, chemical reactions in non-equilibrium plasmas are mainly dominated by a part of species having high thermal or potential energies such as electron, ions, and radicals. Plasma chemistry in non-equilibrium plasmas cannot be represented as a function of T_g or T_e simply.

Numerical simulation techniques that take into account reactions and transportation inside plasmas and at plasma boundaries have been widely used for the study of non-equilibrium plasmas. In these simulations, the energies of collision species are important and only electrons have sufficiently high kinetic energies in non-equilibrium plasmas. Consequently, only the electron temperature (T_e) has been considered in most plasma simulations. Meanwhile, the term of T_g was included in representations of only a small part of reaction rate constants and diffusion coefficients. However, the thermal energy of neutral species in plasmas can be expected to be important in elemental reactions that do not include electrons as collision species.

To estimate the reaction dynamics in non-equilibrium plasmas, the elemental reactions are combined and solved. The reaction rate (R) of each elemental reaction is expressed as

$$R = n_a \times n_b (\times n_c) \times k_R \tag{1. 4}$$

where n_a, n_b, and n_c are number densities of reaction species and k_R is a reaction rate constant of the elemental reaction. Here, R indicates the reaction frequency per unit volume and per unit time and called as a reaction rate. In the reaction rate constants k_R, components of a reaction cross section and a collision frequency are included. In addition, transportation of species due to a diffusion and a drift of charged particles due to an electric field. In particular, the dependency of diffusion coefficients of neutral species on T_g are important in transportation. Therefore, the components affected by T_g in plasma chemistry are summarized as: the collision cross section, the collision frequency, the density of collision species, and the diffusion.

2.5.1.1 Reaction cross section σ

At cryogenic T_g, since the balance of collision reactions of heavy species should be different from that at a higher T_g, unique plasma chemistry can be expected. Since the first studies conducted in the 1950s [38,39], considerable knowledge of plasma reactions at cryogenic T_g, particularly in pure helium (He) gas and liquid, has been accumulated [40–49]. These studies reported that certain reaction rates strongly depend on T_g. For example, the reaction rate constant of the metastable He (He^m) conversion reaction strongly depends on the gas temperature [41] as shown in Figure 2.28(a). Figure 2.28(b) shows the potential energy for the combination of He atoms in the 2^3S and 1^1S

states [50] and there is a small hump in the potential energy which results in the existence of the activation energy (~0.067 eV) [40]. This small activation energy can be considered as a cause of the strong dependency of the reaction rate constant of the He^m conversion reaction. In addition, the dependency of the reaction rate constant of an attachment reaction on T_g should be high when the activation energy in the dissociation reaction of the product is low. For example, the attachment reaction of an oxygen atom radical to an oxygen molecule generating ozone in helium shows large dependency on T_g and its reaction rate constant is higher at lower temperature ($O + O_2 + He \rightarrow O_3 + He$, $k_R = 3.4 \times 10^{-34} \exp(T_g/300)^{-1.2}$ cm^6 s^{-1}) [51]. This is because the probability to cause attachment reaction are relatively high at low T_g, while collision frequency is lower due to low T_g.

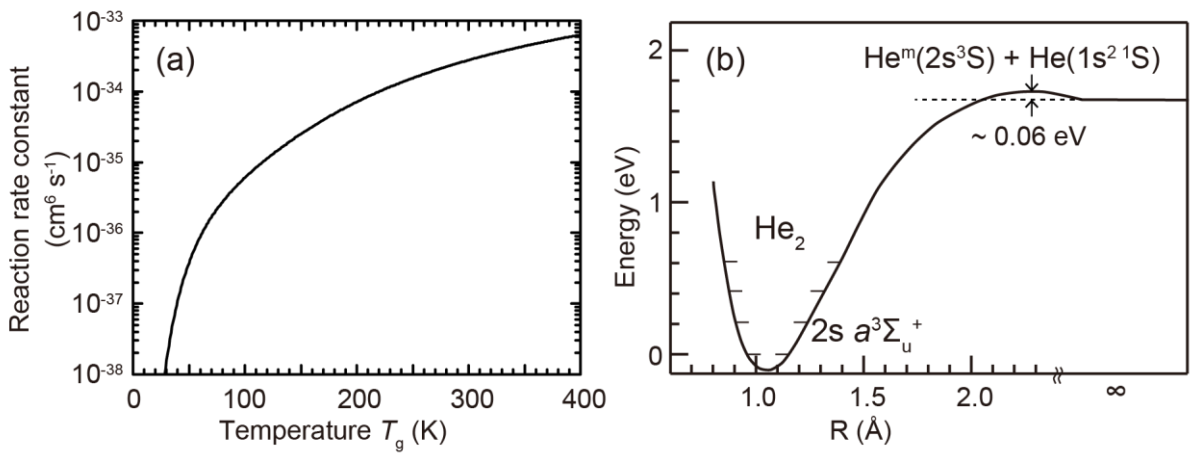

Figure 2.28 (a) Dependency of reaction rate constant on T_g of three body reaction among helium metastable and helium atoms on the gas temperature [41]. (b) Potential curve in the combination of metastable He ($2s^3$S) and ground-state He [50].

2.5.1.2 Collision frequency *f*

Temperature indicate an average kinetic energy of species and simultaneously an average velocity. In the assumption of hard spheres, collision frequencies of two-body collisions between the same species are proportional to $T_g^{0.5}$ [52]. In three-body collisions, although the quantitative estimation of *f* is difficult because the assumption of hard spheres cannot be used, the value of *f* should be also smaller at lower T_g.

2.5.1.3 Density *n*

At T_g near or lower than boiling point, a partial pressure of gas species can be comparable to saturated vapor pressure or saturated sublimation pressure. The values of these saturated pressures depends strongly on T_g as shown in Figure 2.29. When the saturated pressures become lower than the partial pressure of gas species, the partial pressure becomes decreasing according to the saturated pressures. Although the partial pressure of the impurity gas species

sometimes does not become the same value as the saturated pressures in consequence of adsorption, the partial pressure is similar value to the saturated pressures. The effect of T_g on the density of impurity species can be crucial near room temperature, especially for water impurity in atmospheric-pressure plasmas in open air. In addition, the boiling points of the gas species included in air are approximately 195 K (CO_2), 90 K (O_2), 87 K (Ar), and 77 K (N_2). Therefore, it is necessary to discuss the variation of the densities of air impurity species in cryogenic temperatures.

2.5.1.4 Diffusion coefficient *D*

Diffusion coefficient D depends on temperature. In the assumption of the hard sphere gas molecule, the first approximation of interdiffusion coefficient $[D_{12}]_1$ is expressed as [52]

$$[D_{12}]_1 = \frac{3}{2n(\sigma_1 + \sigma_2)^2}\sqrt{\frac{kT_g(m_1 + m_2)}{2\pi m_1 m_2}} \tag{1. 5}$$

where σ_1 and σ_2 are cross sections of species 1 and 2, k is the Boltzmann constant, and m_1 and m_2 are mass of species 1 and 2, respectively. At constant density, $[D_{12}]_1$ can be approximated to be proportional to $T_g^{0.5}$. Similarly, at constant-density conditions, the self-diffusion and interdiffusion coefficients are proportional to $T_g^{0.5}$ in the assumption of variable hard sphere model [53]. The dependencies of the diffusion coefficients of actual gases are similar, for example, D_i for He^m has been estimated to be approximately proportional to $T_g^{0.66}$ below 70 K [48] and D_a in an electron and He^+ system is approximately proportional to $T_g^{0.5}$ [54].

In addition, the ions in plasmas diffuse as an ambipolar diffusion and its coefficient its also dependent on T_g. For example, the slow decay of plasma afterglow due to long ambipolar diffusion lengths [54] and a long relaxation time for the rotational distribution of He_2 molecules [55,56] have been reported. However, in high electric field, drift rather than diffusion is much more important and the drift velocity does not depend on T_g strongly.

However, these studies introduced in this section did not focus on the change in the total plasma reaction system at cryogenic temperatures, but the effects of temperature on the elemental reactions. Therefore, I tried to construct a set of reaction rate constants, whose dependencies on T_g were taken into account, by collecting the data of these previous studies.

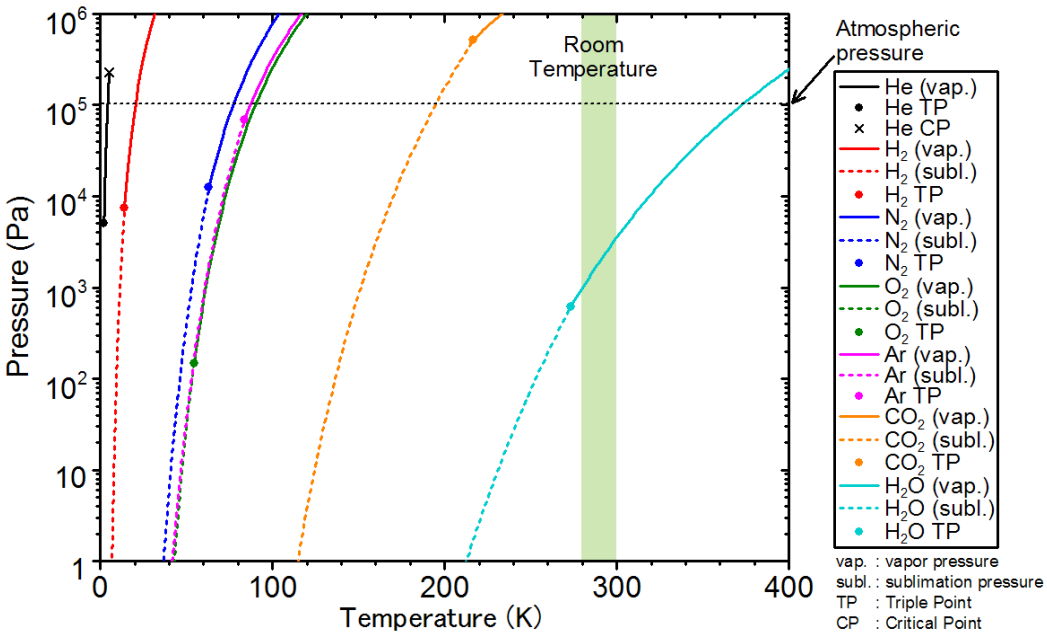

Figure 2.29 Dependency of vapor pressures (vap., solid lines) and sublimation pressures (subl., dashed lines) of various gases on a temperature, and the triple points (TP, circle) and the critical points (CP, cross) of various gases. The data were retrieved from the NIST database of REFPROP [26].

2.5.2 Reaction model

To investigate the effect of T_g on a plasma reaction, it is essential to compare the simulation result using the set of reactions to the experimental result using plasma sources whose T_g can be controlled continuously in the cryogenic range, such as cryoplasmas. For the chemical kinetic calculation of the cryoplasmas, we used a 0-dimensional time-dependent global model. In this calculation, the governing rate equation is expressed as follows:

$$\frac{\mathrm{d}n_i}{\mathrm{d}t} = \sum_j S_{ij\mathrm{R}} - \sum_j L_{ij\mathrm{R}} - L_{i\mathrm{W}} \tag{2. 19}$$

where t is the time, n_i the number density of the ith species, $S_{ij\mathrm{R}}$ the reaction rate R generating the ith species, $L_{ij\mathrm{R}}$ the reaction rate R resulting in the loss of the ith species, and $L_{i\mathrm{W}}$ the loss rate of the ith species by the interdiffusion of neutral species or the ambipolar diffusion and drift of ions.

We considered a He/N_2/O_2/H_2O system including the 21 reactions in Table 2.8 and the 14 species in Table 2.9. The reaction rate constants are also given in Table 2.8 [41,43,45,47,57–66] and their dependency on T_g is discussed in the following paragraphs. The interdiffusion coefficients (D_i), ambipolar diffusion coefficients (D_a), and mobilities (μ) of each species are presented in Table 2.9 [48,49,54,58,67–72]. The reaction pathways for He/N_2 system considered in this study are expressed in Figure 2.30. For O_2 and H_2O, only the Penning ionization reactions with He were included in this model. The studies for plasma chemistry including He, N_2, O_2, and, H_2O have been reported for various plasmas,

such as interstellar plasmas [73–75] and atmospheric pressure microplasmas [65,76–80].

Whether or not the reaction is electron-related has an important effect on the dependencies of some reaction rates on T_g, and the dependencies were estimated by applying the following concepts. First, if it is an electron-related reaction, the reaction rate constant is generally not strongly dependent on T_g, with a few exceptions, for example, k_R of R11 (k_{R11}) in Table 2.8. Second, the reactions not involving electrons are strongly affected by T_g. For two-body collisions, when we assume that the collision cross sections are independent of T_g, the reaction rate constants are proportional to $T_g^{0.5}$ owing to the variation of the collision frequency [23]. This assumption is sometimes valid for small temperature variations near room temperature. Although it might not be valid for the present study because T_g in cryoplasmas changes dynamically to values less than room temperature, we adopted this assumption for some reactions. Third, it has been suggested that k_R of ion-molecule collisions are independent of T_g below 1000 K, owing to the polarization of molecules [81], with some exceptions such as the reaction $O^+ + N_2 \rightarrow NO^+ + N$ [42]. Fourth, concerning three-body reactions, particularly reactions between two atoms and an atomic ion such as R7, $k_R \propto T_g^{-3/4}$ has been reported [59]. Fifth, if there are several alternatives of species generated by the reaction, the generated species possessing a higher molecular weight (MW) is adopted, while the species of lower MW is neglected, because association should tend to occur at lower temperatures. For example, the formation of $He^+ + He + e$ can also occur by the mutual collision of He^m (R4 in Table 2.8). However, we adopted $He_2^+ + e$ for the right branch of R4 for cryogenic temperatures, because it has been reported that the lower the collision energy, the higher the ratio of He_2^+ generation [82]. Specifically, the probability for the formation of H_2^+ is ~59% at a collision energy of 0.052 eV, which corresponds to the energy near room temperature, and ~92% at a collision energy of 0.01 eV [82].

For the specific reaction rate constants in Table 2.8, the reaction rate constants of R1, R2, and R10 were calculated by the Boltzmann equation solver BOLSIG+ [83] using cross section databases [84–86]. For R3 – R7 , R9, and R11 – R13, we used the rate constants in Table 2.8, which were measured or estimated in previous studies [41,45–47,58,76]. For R8, since we could not find any previous reports, we assumed that the reaction constant of R8 was the same as that of R7. Note that the density ratio of $[He_2^+] / [He_3^+]$ in the equilibrium state decreases with decreasing T_g, and it has been estimated to be less than 10^{-5} at $T_g < 100$ K [69,87]. Regarding the ion-molecule collisions in R14, R16, R18, and R19, we assumed that the rate constants were independent of T_g, as mentioned above [81]. As we could only find the reaction constants at room temperature for R15, R17, R20, and R21, we assumed that the rate constants were proportional to $T_g^{1/2}$ for these reactions by only considering the dependency of collision frequency on T_g.

We note that this model does not include all possible reactions in a $He/N_2/O_2/H_2O$ system. Among the reactions which are often taken into account in plasma chemistry calculations at room temperature, we assumed that reactions not included in Table 2.8, such as $He^m + He_2^m \rightarrow H_2^+ + He + e$ and $He_2^+ + e \rightarrow He^m + He$, were negligible. It has been reported that the former reaction does not affect He_2^m decay process at 4.2 K [58], and this implies that the reaction is not dominant at cryogenic temperatures. The latter reaction needs He_2^+ to be vibrationally excited, but it was reported that the He_2^+ vibrational relaxation rate need to be sufficiently high [88,89]. We also neglected dielectronic recombination reactions which have often been investigated in interstellar plasmas [90,91] and fusion plasmas [92],

because it has been reported that the dielectronic recombination to helium is important at high temperature (e.g. ~ 8×10^4 K [93]), where most of the helium is doubly ionized [93,94]. In addition, this model might be invalid at $T_g > 100$ K because of the adopted assumptions mentioned above. However, although the model should be further improved for being a general reaction model for cryoplasma chemistry, as will be shown, it is sufficient for the qualitative discussion in section 2.6.

For the component of L_{iW}, the diffusion and the drift were considered. The diffusion loss of the jth species (number density: n_j) to the electrode in a unit time was assumed to be $D_i \times n_j / d^2$, where d is the gap distance. The formula can be calculated under the assumption that the density profile along a line perpendicular to the electrode between electrodes can be expressed as $n(z) = n_i \times (1 - 4 \times z^2 / d)$ where z is the position along the line and $z = 0$ is at the center of the electrodes. The loss of ions by drift in a unit time was estimated to be $n_j \times \mu \times U / d^2$. The formula can be introduced in the assumption of the homogeneous electric field in the electrode gap ($E = U / d$).

The dependence of D_i and D_a on T_g are included in this model as indicated in Table 2.9. For example, D_i for He^m has been estimated to be approximately proportional to $T_g^{0.66}$ below 70 K [48] and D_a in an electron and He^+ system is approximately proportional to $T_g^{0.5}$ [54]. The values of D_a for the other ions are assumed to be comparable to D_a in the electron and He^+ system. Concerning the mobility (μ), although μ depends on the reduced electric field (E/N) and the "effective temperature" (T_{eff}) [70], the dependences are not strong under the conditions of this study. For example, μ for N_2^+ in He is almost constant when $E/N < 20$ Td ($= 10^{-21}$ V m^2) and $T_{eff} < 150$ K [70] and μ for He^+ in He is within the range of 20 ± 3 cm^2 V^{-1} s^{-1} below 80 K [67,68]. Therefore, μ can be assumed to be independent of both T_g and E/N and v_D can be assumed to be independent of T_g and dependent on E/N.

Table 2.8 Reactions and their rate constants used for numerical calculation. The reactions from R1 to R9 are for He gas, those from R10 to R19 are for the mixture of He/N_2, and those of R20 and R21 are typical quench reactions of He^m caused by O_2 and H_2O.

Index	Reaction	Rate constant [a]	Reference
R1	$He + e \rightarrow He^m + e$	$f(T_e)$	-[d]
R2	$He + e \rightarrow He^+ + 2e$	$f(T_e)$	-[d]
R3	$He^m + e \rightarrow He^+ + 2e$	$4.66 \times 10^{-10} \times T_e^{0.6} \times \exp(-5.55 \times 10^4 / T_e)$	[57]
R4	$2He^m \rightarrow He_2^+ + e$	$1.1 \times 10^{-9} \times (T_g/10)^{0.167}$	[47]
R5	$2He_2^m \rightarrow He_2^+ + 2He + e$	5×10^{-10}	[58]
R6	$He^m + 2He \rightarrow He_2^m + He$	$8.7 \times 10^{-36} \times T_g \times \exp(-750 / T_g)$ $+ 0.41 \times 10^{-36} \times T_g \times \exp(-200 / T_g)$	[41]
R7	$He^+ + 2He \rightarrow He_2^+ + He$	$1.4 \times 10^{-31} \times (T_g / 76)^{-0.75}$	[43,59]
R8	$He_2^+ + 2He \rightarrow He_3^+ + He$	$1.4 \times 10^{-31} \times (T_g / 76)^{-0.75}$	-[c]
R9	$He_3^+ + e \rightarrow He_2^m + He$	$4 \times 10^{-5} \times (T_e / 10)^{-1}$	[45]
R10	$N_2 + e \rightarrow N_2^+ + 2e$	$f(T_e)$	-[d]
R11	$N_2^+ + e \rightarrow N_2$	$7.6 \times 10^{-7} \times (T_e / T_g)^{-0.5}$	[60,61]
R12	$N_2^+ + N_2 + He \rightarrow N_4^+ + He$	$5 \times 10^{-29} \times (T_g / 300)^{-1}$	[62]
R13	$N_4^+ + e \rightarrow 2N_2$	$2 \times 10^{-6} \times (T_e / T_g)^{-0.5}$	[61]
R14	$N_4^+ + He^m \rightarrow He + N_2 + N_2^+$	1×10^{-10}	[63][b]
R15	$N_2 + He^m \rightarrow N_2^+ + He + e$	$5 \times 10^{-11} \times (T_g / 300)^{0.5}$	[60][b]
R16	$N_2 + He^+ \rightarrow N_2^+ + He$	6×10^{-10}	[62][b]
R17	$N_2 + He_2^m \rightarrow N_2^+ + 2He + e$	$3 \times 10^{-11} \times (T_g / 300)^{0.5}$	[64][b]
R18	$N_2 + He_2^+ \rightarrow N_2^+ + He_2^m$	1.4×10^{-9}	[60,65][b]
R19	$N_2 + He_2^+ \rightarrow N_2^+ + 2He$	1.2×10^{-9}	[62][b]
R20	$He^m + O_2 \rightarrow He + O_2^+ + e$	$2.6\times10^{-10} \times (T_g / 300)^{0.5}$	[66]
R21	$He^m + H_2O \rightarrow He + H_2O^+ + e$	$1\times10^{-10} \times (T_g / 300)^{0.5}$	[63]

a: [unit] R6–8,12: $cm^6\ s^{-1}$, other:$cm^3\ s^{-1}$
b: Estimated the dependency of the rate constant on T_g.
c: Assumed to be comparable to R8.
d: Calculated by BOLSIG+.

Table 2.9 Interdiffusion coefficients (D_i) for the neutral species and the ambipolar diffusion coefficients (D_a) and mobilities (μ) for the charged species.

	Species	D_i or D_a ($cm^2\ s^{-1}$)	Ref.	μ ($cm^2\ V^{-1}\ s^{-1}$)	Ref.
1	e	$0.0209 \times T_g^{0.5}$	[54]	–	
2	He	–	[a]	–	
3	He^m	$6.91 \times 10^{-3} \times T_g^{0.66}$	[48]	–	
4	He_2^m	$2.3 \times 10^{-3} \times T_g^{0.66}$	[58][b]	–	
5	He^+	$0.0209 \times T_g^{0.5}$	[54]	20.0 [d]	[67,68]
6	He_2^+	$0.0209 \times T_g^{0.5}$	[c]	16.0	[69]
7	He_3^+	$0.0209 \times T_g^{0.5}$	[c]	19.2	[69]
8	N_2	–		–	
9	N_2^+	$0.0209 \times T_g^{0.5}$	[c]	16.3	[70]
10	N_4^+	$0.0209 \times T_g^{0.5}$	[c]	16.3	[e]
11	O_2	–	[f]	–	[f]
12	O_2^+	–	[f]	–	[f]
13	H_2O	–	[f]	–	[f]
14	H_2O^+	–	[f]	–	[f]

a: Since He and N_2 were treated as background species because of their large density, the diffusion coefficients of He and N_2 are not indicated.
b: D_i of He_2^m [49,71,72] is approximately one-third of that of He^m [48] at 300 K. Since it has been reported that D_i of He_2^m is comparable to that of He^m [58], we assumed that D_i of He_2^m [49,71,72] is also one-third of that of He^m at cryogenic temperatures.
c: Assumed to be comparable to D_a in e and He^+ system.
d: μ of He^+ in He was reported within $20 \pm 3\ cm^2\ V^{-1}\ s^{-1}$ below 80 K in Ref [67,68].
e: Assumed to be comparable to μ of N_2^+.
f: Diffusion and drift of O_2, O_2^+, H_2O, and H_2O^+ was not included in the simulation in this study.

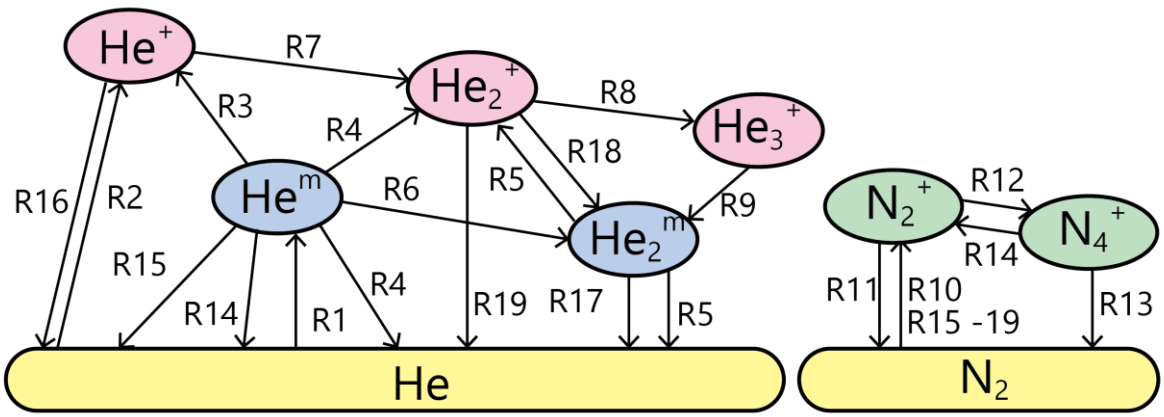

Figure 2.30 Diagram of reaction pathways considered in this study for the system for He/N_2 species. The numbers started from R, e.g. R1, indicates reaction number 1 in Table 2.8.

2.5.3 Electron temperature and density

For the calculation of reaction rate constants and equation (2. 19), the values of electron density n_e and electron temperature T_e are necessary. In this study, these values were estimated by a method based on employing the U and I values measured at each temperature [7]. The Einstein equation was used to estimate T_e,

$$\frac{D_e}{\mu_e} = \frac{k_B T_e}{e} \tag{2. 20}$$

where D_e is the electron free diffusion, μ_e is the electron mobility, k_B is the Boltzmann constant, and e is the elementary electron charge. The following equation was used to estimate N_e:

$$N_e = \frac{j}{eW} \tag{2. 21}$$

where j is the current density and W is the electron drift velocity. The electron swarm parameters were estimated using BOLSIG+ [83] and the cross section database [84–86]. The above estimation method was described in more detail in Ref. [95]. The estimation method involves a few assumptions such as the Boltzmann distribution of electron energy, an isotropic plasma distribution, and a quasi-static electric field. Although we did not evaluate the uncertainty of the method strictly owing to the difficulty of estimating the uncertainties of the involved parameters, the obtained values may be valid to one significant figure.

The estimated average values were 1 – 10 eV for T_e and 10^8 – 10^{10} cm^{-3} for N_e for Metal-2 electrodes. Therefore, the cryoplasmas in this study had a low ionization degree (~10^{-10}). Also, the temporal variations of T_e and N_e could be estimated from Figure 2.6. We used the values of N_e and T_e in the calculation of the cryoplasma chemistry in section 2.6.

2.6 Discussions on T_g dependency of plasma chemistry

2.6.1 Discussions on results of OES

Here we discuss the reaction dynamics in the cryoplasmas on the basis of the experimental results given in section 2.3.2. To understand the results of time-resolved OES in section 2.3.2, such as the longer duration of the discharge current with respect to the helium optical emission, and the delay in N_2^+ emission, we conducted a reaction dynamics calculation of the cryoplasmas using a time-dependent global (0-dimensional) model that included temperature-dependent reaction rate constants, which was introduced in section 2.5. One central aspect of the calculation was that we took into account the effect of T_g on the plasma chemistry and the transportation of species.

In the calculation, the plasma gas temperatures were kept constant at T_g = 28 K in section 2.6.1.1 and T_g = 54 K in section 2.6.1.2. We used the temporal variations of N_e and T_e calculated from the experimental results given in section 2.5.3. The initial densities in the calculation in section 2.6.1.1 were 4.8×10^{19} cm^{-3} for He and 0 cm^{-3} for the other species, and those in section 2.6.1.2 were 4.8×10^{19} cm^{-3} for He, 1.2×10^{16} cm^{-3} for N_2, and 0 cm^{-3} for the other species. The density of each species was almost constant after 10 voltage cycles and the calculation results given in sections 2.6.1.1 and 2.6.1.2 represent the steady-state values. The reaction numbers in this section, such as R1, correspond to those listed in Table 2.8.

2.6.1.1 Longer duration of current in comparison to optical emission (condition 2A)

The calculated reaction rates R of direct ionization of R2 (R_{R2}) and stepwise ionization of R3 (R_{R3}), and the sum of R_{R2} and R_{R3} in pure He in a steady-state situation are shown in Figure 2.31(a). In this section, since we discuss the waveform of the discharge current, we focused on the ionization reactions. The vertical dashed lines and dotted lines in Figure 2.31(a) indicate the times of zero voltage and maximum current, respectively. While the time of peak of R_{R2} approximately corresponds to that of the voltage peak and current peak, the peak of R_{R3} was delayed relative to the current peak. After R_{R3} reached its maximum, it suddenly dropped to almost zero when U reached zero. The shape of the line showing the sum of R_{R2} and R_{R3} was similar to that of the current waveform in Figure 2.6(a). From this calculation, we could assume that the long duration of discharge current was mainly caused by electron generation via the stepwise ionization of R3.

The reason why R3 was delayed with respect to R2 is discussed below. The reaction species colliding with electrons in R2 and R3 are He and He^m, respectively. While both the He^m and electron densities should change with time, the He density temporally changes very little due to its high density. Therefore, R_{R2} mainly depends on the electron density, while R_{R3} depends on both the electron and He^m densities. He^m was mainly generated by R1, and the R of R1 (R_{R1}), which represents approximately the generation rate of He^m, reached a maximum near the current and voltage maxima. However, the He^m density increased and showed a maximum after the maxima of the current and voltage, because the lifetime of He^m was longer, in other words, the decay of He^m was slower at cryogenic temperatures,

mainly owing to the strong dependency of the three-body He^m-quench reaction (R6) on T_g [38,58,71]. Thus, the long lifetime of He^m causes the phenomenon of the long duration of the discharge current.

Figure 2.31(b) shows the calculation results of the delay time of the R_{R3} peak to R_{R2} peak at each T_g from 5 to 300 K. We note that the model might show some shift at higher temperatures, particularly for $T_g > 100$ K, due to the assumptions we used in the model. The data indicates that the delay time (of about 8 μs) is independent from T_g below 150 K and R_{R3} peak shifts to smaller delays with increasing T_g at $T_g > 150$ K, down to approximately 3 μs at 300 K. These calculation results imply that, in a pure He system, the lifetime of He^m is not affected by T_g below 150 K, while the effect of T_g on the lifetime of He^m becomes significant above $T_g > 150$ K. The results also suggest that the quench mechanism of He^m may vary with T_g and that the transition of the quench reactions may occur around 150 K.

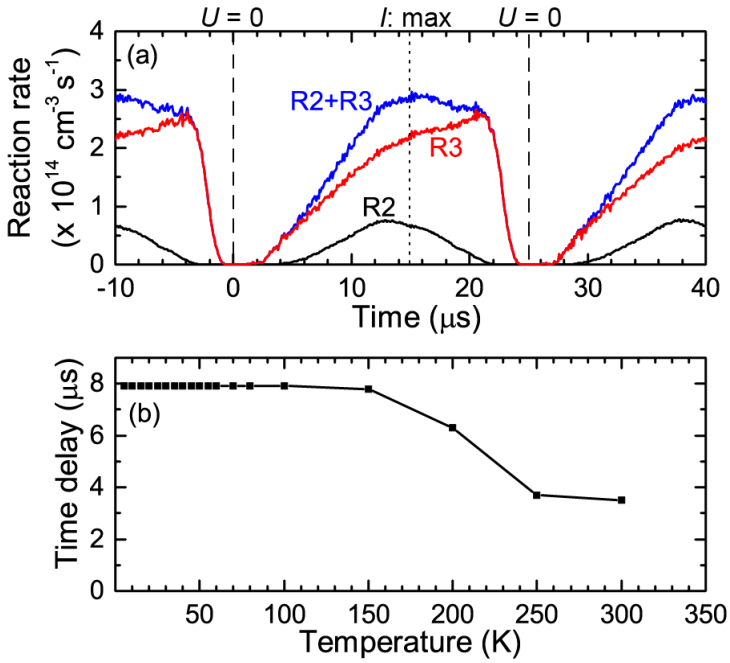

Figure 2.31 Simulation results of cryoplasma reactions at T_g = 28 K in a pure He system. (a) displays the reaction rates of R2 (direct ionization), R3 (stepwise ionization), and R2 + R3 in Table 2.8. The vertical dashed and dotted lines indicate the times of zero voltage and the maximum discharge current, respectively. (b) shows the dependency of the delay time of the reaction rate peak of R3 relative to that of R2 on T_g.

2.6.1.2 Time delay between emission peaks of N_2^+ and He lines (condition 2B)

We observed a delay of the N_2^+ emission relative to the He emission as mentioned in section 2.3.2. The calculation results for the He/N_2 system at condition 2B are shown in Figure 2.32(a). The R_{R1} is indicated as the solid black line, and R of N_2 Penning ionization of R15 (R_{R15}) is shown by the red line. The first negative system of the N_2^+ emissions was basically generated by Penning ionization in the He/N_2 system, rather than by direct ionization from the ground

state by electron collision [96]. While the timing of the peak of R_{R1} was similar to that of the measured He emission, there was a delay in R_{R15} relative to R_{R1}. Although the delay time of the calculated R was shorter than that of the measured time-resolved emission intensities (8 μs vs 4 μs), the delay was successfully reproduced by the plasma chemistry calculation including the effect of T_g.

Figure 2.32(b) shows the delay time of R15 to R1 at each T_g from T_g = 40 K to 300 K. In this calculation, the N_2 ratio was fixed at 2.4×10^{-4}, i.e., the initial density of He and N_2 were set at 4.8×10^{19} cm^{-3} and 1.2×10^{16} cm^{-3}, respectively. Since it was not possible to attain a N_2 ratio of 2.4×10^{-4} in the experiments below T_g = 40 K because of a low sublimation pressure, the calculations were limited to conditions of 40 K and above. The reason why the calculation results do not lie on a smooth line is that electric noise in the measurement results for the discharge current affected the calculations. From the calculations, we found that the delay time gradually decreased from about 4 μs at T_g = 40 K to 0.8 μs at 300 K and, in contrast to a pure He system, there was no plateau below 150 K in the calculation results. This monotonic decrease of the delay time with increasing T_g was similar to what was reported by Choi *et al.* (Figure 1.13) [6]. These results suggest that the present global model can reproduce the experimental results including those of the previous study [6]. On the other hand, we could not reproduce the two time-dependent phenomena discussed in sections 2.6.1.1 and 2.6.1.2 by the reaction models of the previous works [65,76], which are for atmospheric pressure plasmas at room temperature. This result indicates that a reaction model including the term of T_g is necessary for the discussion of plasmas in several temperature ranges (almost all reaction models for atmospheric pressure plasmas are only for around room temperature) and for the discussion of phenomena changing with T_g.

Regarding the cause of the delay phenomenon, it is also thought to be due to the long lifetime of He^m, owing to the slow quenching rate of R6 and R15 at cryogenic temperatures. In a He/N_2 system, the Penning ionization (R15) is important for He^m-quenching reaction, in addition to the He^m-quenching reaction in a pure He system such as R4 and R6. At lower temperatures in Figure 2.32(b) such as those corresponding to 40 K, R15 should be dominant, because of a reaction rate constantly higher than that of R4, and the strong dependency of R6 on T_g. With increasing T_g, R_{R15} should increase because of the collision frequency and also R_{R6} should increase rapidly, so that the quenching rate of He^m should be higher. Therefore, the lifetime of He^m should be shorter with increasing T_g and this should be attributed to the dependency of the delay time of R_{R15} to R_{R1} on T_g in Figure 2.32(b) and the previous study [6]. Moreover, the difference of the dependency of the delay time on T_g in Figure 2.31(b) and Figure 2.32(b) were mainly caused by the difference of the dependency of R_{R6} and R_{R15} on T_g. The dependency of the lifetime of He^m and the elemental reactions are discussed in sections 2.6.2 and 2.6.3.

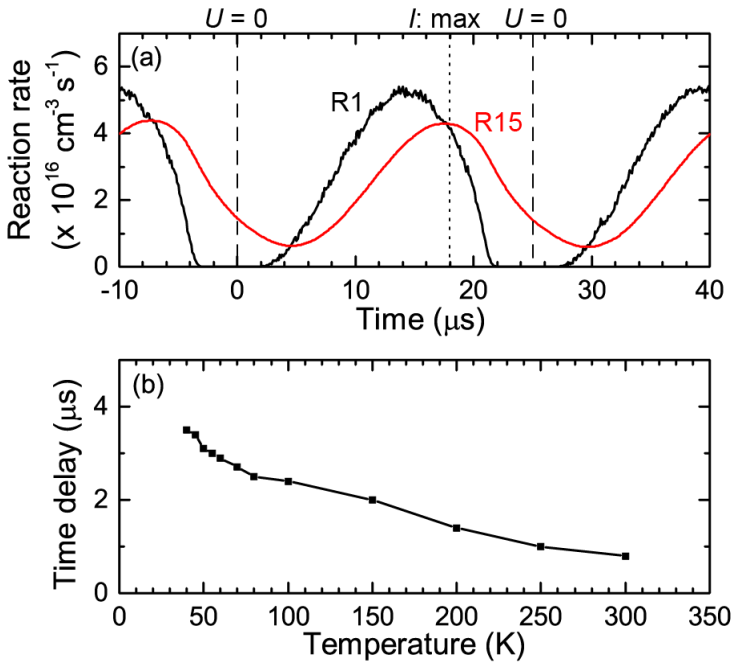

Figure 2.32 Simulation results of cryoplasma reactions at T_g = 54 K in He/N_2 system. (a) displays the reaction rates of R1 and R15 in Table 2.8. The vertical dashed lines indicate the times of zero voltage and the maximum discharge current. (b) indicates the variation of the delay time of the reaction rate peak of R15 relative to that of R1 above 40 K.

2.6.2 Discussion on results of LAS

2.6.2.1 Lifetime of He^m

Here, we discuss the quench reaction processes of He^m atoms generated in the DBD cryoplasma in order to reveal the main quenchers of He^m atoms and their variation for each condition of T_d. We consider the gases of He, N_2, O_2, and water vapor (H_2O), taking into account the following five reactions related to He^m quenching shown in Table 2.10.

The listed reactions are representative of He^m quench processes; however, it should be noted that the actual reaction system in the discharge in He with air impurities is more complex than the listed reactions, as suggested in the literature, for instance [76,97], and the dependences of the reaction rate coefficients on the gas temperature have not been revealed sufficiently, even in the He/N_2 gas mixture reaction system. Therefore, to fully understand the reaction system of He with air impurities of N_2, O_2 and H_2O and its variation due to the change of gas temperature, further fundamental studies on each reaction are still needed. In the discussion part that follows, since the He^m quenching processes in the afterglow phase when the gas temperature was cooled down from T_g are discussed, it is assumed that T_g was equal to T_d in the discussion.

Table 2.10 Reactions and their rate constants used for numerical calculation discussed in section 2.6.2. The indexes and rate constants of reactions are identical to those in Table 2.8.

Index	Reaction	Rate constant [a]	Reference
[Self-quenching reaction between two He^m atoms]			
R4	$2He^m \rightarrow He_2^+ + e$	$1.1 \times 10^{-9} \times (T_g/10)^{0.167}$	[47]
[Three-body reaction with ambient He atoms]			
R6	$He^m + 2He \rightarrow He_2^m + He$	$8.7 \times 10^{-36} \times T_g \times \exp(-750 / T_g)$ $+0.41 \times 10^{-36} \times T_g \times \exp(-200 / T_g)$	[41]
[Penning reactions with impurity species]			
R15	$He^m + N_2 \rightarrow He + N_2^+ + e$	$5 \times 10^{-11} \times (T_g / 300)^{0.5}$	[60][b]
R20	$He^m + O_2 \rightarrow He + O_2^+ + e$	$2.6\times10^{-10} \times (T_g / 300)^{0.5}$	[66]
R21	$He^m + H_2O \rightarrow He + H_2O^+ + e$	$1\times10^{-10} \times (T_g / 300)^{0.5}$	[63]

a: [unit] R6: $cm^6\ s^{-1}$, other:$cm^3\ s^{-1}$
b: Estimated the dependency of the rate constant on T_g.

For the first step of the discussion, we analyze the dry air (N_2 and O_2) impurity ratio from the measured decay curve at T_d = 100 K. At this temperature, we can ignore the effect of the H_2O vapor (R21) on He^m quenching, since the H_2O is in its solid state. From the comparison between the calculated He^m quench rate considering R6, R15, and R20, changing the dry air impurity ratio and the measured He^m quench speed at T_d = 100 K, the dry air impurity ratio in the experiment, where the N_2 : O_2 ratio is fixed at 4 : 1, could be estimated at 120ppm (0.012%). The comparison can be seen in Figure 2.33(a). The relative contributions of the quenchers (quench reactions) are approximately He(R6) : N_2(R15) : O_2(R20) = 1 : 19 : 25 in this condition; therefore, we can conclude that the He^m quenchers are N_2 and O_2 at T_d = 100 K. Since the reaction rate of self-quenching process (R4, $k_{R4}[He^m]^2 \sim 6 \times 10^{13}\ cm^{-3}\ s^{-1}$ where $[He^m] = 2.0 \times 10^{11}\ cm^{-3}$) is 10 times smaller than that of R6 ($k_{R6}[He^m][He]^2 \sim 7 \times 10^{14}\ cm^{-3}\ s^{-1}$ where $[He^m] = 2.0\times10^{11}\ cm^{-3}$ and $[He] = 2.4\times10^{19}\ cm^{-3}$), we ignored R4 in the discussion on the measurement result at T_d = 100 K.

Then, we estimated the H_2O impurity ratio present in the discharge at T_d = 300 K assuming that the dry air (N_2 and O_2) impurity ratio is 120 ppm, the same as that at T_d = 100 K. Figure 2.33(b) shows the comparison between the calculated He^m quench rate changing the H_2O vapor ratio and the measured He^m quench speed at T_d = 300 K. From the calculations, the H_2O vapor included in the discharge region was approximately 550ppm for this temperature. The reason why the H_2O ratio was larger than the dry air impurity ratio is probably due to our experimental procedure. Since increasing T_d takes much less time than decreasing T_d from RT to ~10 K, the LAS experiments were realized with increasing T_d from 14, 100 to 300 K. Therefore, H_2O that is initially present and gets into the system with air impurities is sticking to the inner wall of the tubing during the low T_d experiments, then it turns into vapor and diffuses into the discharge region in the experiment at T_d = 300 K. The relative contributions of the He^m quenchers (quench

reactions) are approximately He(R6) : N_2(R15) : O_2(R20) : H_2O(R21) = 4 : 3 : 4 : 44 at T_d = 300 K. It should be noted that, when T_d is increased to near RT from 100 K, desorption of some impurity molecules, for example carbon dioxide, occurs; however, we considered only H_2O, which was probably the major quencher in the investigated temperature range, and not the other species in this study. Therefore, the H_2O contribution shown above includes contributions of all other molecules except for N_2 and O_2.

Finally, for T_d = 14 K, since neither air nor H_2O impurities are present and the reaction rate of R6 ($k_{R6}[He^m][He]^2 \sim 5 \times 10^9$ cm^{-3} s^{-1} where $[He^m] = 2.5 \times 10^{12}$ cm^{-3} and $[He] = 2.4 \times 10^{19}$ cm^{-3}) becomes much smaller than that of R4 ($k_{R4}[He^m]^2 \sim 7 \times 10^{15}$ cm^{-3} s^{-1} where $[He^m] = 2.5 \times 10^{12}$ cm^{-3}), the He^m quenching process is governed by the self-quenching reaction (R4). This can be confirmed by looking at the measured decay curve, which was not linear on a semi-logarithmic plot as shown in Figure 2.24(b), since this self-quenching process is a second-order reaction.

From the discussion, we could reach the conclusion that the major quenchers of the He^m atoms in the DBD cryoplasma at each T_d condition were mainly H_2O and relatively small contribution of He, N_2, and O_2 for T_d = 300 K, N_2 and O_2 for T_d = 100 K, and finally He^m itself for T_d = 14 K, respectively. The quench reactions of He^m were discussed in more detail in section 2.6.3.2.

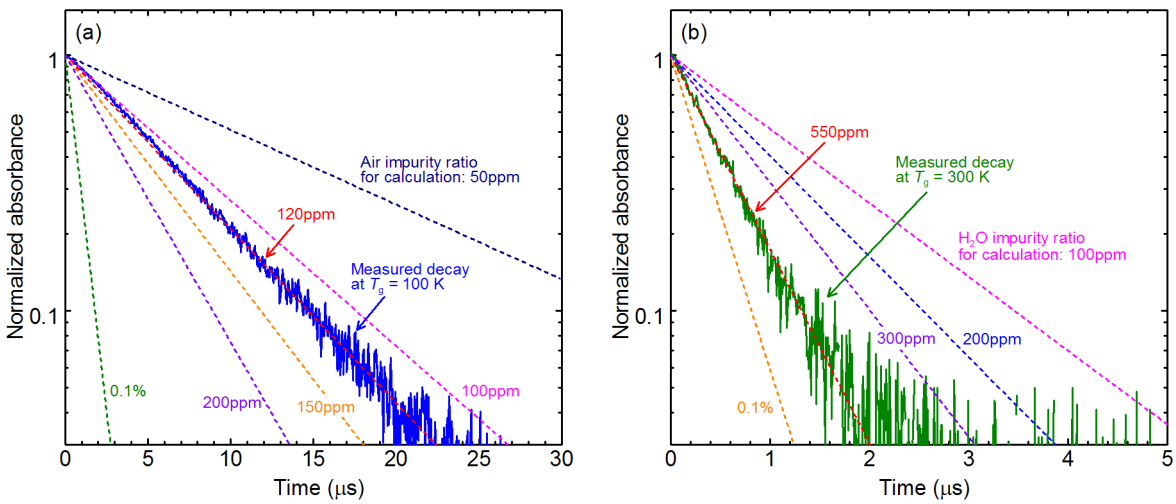

Figure 2.33 (a) Temporal evolution of normalized absorbance in the afterglow of He^m atoms measured at T_d = 100 K, with the simulated decay curves calculated considering R6, R15, and R20 including certain amounts of dry air impurities (N_2 and O_2 with a fixed ratio of 4:1) for evaluating the air impurity ratio at T_d = 100 K. (b) Temporal evolution of normalized absorbance in the afterglow of He^m atoms measured at T_d = 300 K, with the simulated decay curves calculated considering R6, R15, R20, and R21, including a fixed amount of dry air impurity of 120ppm and varying levels of H_2O vapor impurity (100ppm to 0.1%) for evaluating the H_2O impurity ratio at T_d = 300 K.

2.6.2.2 Density and waveform of He^m

The density of He^m (n_m) was simulated using the reaction model with the elemental reactions of R1 – R21 at the conditions listed in Table 2.11. The evaluated T_g by thermal simulation were used and the number densities of the impurity species were estimated in section 2.6.2.1. The values of T_e and n_e were estimated by U and I waveforms indicated in Figure 2.25. The simulation results are presented in Figure 2.34 with the measured values indicated in Figure 2.25. From the initial n_m of 0, n_m were accumulated and became stable after several cycles of an applied voltage. The temporal evolution of n_m was not perfect, but the approximate waveform of n_m was reproduced. In addition, the simulation results of average n_m for a period of the voltage cycle was 7.1×10^{11} cm^{-3} (condition 3A), 1.6×10^{10} cm^{-3} (condition 3B), and 6.3×10^{8} cm^{-3} (condition 3C). On the other hand, the average n_m estimated by LAS were 1.2×10^{12} cm^{-3} (condition 3A), 5.1×10^{10} cm^{-3} (condition 3B), and 2.2×10^{9} cm^{-3} (condition 3C). The average values estimated from the simulation were lower than the measured values, but the estimated values existed between the measured values and a half of them. Therefore, I concluded that they were well reproduced, although these values did not perfectly correspond each other.

Thus, not only the quench reactions, but also the total reactions in cryoplasmas could be reproduced for wide T_g range, at least qualitatively, by the reaction model developed in this study.

Table 2.11 Conditions for the simulation of the plasma chemistry for DBD electrodes.

		Condition 3A	*Condition 3B*	*Condition 3C*
Plasma gas temperature [a]	T_g	31 K	111 K	305 K
Pressure	P	4.7 kPa	33 kPa	100 kPa
[Number density]				
He	n_{He}	2.4×10^{19} cm^{-3}	2.4×10^{19} cm^{-3}	2.4×10^{19} cm^{-3}
N_2	n_{N2}	0	2.3×10^{15} cm^{-3} (96ppm)	2.3×10^{15} cm^{-3} (96ppm)
O_2	n_{O2}	0	5.8×10^{14} cm^{-3} (24ppm)	5.8×10^{14} cm^{-3} (24ppm)
H_2O	n_{H2O}	0	0	1.3×10^{16} cm^{-3} (550ppm)

a: T_g was estimated by thermal simulation.

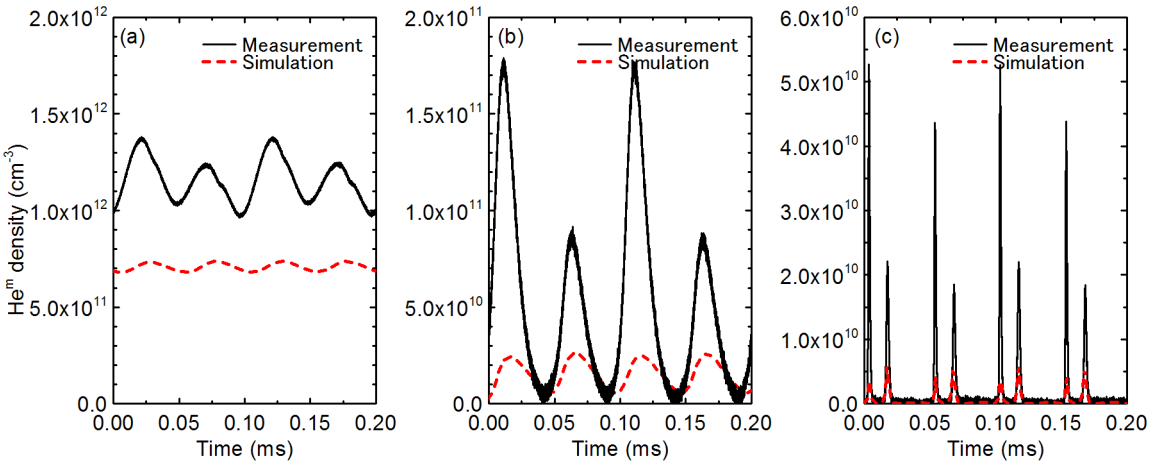

Figure 2.34 Values of the density of metastable He (nm) estimated by LAS measurement and reaction simulation (a) in condition 3A (T_d = 14 K), (b) in condition 3B (T_d = 100 K), and (c) in condition 3C (T_d = 300 K),

2.6.3 Dependency of plasma chemistry on T_g

In this section, the reactions in cryoplasmas are discussed to clarify the dependency of plasma chemistry on T_g using the reaction simulation developed in this study, not only for explaining the experimental results. At first, the whole reaction balance in He/N_2 system was discussed based on the calculation results of the reaction model proposed in this study. Then, the variation of the quench reactions of He^m in He with impurity species of N_2, O_2, and H_2O was discussed.

2.6.3.1 Dependency of plasma chemistry in He with 100ppm of N_2 on T_g

Here, as a typical condition, the variation of plasma chemistry depending on T_g in He with 100ppm (0.01%) of N_2 at constant density of $n_{He} = 2.4 \times 10^{19}$ cm^{-3} was discussed. In the discussion in this section, Penning ionization of O_2 (R20) and H_2O (R21) in Table 2.10 were not taken into account. Figure 2.35 presents the magnitudes of reaction rates R of the elemental reactions at T_g = 300, 40, 5 K on the schematic of reaction paths of Figure 2.30. The reactions with red arrows and characters ($R \geq 10^9$ cm^{-3} μs^{-1}) are the dominant reactions, those with blue (10^6 cm^{-3} μs^{-1} $\leq R < 10^9$ cm^{-3} μs^{-1}) are the effective but not the dominant reactions, and those with black ($R < 10^6$ cm^{-3} μs^{-1}) are scarcely effective to the whole reaction dynamics.

At T_g = 300 K, as shown in Figure 2.35(a), the main reactions were the generation reaction of He^m by electron impact (R1), the quench reactions of He^m to ground state by Penning ionization with N_2 (R15) and to He_2^m by three-body reaction with He atoms (R6), and the quench reaction of He_2^m to ground state by another Penning ionization with N_2 (R17). On the other hand, the direct ionization reaction of He (R2) was not dominant and two-step ionization (R3)

rarely occurred because of the short lifetime of He^m due to high quench rate by other reactions such as R6 and R15. Therefore, electrons were supplied mainly by the Penning reactions of R15 and R17. The generated He^+ was quenched to He_2^+ gradually by attachment reactions of R7 and then to He_3^+ by R8, and the ions were dissipated by drift diffusion. Similarly, N_2^+ mainly generated by Penning reactions was quenched to N_4^+ by attachment reaction of R12 and the ions were dissipated by drift diffusion.

With decreasing T_g, R_{R6} drastically decreased due to the strong dependency of k_{R6} on T_g as shown in Figure 2.28(a), the balance of quench reactions of He^m varied. As a result, at T_d = 40 K, the dominant reactions were only R1, R15, and R12 [Figure 2.35(b)]. Meanwhile, R of two-step ionization reaction to He^+ (R3) and self-quenching reaction generating He_2^+ and He (R4) were larger than those at T_d = 300 K. The reactions related to N_2 did not show large variation from T_d = 300 to 40 K because the reaction rate constants of the reactions related to N_2 does not depend on T_g drastically.

At lower T_g than 40K, the density of N_2 decreased drastically owing to the drastic variation of sublimation pressure of N_2 as shown in Figure 2.35(c). The all reactions related to N_2 (R10-R19) were almost zero and, therefore, the arrows of the reactions were not shown in Figure 2.35(c). As a result of the decrease in R_{R6} and R_{R15}, the lifetime and the density of He^m increased, as discussed in section 2.4. Consequently, the collision frequency between He^m increased and R4 became dominant. Thus, the reaction dynamics varied with T_g drastically.

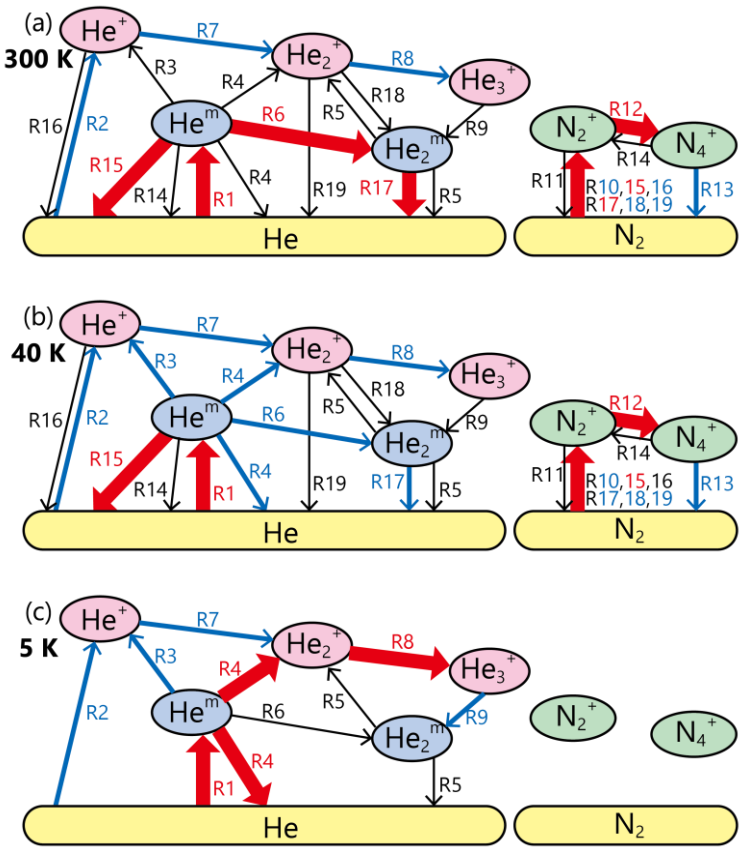

Figure 2.35 Magnitude of a reaction rate (R) of each reaction in He/N_2 system at (a) T_g = 300 K, (b) T_g = 40 K, and (c) T_g = 5 K. The magnitude of R is indicated as the color an dthickness of the arrow: red thick arrows ($R \geq 10^9$ cm^{-3} μs^{-1}), blue mediate-thickness arrows (10^6 cm^{-3} μs^{-1} $\leq R <$ 10^9 cm^{-3} μs^{-1}), and black thin arrows ($R <$ 10^6 cm^{-3} μs^{-1}).

2.6.3.2 Dependency of quench reactions of He^m on T_g

In plasmas including He, He^m takes an important role in reaction dynamics. Here, the quench reactions of He^m were discussed. In the reaction set shown in Table 2.8, the generation reaction of He^m is only the electron impact excitation reaction (R1). On the other hand, six quench reactions were included in the reaction model. Among these reactions, the main reactions are R4, R6, R15, R20, and R21, and quenchers of He^m are He^m, He, N_2, O_2, and H_2O, respectively.

The dependency of the quench frequencies of He^m on T_g were discussed. Here, we calculated the quench frequencies of He^m by $n_{quencher} \times k_R$ for two body reactions (R4, R15, R20, and R21), and $n_{quencher}^2 \times k_R$ for three-body reaction (R6), where $n_{quencher}$ is the density of quencher species. The quench frequencies due to diffusion were calculated as $8D_i / d^2$ (cf. section 2.5.2). In the calculation, the density of He^m was fixed at 5×10^{11} cm^{-3} and the density of He and impurity species were the values in Table 2.11; namely, the impurity ratios of N_2, O_2, and H_2O were 96ppm, 24ppm, and 550ppm, respectively. For impurity species below its boiling point, if the vapor or sublimation pressure is

lower than the partial pressure of the species, the number density at the vapor or sublimation pressure at the temperature was used in the calculation.

Figure 2.36(a) shows the variations of the frequencies of the quench reactions of He^m and the dissipation frequency due to diffusion depending on T_g. The total quench frequency was also indicated in Figure 2.36(a) and continuously decreased with decreasing T_g. The inverse of the total quench frequency approximately corresponds to the lifetime of He^m. The drastic decrease of T_g occurred in two T_g ranges around 200 K and 35 K. These were caused by the rapid decrease of quench frequency of R21 (H_2O) around 200 K and those of R20 (O_2) and R21 (N_2) around 30 – 40 K. The sublimation pressures of H_2O at 200 K, O_2 at 40 K, and N_2 at 35 K are approximately 0.16 Pa, 0.15 Pa, and 0.34 Pa as shown in Figure 2.29 [26]. This low values of sublimation pressures suggested that the only small amounts of impurity species affected the quench reactions of He^m.

Figure 2.36(b) shows the ratio of the quench reactions of He^m. At the temperatures above approximately 200 K, R21 (quencher: H_2O) was most dominant, however, with increasing T_g, the ratio of three-body collision with He atoms (R6) increased. Between 40 and 200 K, the quench reactions due to N_2 and O_2 impurities were dominant. Around 35K, the ratio of N_2 exceeded 90% in narrow T_g range because of the relationship between the sublimation pressures of N_2 and O_2. At lower than around 30 K, the reaction of R4 and the diffusion became dominant. The reason why the component of diffusion became dominant was that the reactions other than R4 became almost zero at such low temperatures, as indicated in Figure 2.36(a). In other words, the reason was that the dependency of the reactions of R6, R15, R20, and R21 on T_g was much higher than that of the diffusion on T_g.

The variation of the quench frequency of He^m was not only caused by the phase transition of impurity species, but also by the variation of the components of collision cross section and collision frequency. Above 300 K where R6 and R21 are dominant. At the condition with 550ppm of water impurity, the total quench frequency increased around 25% with increasing T_g from 300 to 400 K. If the conditions were with less water impurity, the strong dependency of R6 was more pronounced because the quench frequency of He^m due to R21 decreased. For example, at 10ppm of water impurity ratio, the total quench frequency increase by 55% from T_g = 300 to 400 K. The large variations of the quench frequency (and lifetime) of He^m, which is dominant species in He plasma chemistry, implies that the dependency of plasma chemistry on T_g should not be ignored not only at cryogenic temperatures, but also at above room temperature.

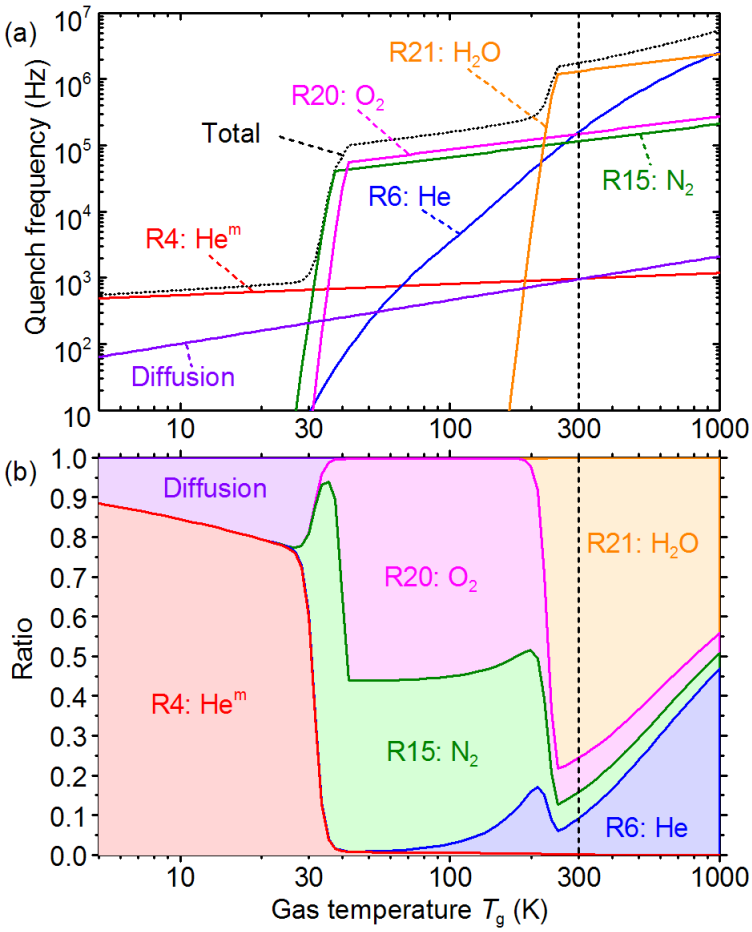

Figure 2.36 (a) Quench frequencies of He^m due to reactions [R4 (quencher: He^m), R6 (He), R15 (N_2), R20 (O_2), and R21 (H_2O)] and diffusion as a function of gas temperature T_g. The total quench frequency, whose inverse corresponds to the lifetime of He^m, is also indicated. (b) Cumulative line chart of ratios of the quench frequencies. The vertical dashed lines at T_g = 300 K are rough indication of room temperature.

2.7 Summary of chapter 2

In this chapter, to investigate the role of T_g in plasma chemistry, fundamental diagnostics of He cryoplasmas and discussion using my developed reaction model were conducted.

At first, T_g, which was the most important parameter in this study, was evaluated by laser heterodyne interferometry (LI) and thermal simulation (section 2.2). In the LI measurement, the spatially averaged T_g was evaluated and, on the other hand, in the thermal simulation, maximum possible values of T_{inc} were estimated in the assumption that the energy efficiency to contribute to increasing T_g was 100% (energy efficiency $\eta = 1$) and the heat transfer due to convection was ignored. The results of T_{inc} estimated by LI and thermal simulation showed a large difference, e.g., the T_{inc} at $T_d = 100$ K and $P_c = 32$ mW in metal electrodes with a diameter of 1.7 mm (Metal-1 electrodes) was 4 K by LI and 79 K by thermal simulation. As a result of the discussion about the possible errors of both methods, it was concluded that the value of T_{inc} estimated by LI was more accurate, although it can be a few times higher or lower than the actual T_{inc}. Therefore, it was concluded that the actual T_{inc} was suppressed below around 10 K and the actual energy efficiency was estimated approximately as a few tens of percent.

Then, the measurements by optical emission spectroscopy (OES) and laser absorption spectroscopy (LAS) were presented. As a result of time-resolved OES (TR-OES), the differences in the timings showing the maxima of the waveforms of the current, the He emission intensity, and the N_2^+ emission intensity were observed, which were unique to cryogenic temperatures. In the LAS measurements, the lifetime and the density of He^m at cryogenic temperatures showed a few hundred times longer and several dozen times higher than those at room temperature, respectively.

In order to clarify the mechanisms of these experimental results, the reaction model for He with small amount of impurities (N_2, O_2, and H_2O) was developed. The most striking feature of the model is that the dependencies of the reaction rate constants of elemental reactions and the diffusion constants of the species on T_g are taken into account. By using the model, the experimental results of OES and LAS were reproduced quasi-quantitatively or qualitatively. In addition, the contributions and the ratio of impurity species were evaluated.

Finally, the total reaction in He/N_2 system and quench mechanisms in $He/N_2/O_2/H_2O$ were discussed by using the reaction model, not only for reproducing the experimental results, but also for further discussion on plasma chemistry and its dependency on T_g. As a result, both the drastic variation of plasma chemistry due to phase changes and the gradual variation due to continuous variation of collision parameters (collision frequency, collision cross section, etc.) were confirmed. The dominant species and the elemental reactions transformed with decreasing T_g and how the plasma chemistry depends on T_g were clarified. In addition, even in the T_g range in which the drastic variations of the plasma chemistry do not appear, both absolute values and relative ratios of quench frequencies due to each reaction or diffusion were affected by the variation of T_g. Therefore, it was suggested that the dependency of the plasma reaction should not be ignored not only at cryogenic temperatures, but also above room temperature.

Thus, the role of the “new” parameter T_g for non-equilibrium plasmas was discussed and the importance of T_g was clarified. In He gas, the three-body reaction of He^m with He atoms, which needs a low activation energy

comparable to the energy of room temperature, was the most important elemental reaction. In addition, other reactions also showed a variety of T_g dependencies. By the combination of the variations in elemental reactions and the transition of phases, a dynamic variation in the plasma chemistry depending on T_g was caused. For other gas systems, although T_g might be less important compared to T_g for He plasma chemistry, the discussion about T_g should be inevitable to understand plasma chemistry and to control plasma reactions precisely.

Chapter 3

Electrical breakdown in high-density fluids

In this chapter, the electrical breakdown mechanisms in high-density fluids such as high-pressure gases, liquids, and supercritical fluids (SCF), particularly in the fluids having high fluctuations of local density (density fluctuations) near the critical point (CP), are investigated. The purposes are to clarify the role of high-density condition and the density fluctuations in electrical breakdown. By achieving the purposes, it is expected that a hint to describe the reaction mechanisms in SCF plasmas, which shows a unique reaction field to be able to syntheses a peculiar species, is obtained. Since cryoplasmas allow controlling T_g, they are useful to investigate temperature-sensitive phenomena such as the density fluctuations near the CP. Similar to a variety of phenomena showing a local-maximum or minimum (critical anomaly) such as transport properties, it has been observed that the breakdown voltage (U_B), which is the characteristic parameter in generation phase of plasmas, also indicates critical anomaly as a local minimum. In addition, the critical anomaly of U_B has been reported only for a few micrometer or shorter gap discharges, and the mechanism of the size dependency has not been clarified.

Elaborate experiments were conducted to obtain a measured U_B curve which allowed us to discuss the reaction mechanism in detail. Then, the effect of the density fluctuations on electrical breakdown in liquid(-like) phase and the electron motion in strong electric field in the fluids having high density fluctuations, particularly the effective mean free path of electron (λ_{fluc}), are modeled and discussed.

In section 3.1, the backgrounds of SCF plasmas and the critical anomaly of U_B are introduced and the purpose of the study in this chapter is described again. Then the experimental setup and results in He around the critical temperature of He (T_c =5.2 K) are shown in section 3.2. For the experimental results, three models are proposed in sections 3.3 – 3.5. In section 3.3, the modification of mathematical formulation of U_B, which had been proposed for gas phase breakdown voltages in previous study, was expanded to the expression of U_B for liquid (Bubble model). Next, the electrical breakdown model with a discussion on density-fluctuating fluid structure (Hard sphere cluster model) was proposed in section 3.4. The model describes the fluid structure with an assumption about the cluster-like structure in locally high-density region. In section 3.5, the hard-sphere cluster model is improved to “Local voids model” by focusing on a distribution of local density, instead of the individual clusters. In addition, the ion-enhanced field emission (IEFE) of electron from cathode, which has been proposed for electrical breakdown in micrometer gap at atmospheric pressure, was applied for high-density fluids. Finally, the experiments, proposed models, and their results are summarized in section 3.6.

3.1 Background

3.1.1 Supercritical fluids (SCFs)

Supercritical fluids (SCFs) are fluids in a state where T and P are both above those at the CP of the fluids (Figure 3.1). Figure 3.2 shows the T-P-n phase diagram of He. The difference in n between gas and liquid becomes small with reaching to CP, and in SCF state, there is no density jump between gas-like and liquid-like states. The T, P, and n at the CP are called the critical temperature (T_c), the critical pressure (P_c), and the critical density (n_c), respectively. The values of T_c, P_c, and n_c are inherent for each fluid, and T_c and P_c of various fluids are plotted in T-P diagram as shown in Figure 3.3. There are no phase transitions between gas and SCF, and between SCF and liquid. SCF can be divided into gas-like SCF and liquid-like SCF as extensions from gas and liquid phases, respectively. The transition line between gas-like and liquid-like SCFs are the extension of coexistence curve of gas and liquid, and at the points on the line, the density fluctuations and the correlation length show local maximum. The transition line is called as "the ridge line of the density fluctuation" [98,99] or "Widom line" [100]. While various properties vary dynamically and continuously in the vicinity of the Widom line, the variation of the properties on the Widom line gradually diminishes with leaving from the CP and the transition between gas-like and liquid-like SCFs becomes fuzzy.

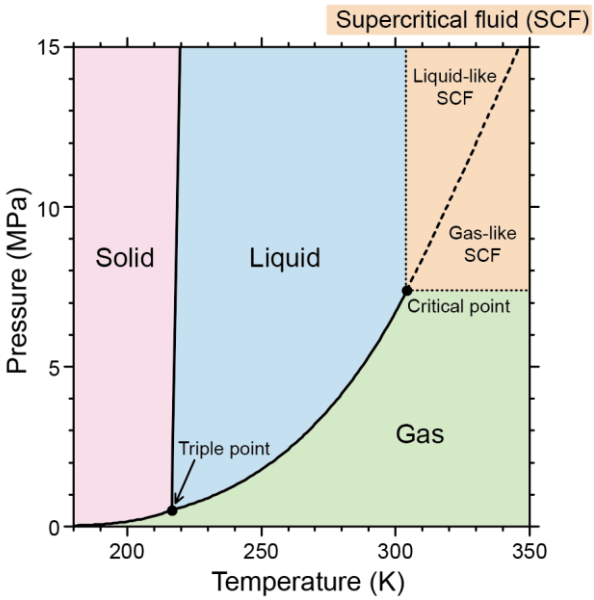

Figure 3.1 Temperature-pressure phase diagram of CO_2.While the transitions among gas, liquid, and solid are indicated as solid lines, the borders between gas and SCF and between SCF and liquid are broken lines because there are no phase transitions. SCF can be divided into gas-like and liquid-like SCFs by the ridge line of the density fluctuation" [98,99], so-called, "Widom line" [100].

SCFs have intermediate properties between gas and liquid, i.e., liquid-like transport properties (such as high density, high thermal conductivity, and high solvency power) and gas-like transport properties (such as high diffusivity, low viscosity, and zero surface tension) (Figure 3.4) [101]. In addition, various properties, such as electric permittivity and ion product, can be controlled from gas-like values to liquid-like values by controlling *T* and *P*.

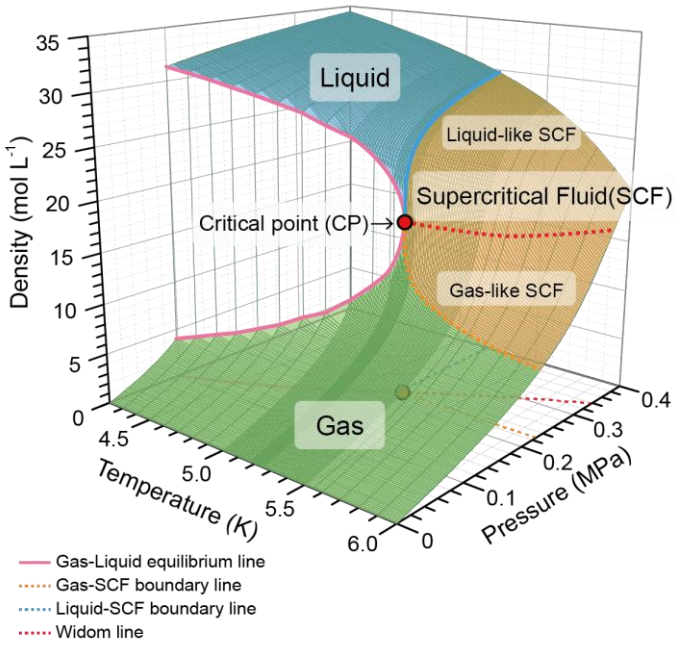

Figure 3.2 Temperature (*T*) – Pressure (*P*) – Density (*n*) phase diagram of He. Combinations of *T*, *P*, and *n* on the curved surface are realized in equilibrium state.

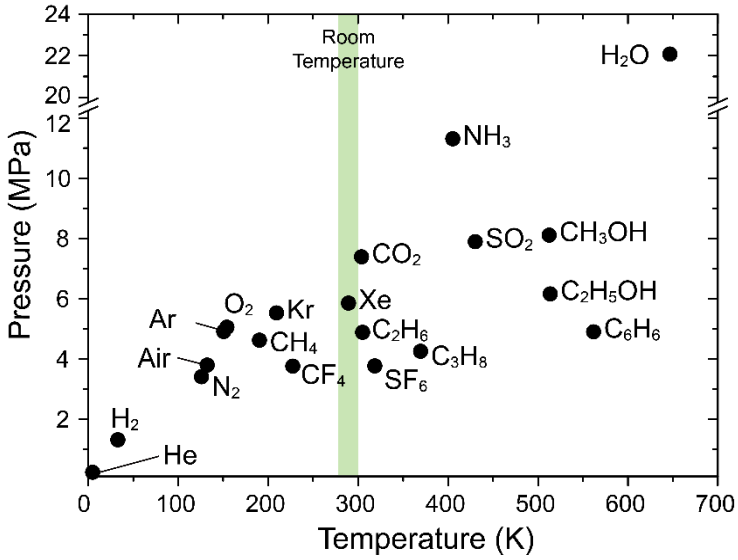

Figure 3.3 Critical points of the fluids plotted on a temperature-pressure diagram. The temperature range of room temperature are shaded as green.

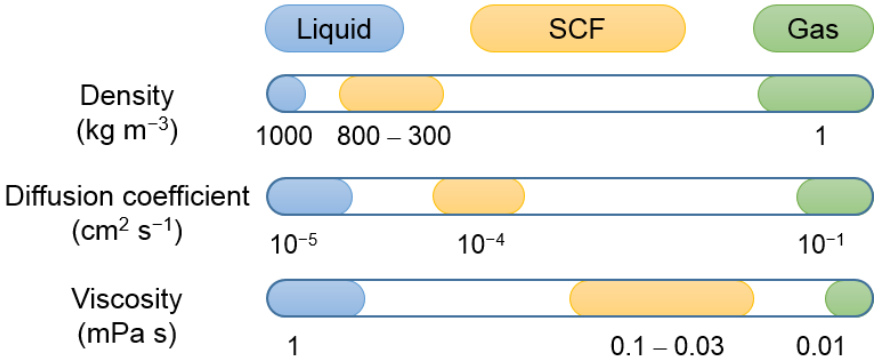

Figure 3.4 Schematic of the typical properties of liquid, supercritical fluid (SCF), and gas. The values are indicated approximately on a logarithmic scale. The values were retrieved from Ref. [101].

By using such unique characteristics, SCF reaction processes of environmentally-friendly reaction solvents such as water (H_2O) and carbon dioxide (CO_2) have been studied and partially developed. These SCF solvents are expected to replace organic solvents having explosiveness or toxicity. Various applications of SCFs have been studied, such as organics decompositions [102], extractions [103], analytics [104], drying [105], and materials syntheses [106,107].

3.1.2 Critical anomaly and density fluctuations in SCFs

In SCFs, at the conditions far from the CP, since the spatial and temporal fluctuations of local number density, the fluid structure is almost homogeneous. Meanwhile, near the CP, the local density heavily fluctuates [108] because

condensing power due to intermolecular force and the thermal agitation balances. Therefore the fluid structure shows a long-range correlation. This density-fluctuation structure forms a kind of the gas-liquid multiphase nanostructure composing of gas-like voids and liquid-like clusters.

Near the critical point, unique characteristics, so-called critical anomalies, which are of interest in various scientific fields, arise, for example, thermophysical properties, such as the local maxima or minima of thermal conductivity [109–112], isobaric specific heat [113], sound speed [114], and partial molar volume [115,116]. Figure 3.5 indicates the thermal conductivity and the speed of sound in CO_2 near its CP which are cited from the database of the thermophysical properties "REFPROP" [26]. In addition, the critical anomalies in a broad sense are observed in the interactions with external stimulations, such as critical opalescence [117,118], local maxima of reaction rate constants [119–121], and local maxima of swelling of polymers [122,123].

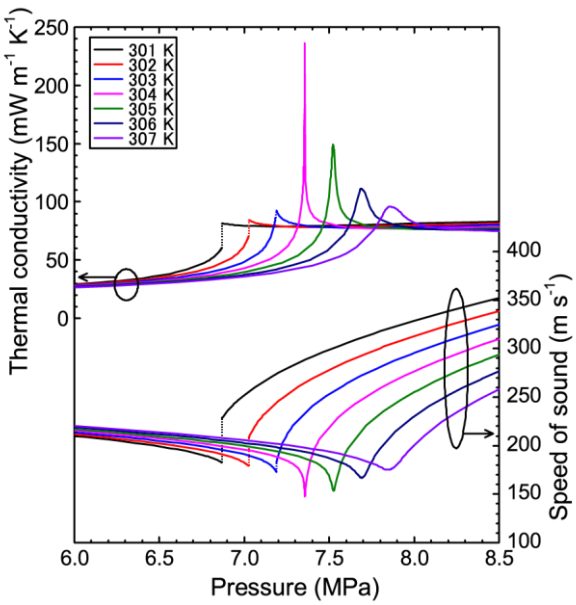

Figure 3.5 Thermal conductivity and speed of sound in CO_2 near its CP (T_c = 304.2 K, P_c = 7.38 MPa). The values were cited from the NIST database of thermophysical properties "REFPROP" [26].

These critical anomalies should have a relationship with the microscopic fluid structure of the density-fluctuation. The parameters expressing the magnitude of the density fluctuation are F_D and ξ.

The term of F_D is defined as a fluctuation of the number of particles and expressed as [108]:

$$F_D \equiv \langle (N - \langle N \rangle)^2 \rangle / \langle N \rangle = \kappa_T / \kappa_T^0 \tag{3. 1}$$

where $\langle x \rangle$ denotes the average of x, N is the number of particles in a given volume, κ_T is the isothermal compressibility, and κ_T^0 is κ_T of the ideal gas. F_D = 1 for an ideal gas and a high F_D means that the fluid fluctuates strongly. F_D can be estimated by using thermophysical databases such as REFPROP [26]. For an ideal gas, F_D = 1 and a high F_D means

that the fluid strongly fluctuates. The magnitude of F_D strongly depends on the thermophysical conditions near the CP [Figure 3.6(a)]. The graph shows that F_D diverges at the CP and the ridge of F_D divides SCF into two regions (gas-like and liquid-like). The schematics of the fluid structures at the conditions in Figure 3.6(a) are indicated in Figure 3.6(b) – (g).

While F_D are defined by considering the number of particles in a given volume, the correlation length ξ is a characteristic length of the fluid structure created by density fluctuations. ξ is defined in the Ornstein-Zernike theory [108] and, in the theory, the density-density (long-distance) correlation function, $g(r)$, can be approximated using ξ as

$$g(r) = k_B T \kappa_T \frac{\exp(-r/\xi)}{4\pi\xi^2 r} \tag{3. 2}$$

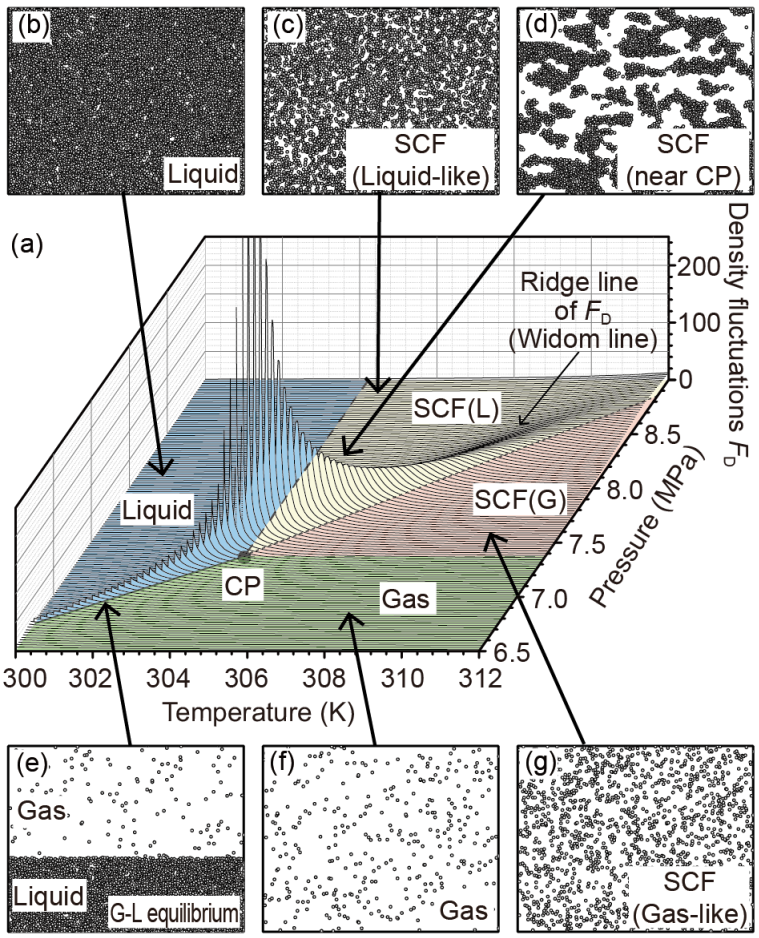

Figure 3.6 (a) The isobaric variation of the magnitude of the density fluctuation F_D on the temperature-pressure phase diagram of CO_2. The excess of F_D near the critical point (CP) are cut. (b-g) The schematics of the fluid structures in (b) liquid, (c) liquid-like SCF [SCF(L)], (d) SCF near CP, (e) equilibrium state of gas and liquid [G-L equilibrium], (f) gas, and (g) gas-like SCF.

where r is a distance, k_B is the Boltzmann constant. While the value of ξ can be estimated by X-ray small angle scattering [98], it is difficult to estimate the value of ξ from databases of physical properties unlike F_D.

The relationship between F_D and ξ can be expressed as [6,35]

$$\xi = R' F_D^{0.5} \tag{3. 3}$$

where R' is the second momentum (or direct-correlation range) of the direct correlation function [108]. R' is independent of T and varies with n_p in an almost linear fashion for small coefficients.

As a phenomenon forming molecule clusters, solvation can occur in SCF in mixture fluid. The solvation is not unique phenomenon near the CP, unlike the density fluctuation. Since the difference between a local density around a solute molecule and an average density in the solvation in SCFs is larger than that in the solvation is liquids, clusters form. When the fluctuations of local number density themselves are discussed in mixture fluids, the solvation should not be ignored. However, in this study, since we used a pure fluid, we could take into account only the density fluctuations.

Concerning the timescale of the density fluctuation, the aggregation and dispersion of clusters repeatedly and quickly occurs in SCF near CP, and the time to take the exchange of particles in a cluster was suggested to be on the order of picoseconds [125,126]. While the timescale is shorter than that of the light-emissive relaxation of the excited states of gas molecules (nanosecond – microsecond), it is longer than the average time between a collision and the next collision of electron (femtosecond).

3.1.3 SCF plasmas

In recent years, media for plasma generation have been extended from low-pressure gases to high-pressure gases, such as atmospheric pressure gases [127,128]. Since atmospheric pressure plasmas (APP) has the advantages of the room conditions, i.e., low-cost experimental equipment without expensive vacuum pumps and affinity for polymers and biomaterials, they open up a variety of new applications of plasmas. In addition to gas phase plasmas, plasmas in liquids [13,129] have attracted much attention recently. For example, knowledge on interaction between plasmas and water are very important for plasma medicine and other applications such as nanomaterials syntheses in liquids. Moreover, by including the small-scale condensed phases, such as clusters or droplets whose size are μm – nm, in plasmas, innovative materials processing have been achieved, for example, a single step partial oxidation of methane converted to methanol and other liquids with around 10-times high efficiency than conventional methods [130]. These are caused by utilizing the effects regarding interface between plasma and condensed phases, the advantage of condensed phase in plasmas, and their hybrid effects. Then, the mixture of gaseous and liquid phases in nanometer scale can be emerged in the SCFs with high density fluctuations.

Studies of discharges in SCFs started around 1900 for high-pressure discharge lamp or elementary analysis [131], mainly in the field of electric discharge engineering. Then, the properties of the electrical breakdown in supercritical

CO_2 began around 1950 [132], that in supercritical He for refrigerant and insulant of superconducting cables started around 1960 [133,134], and recently the breakdown mechanisms using nanosecond pulse discharge have been studied [135,136].

In this century, along with the advance of microplasmas technologies, the studies of plasmas in SCF from the view point of materials science and engineering have started. In many cases, the plasmas in SCFs are gaseous plasmas surrounded by SCF media, namely "plasmas in SCF". Meanwhile, by controlling the discharges, the fluid structure of the density fluctuations can be preserved in plasmas. Since this kind of plasmas can be considered as a different phase from gaseous plasmas, it is called "SCF plasmas".

Figure 3.7 shows results of Raman scattering spectroscopy for SCF plasmas in CO_2, which indicates that the fluid structure having local density fluctuation declined but preserved in the SCF plasmas [137].

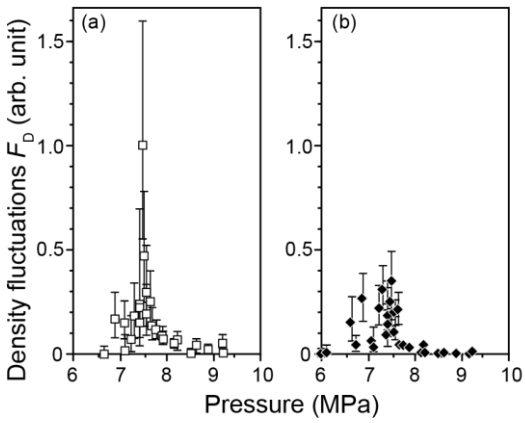

Figure 3.7 Density fluctuation of CO_2 (a) without and (b) with plasma generation. The values of F_D were estimated from Raman spectroscopy [137].

The application studies of SCF plasmas for materials syntheses and deposition have been developed. SCF plasmas have the advantages of both SCF processes, such as unique properties between gas and liquid, high-reactivity, and controllability of the properties, and plasma processes, such as rapid, low-temperature, and non-equilibrium reactions. By using these properties, the high-speed growth of carbon nanotubes and other carbon materials at the lower temperature without catalysis compared to can be achieved [138]. In addition, near the CP, they have unique properties showing critical anomalies and nanometer-scale fluid structure due to the density fluctuations. In the silicon nanocrystals syntheses by SCF plasmas generated by laser ablations, the various silicon nanocrystals emitting different colors can be synthesized by using the controllability of SCF conditions, and moreover, amount of synthesized nanocrystals showed local maxima at the conditions on the Widom line [139].

In recent years, in addition to such critical anomalies of thermophysical properties, critical anomalies related to electrically charged particles have been reported. For example, local minima of U_B in micrometer-scale

discharges [140–144], local maxima of emission intensities in plasmas generated by pulsed laser ablation [145], and the peculiar behavior of cavitation bubbles subsequent to the generation of plasmas by pulsed laser ablation [146]. Also, increased yields in the syntheses of nanomaterials by discharge and laser-ablation plasmas in SCFs near the CP have been reported, such as nanodiamonds [147], and molecular diamond [148,149]. These critical anomalies imply that electron motion is highly affected by the local fluctuation of the particle density in fluids near the CP; however, studies on the motion of charged particles in such fluctuating fluids have not allowed clarifying the mechanism of these critical anomalies. Critical anomalies related to plasmas have been reported, such as local minima of U_B in micrometer-scale discharges [140,142,143] and increased yields in the syntheses of nanomaterials by plasmas in SCFs near the CP [139].

3.1.4 Breakdown voltages and their critical anomaly

Investigation of the critical anomaly of U_B is expected to give information about the electron motion and the reaction mechanisms in fluctuating fluids. In this study, we discuss the critical anomaly of U_B. Before the introduction of the critical anomaly of the breakdown voltages, the conventional mechanisms of electrical breakdown in gas phase are introduced in section 3.1.4.1 and the deviation from the conventional mechanisms in micrometer-gap discharges in section 3.1.4.2. Then, we introduce the critical anomaly of the breakdown voltages.

3.1.4.1 Electrical breakdown in gas phase

Before introducing electrical breakdown near CP, a general gas breakdown is introduced here.

There are several kinds of initiation theories of electrical discharges in gas, such as Townsend theory, streamer theory, and corona theory. In this chapter, Townsend discharge are introduced because this discharge theory is basic and the electrical breakdown models proposed in this study were based on the Townsend theory.

In the Townsend theory, two reactions are considered. One is the electron avalanche due to the acceleration of electron (α effect), and the other is the secondary electron emission due to the electron impact to a cathode (γ effect). The first Townsend coefficient (α) and the secondary emission coefficient (γ) are defined for each reaction: α indicates the number of ionization events caused by an electron in a unit-length path along an electric field and γ indicates the number of electrons emitted from the cathode per incident positive ion [150]. In the theory, the following equation is satisfied when breakdown occurs:

$$\gamma \times [\exp(\alpha d) - 1] \geq 1. \tag{3. 4}$$

This equation means that breakdown occurs when more than one electrons are generated by the impact to a cathode of ions generated by electron avalanche caused by one seed electron.

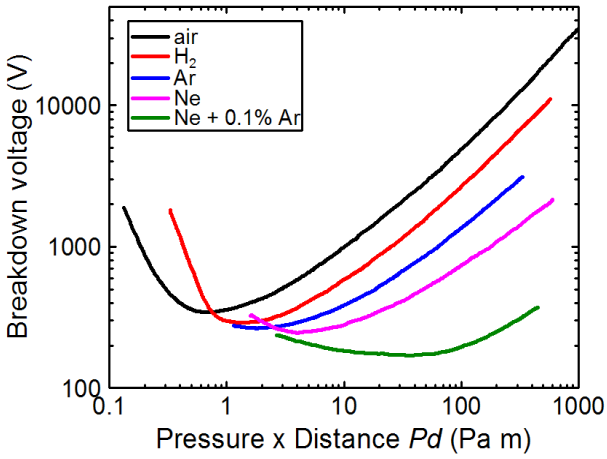

Figure 3.8 Breakdown voltage curve as a function of a product of pressure and distance (*Pd*), so-called "Paschen's curves", of air, H_2, Ar, Ne, and the mixture of Ne with 0.1% Ar [151].

When Townsend discharge occurs in homogeneous electric field between parallel plate electrodes, the values of U_B can be expressed as a function of a product of n and d (often using P instead of n, although P can only be used when the experimental conditions ensure proportionality between P and n). This law is called as "Paschen's law" and a curve of U_B as a function of $n \times d$ is "Paschen's curve". As indicated in Figure 3.8, Paschen's curve shows a minimum at a specific $P \times d$ or $n \times d$ (Paschen's minimum) [151]. The breakdown voltages of the mixture of Ne and 0.1% Ar are lower than those of pure Ne and Ar due to the Penning effect.

3.1.4.2 Deviation from Paschen's curve in micrometer-gap discharge at atmospheric pressures

The deviation of U_B from Paschen's curve at atmospheric pressure, which has only been observed on the left branch of Paschen's curve in very small gap discharges (typically: $d < 10$ μm), has been investigated intensively (Figure 3.9) [152–164]. The main motivation for these studies was the prevention of unintended breakdown leading to spark discharges as well as applications to gas sensing and analysis, and lighting [153,161]. The values of U_B as a function of Pd, including the deviation from the conventional Paschen's law, form the so-called modified Paschen's curve [153–155].

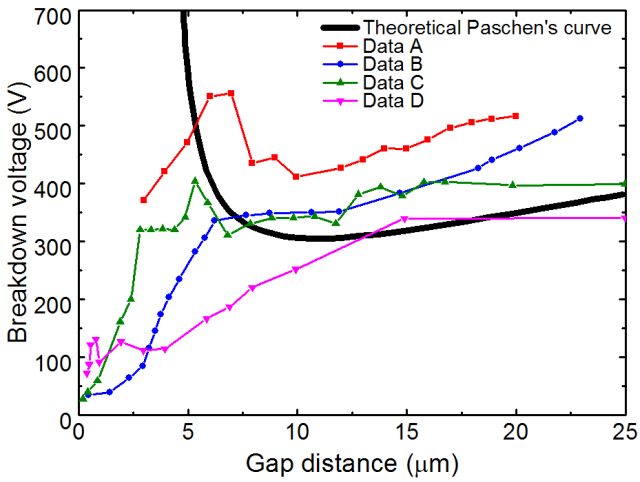

Figure 3.9 The experimental results showing the deviation from Paschen's curve in very narrow gap distances and the theoretical Paschen's curve in air. The data of A, B, C and D were retrieved from [153], [162], [163], and [164], respectively.

The modified Paschen's curve has been reported to be reproduced by considering ion-enhanced field emission (IEFE) from a cathode. IEFE is field emission enhanced by the thinning of the potential barrier in the vicinity of the cathode owing to positive ions approaching the cathode [152,161]. Figure 3.10 shows a schematic of potential curve of IEFE. At first, the mathematical formulation for the modified Paschen's curve was suggested using an assumption that the potential field is linearly modified by the approaching ions. Then, the effect of IEFE has recently been investigated by a fully analytical model of the distortion of an electric field by positive ions near the cathode [165]. However, the differences between the calculation results for U_B obtained by the model under the linear assumption and by the fully analytical model are small (< 10%) [165]. Since the parameters in this study such as d have an uncertainty of more than 10%, we consider that the model with the linear assumption is sufficiently accurate for this study.

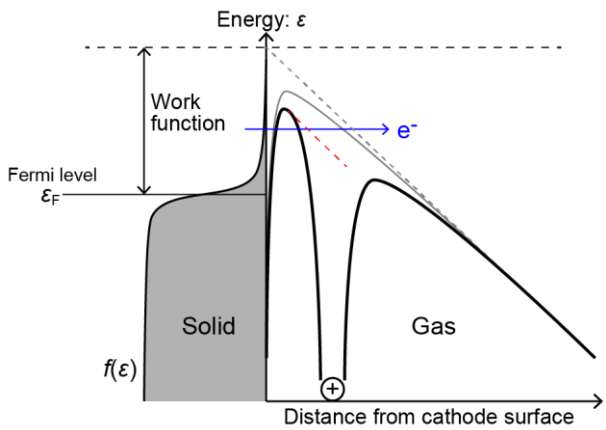

Figure 3.10 Schematic of potential curves near a cathode when a positive ion is approaching the surface of the cathode. The curve of $f(\varepsilon)$ is the electron energy distribution function on the cathode surface and the gray-shaded area means the occupation of electron. The gray solid line is the modified potential curve by the applied electric field without the effect of the positive ion.

In following, the mathematical formulation of the modified Paschen's curve including the effect of IEFE is introduced with a little modification for fitting the experimental and calculation conditions in this study.

The modified Paschen's curve is expressed by incorporating the potential field of the approaching ions into the Fowler-Nordheim equation. The Fowler-Nordheim equation gives the field emission current j_{FE} [166]:

$$j_{\mathrm{FE}} = C_{\mathrm{FN}} E_{\mathrm{A}}^2 \exp\left(-\frac{D_{\mathrm{FN}}}{E_{\mathrm{A}}}\right) \tag{3. 5}$$

where C_{FN} and D_{FN} are parameters related to the work function (ϕ) of the cathode and are loosely dependent on the electric field. The effective electric field on the cathode (E_{A}) is expressed as

$$E_{\mathrm{A}} = \beta E \tag{3. 6}$$

where β is the geometric field-enhancement factor and E is an average electric field between electrodes.

In the mathematical formulation of the modified Paschen's curve, γ is modified by IEFE as follows:

$$\gamma = \gamma_{\mathrm{i}} + \gamma' \tag{3. 7}$$

where γ_{i} is the secondary electron emission mainly due to the Auger neutralization effect [150] and γ' is that due to IEFE. The value of γ_{i} is assumed to be independent of P in this model. The following mathematical expression of γ' was originally suggested by Boyle and Kisliuk [152] and implemented by Radmilović-Radjenović and Radjenović [156]:

$$\gamma' = K\exp\left(-\frac{D_{\mathrm{FN}}}{E_{\mathrm{A}}}\right) \tag{3. 8}$$

where K is a parameter, which has been analytically determined to be [159]

$$K = \frac{10C_{\mathrm{FN}}\beta^2 d}{\varepsilon_0\mu} \tag{3. 9}$$

where ε_0 is the permittivity of vacuum.

C_{FN} and D_{FN} can be expressed as [167]

$$C_{\mathrm{FN}} = a_1/[\phi t^2(y)], \tag{3. 10}$$

$$D_{\mathrm{FN}} = a_2\phi^{\frac{3}{2}}v(y), \tag{3. 11}$$

where $a_1 = 1.54 \times 10^{-6}$ A eV V^{-2}, $a_2 = 6.83 \times 10^9$ eV V m^{-1}, and $t(y)$ and $v(y)$ are nondimensional parameters that are functions of a nondimensional parameter y.

By combining Equations (3. 6), (3. 8) – (3. 11), the value of γ' is expressed as

$$\gamma' = \frac{10a_1\beta^2 d}{\varepsilon_0\mu\phi t^2(y)}\exp\left(-\frac{a_2\phi^{\frac{3}{2}}v(y)}{\beta E}\right). \tag{3. 12}$$

Concerning the estimation of y, $v(y)$, and $t(y)$, y can be expressed as [167]

$$y = a_3E_{\mathrm{A}}^{1/2}/\phi = a_3(\beta E)^{1/2}/\phi \tag{3. 13}$$

where $a_3 = 3.79 \times 10^{-4}$ eV V$^{-1/2}$ m$^{-1/2}$. We estimated $v(y)$ [94,168] and $t(y)$ [168] to be

$$v(y) = 0.2792y^3 - 1.180y^2 - 0.09681y + 1 \tag{3. 14}$$

$$t(y) = -0.06394y^3 + 0.1422y^2 + 0.03176y + 1 \tag{3. 15}$$

which are expressions fitted to the values in the references. We confirmed that the differences between the values in the previous studies and the calculated values obtained from Equations (3. 14) and (3. 15) are within 3% for both $v(y)$ and $t(y)$.

From Equations (3. 12) – (3. 15), γ' can be estimated by determining the parameters E and d related to the experimental conditions and the parameter β related to the surface condition of the cathode. The assumption concerning E and β in this study are expressed in section 3.5.1.1 and 3.5.1.2, respectively.

Meanwhile, the deviation of U_{B} has also been observed for the right branch of Paschen's curve at very high P (typically: > 1 MPa) [133,152,169–172]. The deviation from the right branch has been observed at larger d, for example, for d = 1 mm at about P = 1000 kPa at room temperature in air [171], for d = 1.5 mm at about P = 80 kPa at T = 4.2 K in He [133], and for d = 10 mm at about P = 200 kPa at room temperature in SF_6 [169]. The deviations from the conventional Paschen's curve have been reported to be caused by ion-enhanced field emission (IEFE) from the

metal cathode [152], and those from the left branch of Paschen's curve can be reproduced by a mathematical formulation based on the Townsend breakdown model by modifying the secondary Townsend coefficient (γ) [153,158,159]. However, the validity of the numerical expression for the modified Paschen's curve has not yet been confirmed for high P.

3.1.4.3 Critical anomaly of breakdown voltages

The critical anomaly of the breakdown voltages has been observed in various fluids, such as those made up of monatom (xenon (Xe) [142]), nonpolar molecule (carbon dioxide (CO_2) [140–142]), and polar molecule (water [142]), and mixed fluid (air [143]). Figure 3.11 shows the measured U_B and the fitting curves in Xe [142]. In these studies, it was suggested that the local minima of U_B near the CP were caused by the concomitant effect of efficient electron acceleration in a void space and the low ionization potential of solid clusters [173–175], which are both generated by the density fluctuations [140,142]. In addition, there may be a rapid change of gradient of U_B curve around 3 MPa. This was suggested to be due to the rapid change in the mobility of negative charges [176,177], probably due to an electron attachment to clusters formed in high-pressure gas [142].

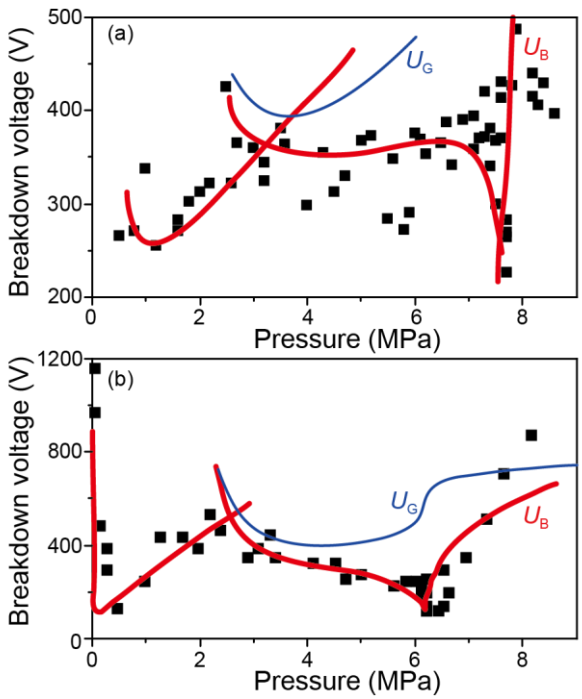

Figure 3.11 Experimental results of breakdown voltages and theoretical fitting curves for (a) CO_2 at T = 305.65 K [141] and (b) Xe at T = 292.15 K [142]. The black squares show the experimental results. The curves of U_G and U_B represent the theoretical fitting curves calculated from Eqs. (3. 16) and (3. 17).

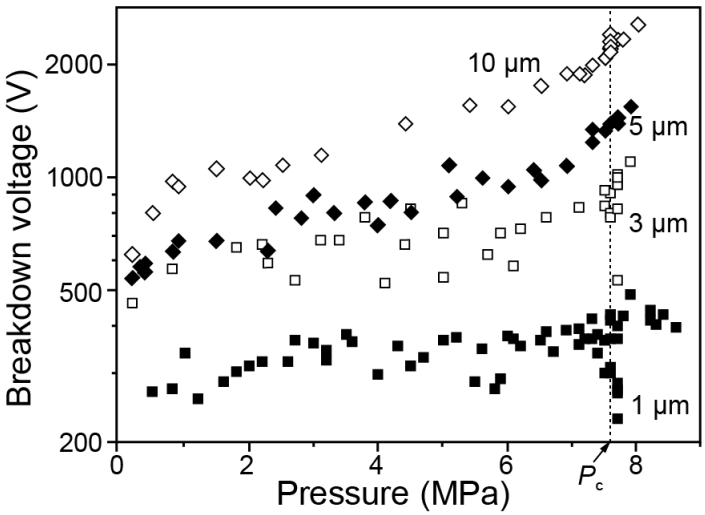

Figure 3.12 Breakdown voltages in high-pressure CO_2 with coplanar thin-film electrodes of 1, 3, 5, and 10 μm gap distances.

One of the notable characteristics of the critical anomaly of U_B is that it has only been observed in micrometer-scale discharges [$d < 5$ μm] and that the local minimum of U_B was more pronounced for smaller d (~ 1 – 3 μm) [140,142]. Figure 3.12 shows that the dependency of the breakdown voltages on the gap distance in CO_2. For larger d ranging from 25 μm to 5 mm, the variation of U_B and the breakdown mechanisms in SCFs including the region near the CP have been studied [133,134,136,178–181]. However, these studies have not reported the existence of a local minimum of U_B near the CP, and the mechanism of the dependence of the critical anomaly of U_B on d has not yet been revealed.

To evaluate the effects of the density fluctuations on U_B, a modification of Paschen's law [182] by combining it with a power law containing a dimensionless parameter F_D was proposed. The value of U_G, which means the breakdown voltage in gas phase without the effects of the density fluctuations, and that of U_B were expressed as

$$U_G = \frac{dn\sigma\Phi}{AB}\left\{\ln(dn\sigma) - \ln\left[ln\left(\frac{1}{\gamma}+1\right)\right]\right\}^{-1}, \tag{3. 16}$$

$$U_B = C_1 U_G F_D^{-C_2} \tag{3. 17}$$

where σ is electron-to-particle cross section, ϕ the ionization potential, A the effective coefficient related to the electrode sharpness, B a coefficient associated with Lorentz's internal field [183] and is described as

$$B = \frac{1}{3}(\varepsilon + 2), \tag{3. 18}$$

and C_1 and C_2 are individual coefficients. In addition, in order to reproduce the change of the gradient of measured U_B around 3 MPa using the same equations, two sets of the calculation parameters were used.

The results of the calculated U_G and U_B are shown in Figure 3.11 as thin and thick lines, respectively. Although

this modification allowed the reproduction of experimental U_B values in each fluid reasonably well, this model was purely phenomenological, making it difficult to link it to fundamental physical observations.

Moreover, as an issue of the experimental results in the previous studies, the number of measured U_B was at most 50 for each temperature. This is due to the limitation of the coplanar thin-film electrodes in previous studies. The electrodes must be replaced every measurement because of the damage of them. Therefore, the issue of the electrode damage should be improved to discuss more precisely.

3.1.5 Purpose

For a more detailed investigation of the electrical breakdown in high-density fluids with strong density fluctuations, it is necessary to establish a new model of the electrical breakdown that reproduces two characteristics of the electrical breakdown near the CP, i.e., the critical anomaly itself and its dependence on d. In this thesis, I propose electrical breakdown models and discuss their validity by comparing calculated U_B by the models with the measured U_B. Moreover, we discuss the physics related to the electron motion in fluids with large density fluctuations. It is expected that this discharge model, which takes into account the density fluctuations, might provide further insights into the motion of charged particles in fluids exhibiting local density fluctuations, into the origin of the critical anomaly of the electrical breakdown, and into the other critical phenomena mentioned above.

In this study, the roles of high-density fluids and the density fluctuation on the generation of high-pressure non-equilibrium plasmas were investigated by measuring the electrical breakdown in He (T_c = 5.20 K, P_c = 0.227 MPa, n_c = 17.4 mol L^{-1} [31]) at cryogenic temperature and by establishing electrical breakdown models.

In general, an SCF exhibits intermediate properties between those of a gas and a liquid, and the SCF phase are divided into two regions: gas-like and liquid-like SCFs. Three models were developed to discuss the critical anomaly of U_B based on liquid or gaseous breakdown models. While the first model in section 3.3 was expanded from the liquid(-like) phases, the other two models, described in sections 3.4 and 3.5, were expansion from the gas(-like) phases. Note that these models have been developed using different approaches and do not conflict with each other.

3.2 Experiments

3.2.1 Experimental conditions

In this study, we used He. Since T_c of He is at a very low temperature where all matters else are solidified, the fluid near the CP of He must be extremely pure He. Moreover, He is a monatomic. Therefore the discussion of the critical anomaly of U_B in He should be simple. In addition, the damage of the electrodes should be smaller due to the light weight of He atom. This was crucial to conduct experiments without replacing electrodes.

The discharge experiments were performed using tungsten (W) electrodes separated by gaps of 3 ± 1 μm, the tips of which were etched electrochemically [30]. The electrodes were not coplanar configuration but the sphere-sphere configuration. The curvature of the tips was measured to be 25 ± 5 μm by scanning electron microscopy (JEOL JSM 6060LV). We assume that the electric field between the electrodes was quasi-uniform because the tip radii were sufficiently large in comparison with d. The electrodes were placed in a high-pressure cell inside a vacuum chamber to allow precise control of the temperature (4 K chamber, Figure 2.3). The experiments were conducted at temperatures (T) from 5.02 to 5.50 K (T/T_c = 0.965 – 1.06) and in a pressure (P) range between 0.03 and 0.30 MPa (P/P_c = 0.132 – 1.32) (Figure 3.13), corresponding to a number density (n) range between 1 and 27 mol L^{-1} (n/n_c = 0.0574 – 1.55). These conditions include the CP of He and its three fluid states: gas, liquid, and SCF. In the measurements, the He pressure (density) was increased continuously while keeping the temperature constant. Temperatures were set at every 0.5 K from 5.10 – 5.50 K, but the measurements at T = 5.35 K were invalid due to a technical problem. The minimum temperature was 5.02 K due to a limitation of the experimental setup and method in this study. We note that the maximum and minimum pressure in this study were not the same for the measurements at different temperatures.

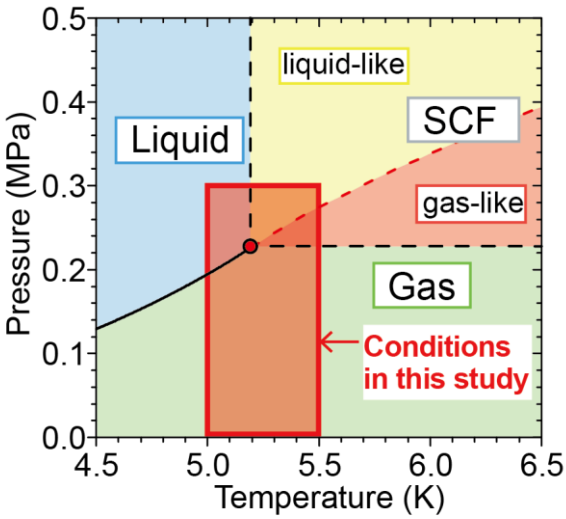

Figure 3.13 *T-P* phase diagram of He near the critical point. Area of conditions where experiments were conducted in this study is indicated as red-shaded square.

The inlet flow rate of He (purity: >99.99995%, TAIYO NIPPON SANSO Corp.) was kept at 1 cm^3 min^{-1} at each temperature and it was found to cause little turbulences inside the fluid. The effect of impurities could be ignored because all species except He become solid at such a low temperature. Even if there might be a very small number of particles (either solidified impurities or from the erosion of the electrodes), their effect on the observed electric discharge behavior is negligible due to their extremely small fraction in such a high density of He. We developed an automatic measurement system to record T, P, and U_B simultaneously when electrical breakdown occurs. Every 60 – 120 s, a DC voltage was applied to the electrodes, and the voltages were recorded by a digital oscilloscope. The density steps between measurements (< 0.1 mol L^{-1}) were much smaller than those in previous studies [140–142].

Since the measurements were conducted with a fixed inlet flow of 1 cm^3 min^{-1}, the pressure (density) continued increasing during the measurements and there should not be any duplicate measured U_B values at the same density. The increase in density between individual measurements was below 0.1 mol L^{-1}. However, in some figures in this paper, some of the increases in density between measurements – especially near the CP – are larger than 0.1 mol L^{-1} and more than one value exists at the same density. This is because the isothermal compressibility was so high that we could not measure the difference in pressure for each measurement by our three-digit pressure gauge (PG35, Copal). To avoid any "conditioning effects" [133,171] that could affect the value of U_B, we started the measurements after more than 100 electrical discharges at each T. All values of n in our experiments were calculated by REFPROP [26] using the measured values of T and P.

3.2.2 Experimental results

Figure 3.14 shows the variations of the breakdown voltages at T = 5.250 K as a function of P. The variations of F_D, which were calculated by Equation (3. 1) using the parameters obtained from the NIST database of thermophysical properties of fluid systems [31], was also presented in Figure 3.14. The most striking feature of the U_B curves is that they show local minima at almost the same value of P where F_D reaches a maximum. Figure 3.15 indicates the experimental results of various temperatures as a function of normalized pressure (P/P_c') which is the pressure normalized by the pressure on the Widom line (P_c') depending on the temperature. The local minimum was most pronounced at T = 5.25 K corresponding to the temperature close to T_c. Although the condition of T = 5.20 K is the closest to T_c, the critical anomaly at T = 5.25 K was larger than T = 5.20 K. This is probably due to the heat noise where the condition very close to CP should be very sensitive, in spite of the high controllability of the ambient condition of cryoplasmas.

To the best of our knowledge, this is the first report on such a critical anomaly of electric discharges in He. The main difference between this study and previous studies not showing the critical anomaly [21–26] is the gap distance. The distances in our study and the previous studies are 3 μm and more than tens of micrometers, respectively. This suggests that the gap distance needs to be close to the characteristic length of the structure of the density-fluctuating fluid [142] in order to observe this correlation between U_B and F_D.

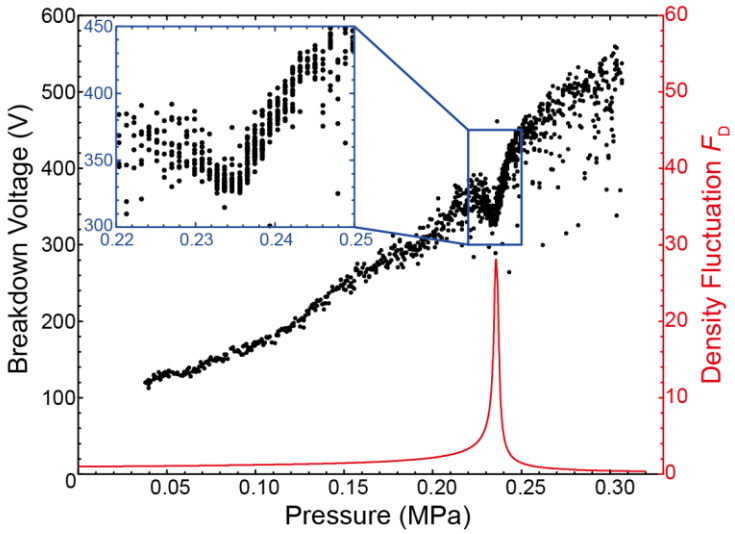

Figure 3.14 Breakdown voltages (black dots) and density fluctuation F_D (red lines) as a function of helium pressure at temperatures of 5.25 K. The experimental U_B plots at the pressures near the maximum of F_D are magnified in the upper-left of the figure.

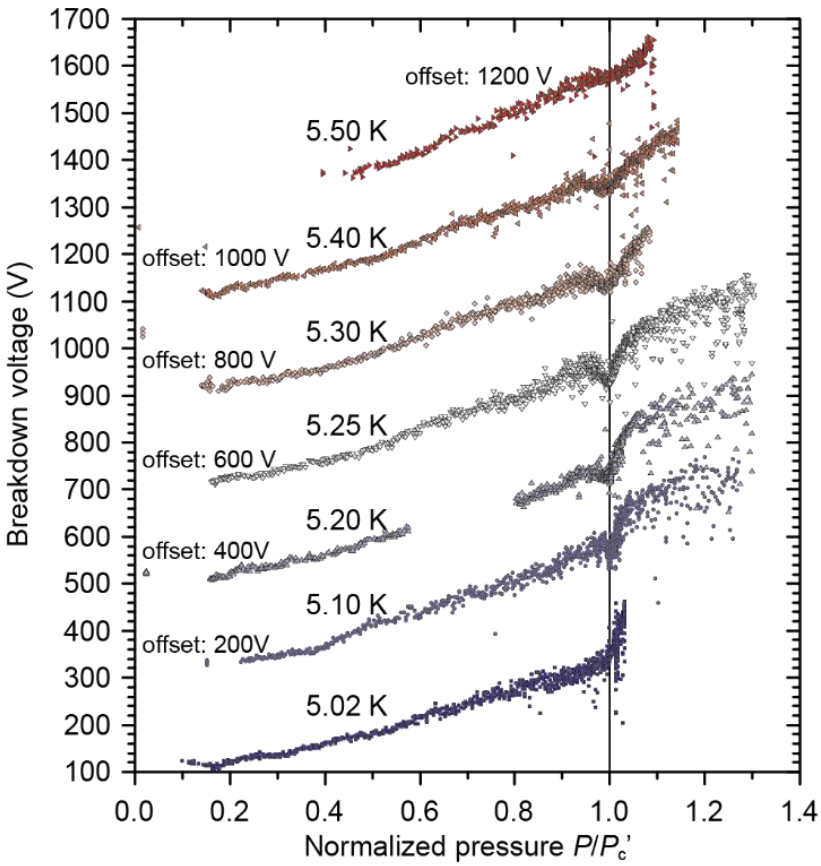

Figure 3.15 The experimental results of various temperatures in this study. The horizontal axis is normalized pressure which is the pressure normalized by the pressure on the Widom line (P_c') depending on the temperature. The lack of the measured U_B at 5.20 K from around $P/P_c' = 0.6 - 0.8$ were caused by technical problem of our experimental system.

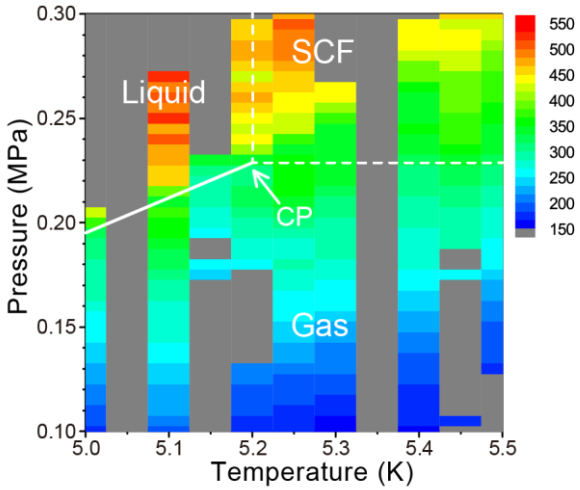

Figure 3.16 Color plot of the measured U_B on temperature-pressure phase diagram of He. The reddish colors indicate high U_B. The cells size is 0.5 K and 5 kPa. The value of U_B in each cell was an averaged value of all U_B measured at the condition within the cell. The gray cell indicates that there is no measured point in the cell.

A large number of U_B data points (800 – 1200 for each temperature) were measured in this study. This number was more than 10 times larger than that in the previous studies. Moreover, since the experiments were conducted without replacing the electrodes in this study, the variation in U_B was much less than that in the previous study. These enabled us to conduct discussions by fitting of the estimated breakdown voltages from discharge models to the experimental results.

The values of U_B are plotted on the *T*-*P* phase diagram of He as a contour plot as shown in Figure 3.16. The value of U_B in each cell whose size is 0.5 K and 5 kPa in Figure 3.16 was an averaged value of all U_B satisfying that the condition where the value was measured was within the cell.

Figure 3.17 shows the reduced U_B as a function of density for each temperature. The measured U_B in this figure were normalized with respect to the average values in the range of 8.0 ± 0.05 mol L^{-1} in order to compare their dependencies on *n* more clearly. In the case of $T = 5.10$ K, there was a jump in U_B due to the gas-liquid phase change. Up to approximately $n = 11$ mol L^{-1}, the values of U_B were independent of *T*. However, for $n > 11$ mol L^{-1}, the values of U_B were dependent on *T*. If we choose any density below 11 mol L^{-1} instead of 8 mol L^{-1} in the normalizing operation, then the transition is also observed around 11 mol L^{-1}. These dependences on both *n* and *T* except the critical anomaly resemble those of He breakdown in 1 mm gap [22].

For the horizontal axis, *n* is a more important parameter than *P* for electric discharges in the gas phase, especially when discussing the change in temperature or discussing phenomena at high isothermal compressibility conditions near the phase transition line including the Widom line. Meanwhile, the critical anomaly of U_B becomes more apparent when *P* is plotted on the *x*-axis. Therefore, *P* or *n* was selected as x-axis depends on what was intended to be emphasized

in the graph.

In following, the electrical breakdown models to explain these experimental results are proposed and the results of the model simulation are discussed.

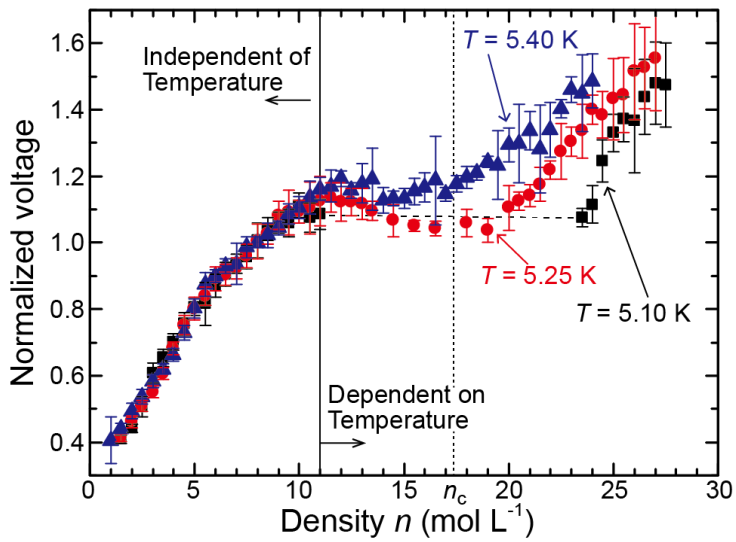

Figure 3.17 Normalized breakdown voltages as a function of helium density measured at 5.10 K (black squares), 5.25 K (red circles), and 5.40 K (blue triangles). The breakdown voltages are normalized with respect to the measured voltages at an average density of 8.0 ± 0.05 mol L^{-1}. The error bars correspond to standard deviations. In the case of T = 5.10 K, there is a jump in density due to the gas-liquid phase change.

3.3 Bubble model

3.3.1 Model description

We analyzed the results by employing a quantitative analytical model of the breakdown voltages. In this model, we assume that the breakdown mechanisms change from gas-like to liquid-like at the threshold number density (n_{th}). We also assume that the gas-like breakdown mechanisms follow the general Townsend theory, and that the liquid-like breakdown can be modeled by a discharge forming a vapor bubble [22,32]. The vapor bubble around an electron in liquid He, which is called an "electronic bubble", is basically due to the negative electron affinity of liquid He and this is a kind of a quantum effect. In this model, since a detailed assessment of the nature of the bubbles in liquid-like SCF and on the electron motion in the bubble was complicated, it was assumed that the local electrical breakdown occurred in each bubble caused the whole electrical breakdown and the electron motion in the bubble was similar to that in a normal gas. Since the role of the density fluctuation in the electron bubble was unclear, the power law of F_{D}, which was introduced in section 3.1.4.3, was used in both gas and liquid phases. The breakdown voltage based on these two mechanisms, U_{N}, can be expressed as

$$U_{\mathrm{N}} = \begin{cases} U_{\mathrm{G}} & (n \leq n_{\mathrm{th}}) \\ U_{\mathrm{L}} & (n > n_{\mathrm{th}}) \end{cases}, \tag{3. 19}$$

$$U_{\mathrm{G}} = \frac{\Phi}{AB}\frac{d}{\lambda}\left(\ln\left(\frac{d}{\lambda}\right) - \ln\left(\ln\left(\frac{1}{\gamma}+1\right)\right)\right)^{-1}, \tag{3. 20}$$

$$U_{\mathrm{L}} = C_1 d \times \left\{\frac{1}{\varepsilon_0 \varepsilon_{\mathrm{r}}}\left(P + \frac{2s_{\mathrm{b}}}{r_{\mathrm{b}}}\right)\right\}^{1/2}. \tag{3. 21}$$

Here, U_{G} is the breakdown voltage based on the Townsend theory, d is the gap length, λ is the mean free path of electrons, Φ is the ionization potential, γ is the secondary Townsend coefficient, A is the coefficient related to the electrode geometry, and B is the coefficient associated with Lorentz's internal field [equation (3. 18)]. U_{L} is the breakdown voltage based on the bubble model [22,32], C_1 is a fitting coefficient, ε_0 is the vacuum permittivity, and s_{b} and r_{b} are the surface tension and the radius of the "bubble", respectively. We employed $r_{\mathrm{b}} = 5$ nm, which is a typical radius of a bubble generated due to the negative electron affinity in liquid He [22], and it was found that U_{L} did not change substantially for $r_{\mathrm{b}} > 0.1$ nm. λ was calculated using the kinetic theory of gases and can be expressed by $\lambda = (n \times \sigma)^{-1}$, where σ is the electron-particle cross section. Here, $\sigma = 2 \times 10^{-21}$ m^{-2} was employed and this value approximately corresponds to the typical value of electron-impact ionization cross section in He [34].

Concerning the critical anomaly of U_{B}, a power law depending on F_{D} was suggested [140–142]:

$$U_{\mathrm{B}} = U_{\mathrm{N}} F_{\mathrm{D}}^{-C_2} \tag{3. 22}$$

where C_2 is a fitting coefficient, which expresses the effect of F_{D} in an electrical discharge. The parameters applied in this analysis are listed in Table 3.1 [133,150,189].

Table 3.1 Parameters used in the analysis of the breakdown voltage in Bubble model.

		Value	Ref.
Threshold number density (mol L^{-1})	n_{th}	10.9	-
Gap distance (μm)	d	3.4	-
Ionization potential (eV)	Φ	24.6	-
Coefficient related to electrode	A	0.735	-
Secondary Townsend coefficient	γ	0.3	[150]
Radius of bubble (nm)	r_b	5	[133]
Surface tension (mN m^{-1})	s_b	$0.809\{(T_c - T)/T_c\}^{1.306}$	[189]
Constant	C_1	0.459	-
Constant	C_2	−0.09	-

3.3.2 Discussions

Figure 3.18 shows the comparison between experimentally measured U_B and calculated U_B curves. The experimental results were well reproduced by the calculated U_B curves. This strongly supports the validity of the model expressing the gas-like [Equation (3. 20)] and liquid-like [Equation (3. 21)] breakdowns and the power law of F_D [Equation (3. 22)]. Compared with previous studies, the high accuracy of the fitting is considered to result from the large number of experimental data points. It is also suggested that the transition in the breakdown mechanisms occurs at n_{th} = 10.9 mol L^{-1}, which is lower than n_c. The transition between T-independent and T-dependent behavior of the breakdown voltages in Figure 3.17 can be considered to be due to the difference of whether the electrical breakdowns were occurred by the gas-like or the liquid-like breakdown mechanisms. In gas-like breakdowns, U_B depend on n (in λ), whereas in liquid-like breakdowns they depend on P, not n. Therefore, the density that marks the transition between gas-like and liquid-like breakdowns should be in good agreement with the transition density between T-independent and T-dependent behavior shown in Figure 3.17. In the bubble model, bubbles are formed by local heating due to the applied electric field [32]. In contrast, near the CP, no energy may be required for bubble formation, because low-density regions, which are intrinsic in the structure of density-fluctuating fluids, may act as bubbles. Therefore, we conclude that the U_B near the CP becomes relatively low due to such intrinsic bubbles.

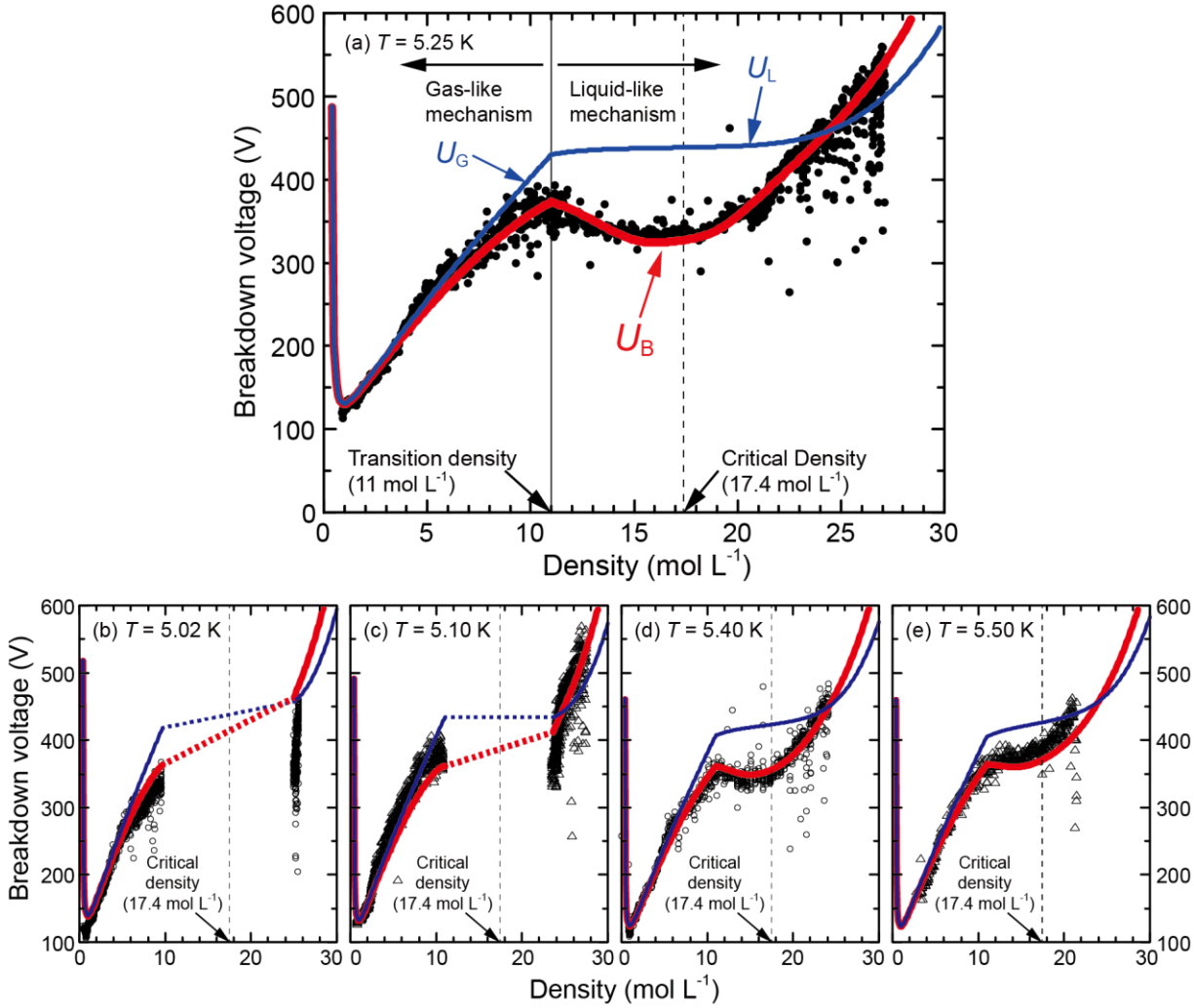

Figure 3.18 Experimental breakdown voltages (black symbols) and calculated breakdown voltages not taking into account the density fluctuation U_G and U_L (blue thin lines), and breakdown voltage U_B considering density fluctuation (red thick lines) at T = (a) 5.25 K, (b) 5.02 K, (c) 5.10 K, (d) 5.40 K, and (e) 5.50 K. The full and dotted vertical lines indicate the densities where the transition in the breakdown voltage occurs (n_{th}) and the critical density of He (n_c), respectively.

The discussion shows that the experimental results can be reproduced by the extension of the method proposed in the previous study to liquid phase. However, it is still not easy to find the physical meaning of the power law of F_D. Therefore, the further improvements of the discharge models extended from both gas and liquid phases are necessary for clarifying the effect of the density fluctuations. While the improved discharge model for gas and gas-like SCF are discussed following sections, an approach using numerical modeling considering the interaction between He atoms are probably necessary to further improve the discharge model for liquid and liquid-like SCF and to clarify the influence of quantum effect on the electrical breakdown.

3.4 Hard sphere cluster model

3.4.1 Model description

In order to investigate how the local structure of the density-fluctuating fluid affects the breakdown, we propose the concept of an effective electron mean free path (λ_{fluc}) for electrical breakdown in intrinsic bubbles, which takes into account the effect of the local structure of the fluid. λ_{fluc} can be estimated as follows.

We assume that clusters generated as a result of F_{D} can be approximated by an artificial, single large atom, which can be ionized by electron impact without dissociation, and that electrons can move in the interspace between clusters. In this model, the average radius of the clusters (r_{clu}) is also assumed to be approximately proportional to ξ and then indicated as

$$r_{\mathrm{clu}} = C_3\xi, \tag{3. 23}$$

where C_3 is a constant.

Although this model might be too simple to capture detailed discharge phenomena, it allows us to obtain important information on the discharge behavior in fluctuating fluids.

The third step is the calculation of λ_{fluc} with the above assumptions. The cluster cross section (σ_{clu}) can be estimated as

$$\sigma_{\mathrm{clu}} = \pi {r_{\mathrm{clu}}}^2 = \pi(C_3\xi)^2, \tag{3. 24}$$

Then, the average number of atoms contained in a cluster (Z_{clu}), which is necessary to estimate the cluster number density (n_{clu}), can be estimated as

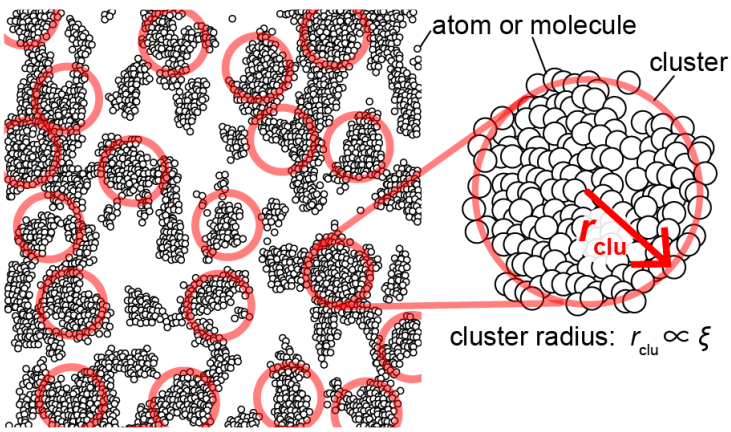

Figure 3.19 Schematic of the fluid structure with the assumption of "super" atoms (red circles), and the magnified view of a "super" atom with the indication of its radius (r_{clu}).

$$Z_{\mathrm{clu}} = \frac{A_{\mathrm{PF}} \cdot \frac{4}{3}\pi {r_{\mathrm{clu}}}^3}{\frac{4}{3}\pi {r_{\mathrm{p}}}^3} = A_{\mathrm{PF}} \left(\frac{C_3 \xi}{r_{\mathrm{p}}}\right)^3, \tag{3. 25}$$

where A_{PF} is an atomic packing factor, i.e. the fraction of volume of the cluster occupied by the atoms in the cluster, and r_{p} is the radius of a He atom. A_{PF} can be treated as a constant because the cluster structures are almost independent of their density [37]. Since it is assumed that all atoms are used to form clusters and there are only clusters in the fluid, n_{clu} is expressed as

$$n_{clu} = \frac{n}{Z_{clu}} = \frac{n}{A_{PF}} \left(\frac{r_p}{C_3 \xi}\right)^3. \tag{3. 26}$$

Finally, by Equations (3. 24), (3. 26), and (3. 3), λ_{fluc} can be expressed as a function of σ_{clu}, n_{clu}, and ξ:

$$\lambda_{\mathrm{fluc}} = (\sigma_{\mathrm{clu}} n_{\mathrm{clu}})^{-1} = \frac{A_{\mathrm{PF}} C_3 \xi}{\pi n r_{\mathrm{p}}^3} = \frac{A_{\mathrm{PF}} C_3 R' {F_{\mathrm{D}}}^{0.5}}{\pi n r_{\mathrm{p}}^3} \propto \frac{{F_{\mathrm{D}}}^{0.5}}{n}. \tag{3. 27}$$

3.4.2 Discussion

The variation of $F_{\mathrm{D}}^{0.5} / n$, which is proportional to λ_{fluc}, is shown in Figure 3.20. A negative correlation between the calculated λ_{fluc} and the measured breakdown voltages can clearly be seen. The correlation was confirmed at other temperatures. This strong correlation implies that λ_{fluc} is one of the key parameter to describe the electrical breakdown in the density-fluctuating fluids. In other words, it is suggested that F_{D} affects the discharge by modifying the electron mean free path λ_{fluc} due to a change of the correlation length ξ. Although this model approximates the fluid structure as gas-like structure in which there is no interaction between clusters, the negative correlation between λ_{fluc} and U_{B} is confirmed also in liquid and liquid-like SCF. This implies the possibility that the variation of U_{B} can be estimated from an evaluation of λ_{fluc} in liquid and liquid-like SCF.

In this model, the concept to estimate λ_{fluc} was proposed. However, since the method in this model to approximate the fluid structure having density fluctuation was too simple, the measured values of U_{B} could not reproduced reasonably. Therefore, a more precise model to estimate λ_{fluc} is necessary to clarify the electron motion in density-fluctuating fluids.

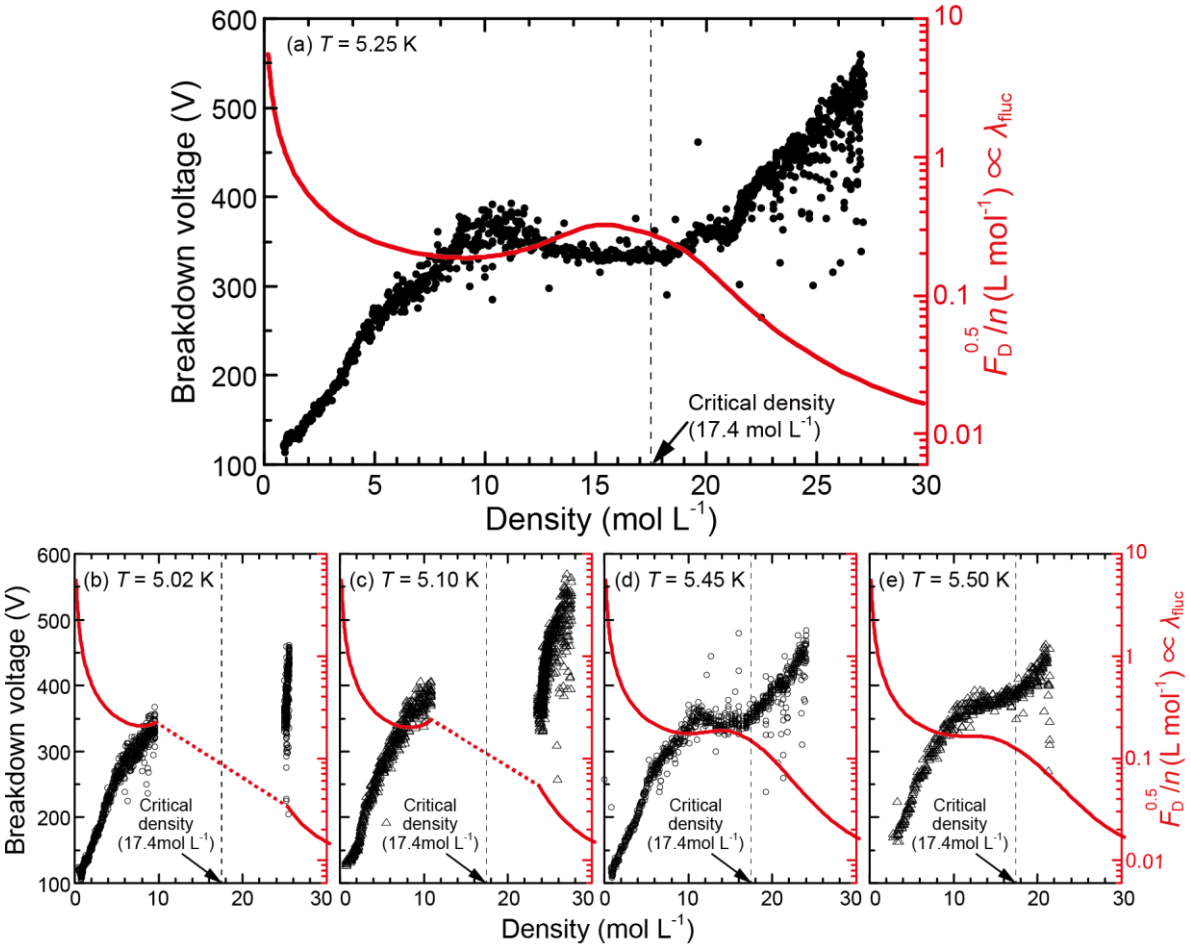

Figure 3.20 Measured breakdown voltages (black open symbols) and $F_D^{0.5}/n$, which is proportional to the electron mean free path assuming a cluster containing fluid λ_{fluc} [see equation (3. 27), red lines] as a function of helium density at temperatures of (a) 5.25 K, (b) 5.02 K, (c) 5.10 K, (d) 5.40 K, and (e) 5.50 K.

3.5 Local voids model

3.5.1 Model description

In general, an SCF has intermediate properties between a gas and a liquid, and can be divided into two regions by the so-called Widom line [100], which represents the local maxima of the density fluctuations F_D in the SCF state extending from the gas-liquid coexistence curve [98]: gas-like and liquid-like SCFs. Therefore, there are three approaches to discussing the properties and phenomena in an SCF: expanding existing theories from the gaseous phase (perhaps with some modifications), expanding those from the liquid phase (with modifications), or developing an original theory for SCFs. In this section, we adopted the first approach and we propose a model based on the conventional Townsend discharge model.

On this basis, we modified α due to the density fluctuations and γ due to the IEFE. We consider that the electrical discharges in the experiments in this study and in our previous study [144] were not corona- or streamer-like discharges because the gap distances were too short, the surfaces of the electrodes were too smooth, and the applied voltages were too small for such discharge modes to occur. In addition, while the breakdown voltages in liquid and liquid-like SCF regions were reported to be independent of the pressure in negative corona discharges [134,191], our experiments indicated the dependence of U_B on the pressure as shown in section 3.2.2. In the following, the effect of density fluctuations on α is discussed in section 3.5.1.1, and then supplementary information for the modification of γ in the mathematical expression for the modified Paschen's curve, which is introduced in section 3.1.4.2, is discussed in section 3.5.1.2.

3.5.1.1 Modification of α due to density fluctuations

We introduce the effect of density fluctuations on electron motion in the space between electrodes and the consequent change in α. In our model, other significant effects of the density fluctuations are not included, such as the low ionization potential of cluster species, the generation of cluster ions, and the change in ion mobility due to clustering. Also, the disturbance due to plasma-induced heating is not included because it can be assumed that the electrical breakdown occurs before the heating becomes dominant.

Figure 3.21 schematically illustrates the microscopic arrangements of fluid particles in domains with large and small volumes. The number of particles inside a given volume (indicated as a circle in the Figure 3.21) heavily fluctuates spatially and temporally when the volume is comparable to the characteristic volume of the fluctuation. The main characteristic of our model is that it includes this nature of the density fluctuations. The relationship between the standard deviation (n_s) of the local number density (n_L) and the average number density (n_{ave}, which is identical to n in previous sections) can be expressed using a nondimensional parameter F_D as [108]

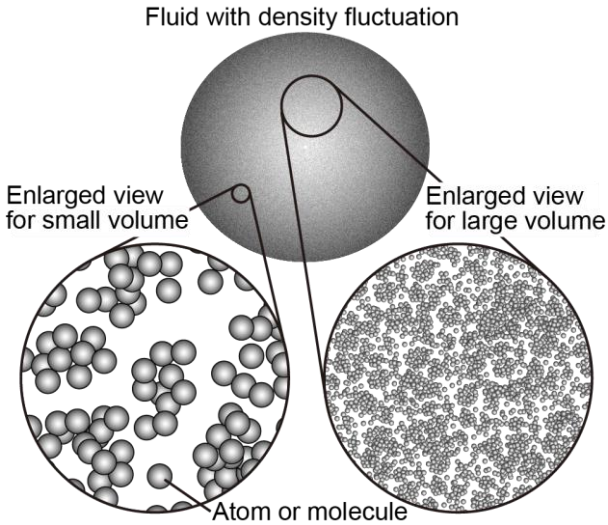

Figure 3.21 Schematic of microscopic arrangements of fluid particles subjected to density fluctuations in domains with large and small volumes. The fluctuation of the local number density in a given volume is emphasized when the volume is small.

$$\frac{n_s}{n_{ave}} = \sqrt{\frac{F_D}{n_{ave}V}} \tag{3. 28}$$

where

$$F_D \equiv \frac{\langle (N - \langle N \rangle)^2 \rangle}{\langle N \rangle} = \frac{(n_s V)^2}{n_{ave}V} = \frac{k_T}{k_T^0} \tag{3. 29}$$

with $\langle X \rangle$ indicates the average of X, N the number of molecules in a given volume V, k_T the isothermal compressibility, and k_T^0 the value of k_T for an ideal gas. Since k_T can be calculated from thermophysical databases, such as REFPROP [26], F_D can also be derived similarly to other thermophysical properties. Note that a larger F_D means larger density fluctuations and $F_D = 1$ in an ideal gas under any condition, which follows from the definition of F_D. Equation (3. 28) indicates that n_s does not only depend on F_D and n_{ave} but also depends on V. In other words, n_s varies with V even under the same thermophysical conditions. This means that to discuss the effect of the density fluctuations on a specific phenomenon, we must evaluate the characteristic volume related to the phenomenon.

Our discharge model assumes that the electrical breakdown initiates in a locally low-density spatial domain caused by the density fluctuations. Figure 3.22 schematically illustrates the microscopic structure of fluid particles with a random distribution under conditions where the density fluctuations are negligible [Figure 3.22 (a)] and large [Figure 3.22 (b)]. An electron is accelerated by the applied electric field and collides with fluid particles inside the cylindrical volume along the electron path from the cathode to the anode. Figure 3.22 implies that an increase in F_D leads to an increase in the width of the distribution of the mean free path of the electron (λ) even at the same density and, as a result, λ can be larger in a local region of low density.

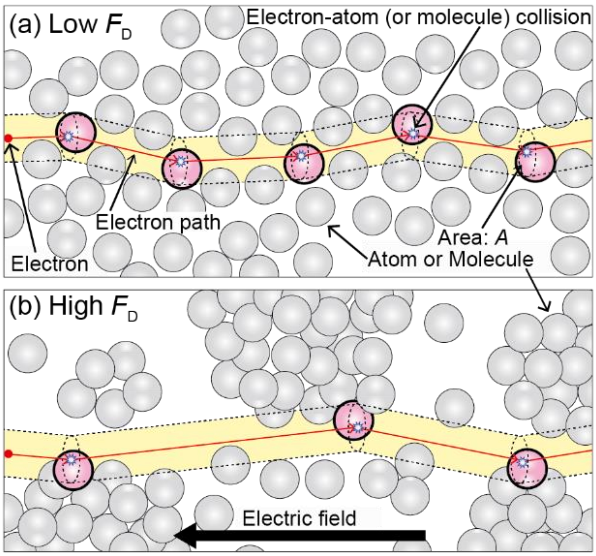

Figure 3.22 Schematic microscopic view of the cylindrical spatial domain along an electron path with a particle distribution and electron acceleration in (a) an ordinary gaseous fluid with low density fluctuations F_D, (b) a fluid with large density fluctuations (molecular clustering). An electron is accelerated by the applied electric field and collides with atoms or molecules whose centers are within the cylinder. The cross section of the cylinder is assumed to be the total collision cross section. The gray circles with thin circumferences indicate gas atoms or molecules and the circles with thick circumferences indicate atoms or molecules that collide with the electron.

On the basis of this assumption, we discuss α. We also assume that α/n can be expressed as a function of the reduced electric field (E/n), as is the case for a normal gas discharge. An expression for α/n can be obtained by solving the Boltzmann equation for an electron with employing cross section databases or by the literature (for example, Ref. [150]) as an empirical expression (often using P instead of n, although P can only be used when the experimental conditions ensure proportionality between P and n):

$$\frac{\alpha}{n} = \mathrm{A}\exp\left[-\mathrm{B}\left(\frac{E}{n}\right)^{-1}\right] \tag{3. 30}$$

where A and B are constants. In the following, we discuss the effect of density fluctuations on the reduced electric field E/n.

Concerning E, a homogeneous electric field is assumed in this study, because there are only few charged particles between the electrodes before breakdown occurs and the geometry of the electrodes could be approximated as a plane-to-plane geometry as described in section 3.2.1. Under this assumption, E is expressed as

$$E = \frac{U}{d} \tag{3. 31}$$

where U is the amplitude of the voltage between the electrodes and U should be U_B at the breakdown condition.

In the evaluation of n, the density of the local low-density spatial domain where the discharge occurs should be used in the estimation of α. Therefore, estimating the actual n_L where the discharge occurs is essential for calculating α. The effect of the density fluctuations on the value of n_L is discussed in the following.

Because of the density fluctuations, n_L at any given time and position has a distribution. Therefore, n_L can be expressed using n_{ave} and n_s as follows:

$$n_L = n_{ave} + xn_s = n_{ave}(1 + xn_s/n_{ave}) \tag{3. 32}$$

where x is a parameter indicating the magnitude of the deviation from the average number density. The value of n_{ave} can be estimated from T and P using thermophysical databases such as REFPROP [26].

Figure 3.23 shows the distribution function of the local number density n under the assumption of a Gaussian distribution and the relationship between n_{ave}, n_s, n_L, and x. The value of x should be negative because n_L should be less than n_{ave} where breakdown occurs. In the present model, x is assumed to be constant for all conditions. This means that the proportion of the volume of the locally low-density spatial domain where breakdown can occur to the total volume between electrodes is constant, even if the conditions change. For example, if $x = -1$ when breakdown occurs and the distribution function of n_L is assumed to be Gaussian, then about 16% of the total volume must contribute to the electrical breakdown. Similarly, if $x = -2$, then about 2.2% of the total volume must contribute to the initial breakdown. In the calculation, we treat x as a fitting parameter because we currently do not know how to obtain an analytical estimate of x. When F_D reaches a high level, i.e., at conditions near the CP, n_L is lower because n_s is higher and x is constant. Note that the skewness of the local number density distribution is not zero for a gas, liquid, or SCF, except for conditions corresponding to the Widom line [192], in other words, the distribution is not symmetric with respect to the average number density for almost all conditions. Therefore, the above percentages are only approximate values.

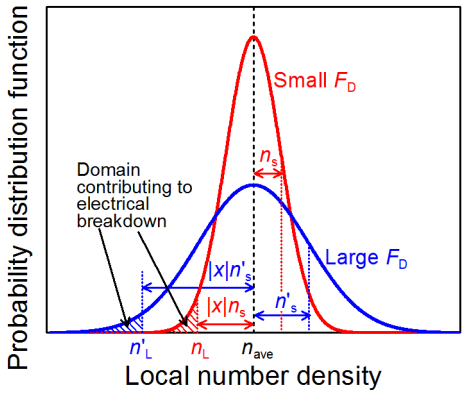

Figure 3.23 Schematic of the probability distribution function of the local number density with small and large density fluctuations F_D assuming that the probability distribution function is Gaussian. The relationship between the average number density n_{ave}, the standard deviation n_s (n'_s for a large F_D), the local number density in the cylindrical domain n_L (n'_L for a large F_D), and the parameter indicating the magnitude of the deviation from the average number density x is illustrated. For a large F_D, n'_L is lower than n_L at the same x. Domains with density lower than n_L (or n'_L) contribute to the electrical breakdown (shaded area). Note that the actual distribution of the local number density is not Gaussian and the skewness is not zero for almost all conditions.

As expressed by Equation (3. 28), n_s is related to both F_D and V. To evaluate V, we consider a local cylindrical spatial domain along the path of an electron that accelerates from the cathode to the anode (Figure 3.24). Although the length of the cylinder (L) should exceed d because the direction of electron motion varies after each collision with a gas species, for simplicity, we assume that $L \approx d$. In high-pressure gases, since an electron does not gain sufficient energy for each collision to be inelastic, and because the electron is accelerated by repeated elastic collisions, the value of λ is important. When λ is small, the electron cannot easily gain sufficient energy between collisions. On the other hand, electrons can be accelerated efficiently for large λ. Therefore, to take into account collisions between all electron and gas species, including elastic and inelastic collisions, the cross section of the cylindrical spatial domain (A) is assumed to be the total collision cross section between the electron and gas species (σ). σ can be expressed as a function of the electron temperature (T_e). Under these assumptions, the volume of the cylinder (V) can be written as

$$V = AL = \sigma d. \tag{3. 33}$$

From Equations (3. 28) and (3. 31) – (3. 33), the effective reduced electric field in a locally low-density domain E/n_L can be expressed as

$$\frac{E}{n_L} = \frac{U/d}{n_{ave}\left[1 + x\sqrt{F_D/(n_{ave}\sigma d)}\right]}. \tag{3. 34}$$

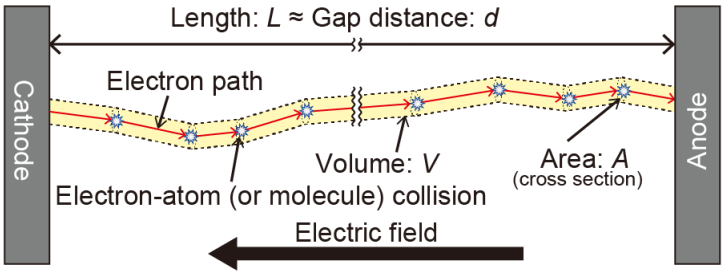

Figure 3.24 Schematic of cylindrical spatial domain along electron path between electrodes assumed in our model. As an electron travels from the cathode to the anode, it changes direction upon elastic and inelastic collisions with gas atoms or molecules in the high-density fluid (electron path). In our model, we assume that the length of the cylindrical spatial domain (yellow part along electron path) L is almost identical to the gap distance d.

By determining the parameters related to the gas species (σ) and the experimental conditions (U, d, n_{ave}, and F_D) and by treating x as a fitting parameter, we can estimate the effective reduced field E/n_L. Then, we can estimate α from E/n_L by solving Boltzmann's equation or Equation (3. 30). The values of the parameters used in this study are given in section 3.5.2.

3.5.1.2 Modification of γ due to ion-enhanced field emission

The modification of γ in the mathematical formulation of the modified Paschen's curve was introduced in section 3.1.4.2 [153,158,159]. Originally, the modified Paschen's curve was for a low $P \times d$ region (left branch of Paschen's curve). This work is the first to apply it to the deviation of U_B in the right branch of Paschen's curve under high-pressure conditions. The reason why the model includes the modification of γ due to IEFE is to account for the effect of the high-density conditions on electrical discharges. As another effect of the high-density conditions, while the variation of the ion mobility (μ) depending on n is included in our model (see section 3.5.2), other major disturbances related to electrical discharges due to the high-density conditions and condensation, such as the change of collisional cross sections due to clustering, are not included.

3.5.2 Calculation condition

To calculate U_B in our model, the properties (expressed by α, ϕ, γ_i, σ, and μ) should be determined. As mentioned in section 3.5.1.1, α/n_L can be expressed as a function of E/n_L. This function was calculated by solving the Boltzmann equation using the Boltzmann equation solver BOLSIG+ [83] with a cross section database of He [84] under the assumption that the difference in the ionization potentials between an isolated atom and its cluster is negligible because clusters in an SCF near the CP are very unstable [125]. In the He-W system, the work function ϕ and the secondary

emission constant γ_i can be assumed to be 4.54 eV and 0.21, respectively [150]. We adopted the electron-atom impact (total) cross section of He [193] for σ, which is expressed as a function of the electron temperature (T_e). T_e was calculated as a function of E/n_L by BOLSIG+. Since the total cross section σ was only measured for T_e below 20 eV in the reference data [193], we conducted the calculation for values of T_e below 20 eV and all calculated data (shown in Figs. 5 – 11) satisfied $T_e < 20$ eV. Although the energy of electrons varies as they move along the path from the cathode to the anode, we did not take into account this temporal and spatial variation of energy and we used the average T_e value.

For the calculation of γ' from equations (3. 12) – (3. 15), the parameter β and the electron mobility μ should be determined.

Concerning β, field emission is known to be strongly affected by small protrusions on the surface, modeled by the factor β, and β can be estimated from the Fowler-Nordheim plot [168]. Hoewver, β was not evaluated by the Fowler-nordheim plot in our experiments because of difficulties related to our experimental setup. The value of β has been reported to be at least 15 despite the use of carefully prepared surfaces [168] and, for example, a value of about 55 was used in investigations on the deviation of U_B from Paschen's curve in atmospheric-pressure micrometer discharges without considering the microscopic surface condition [158,159,194]. Therefore, in this study, β is used as a fitting parameter in our calculation.

The ion mobility μ can be expressed using the reduced mobility μ_0 as

$$\mu = \mu_0 n_0 / n_L \tag{3. 35}$$

where n_0 is the number density of the gas at standard temperature (T = 273.15 K) and pressure (P = 101.325 kPa). The value of μ_0 was estimated using the effective reduced electric field E_A/n_L:

$$\mu_0 = 5.06 \times 10^{-3} \times \left(\frac{E_A}{n_L}\right)^{-0.4} \tag{3. 36}$$

which is the fitted expression of the values for He^+ in He at 5 K [68]. The units of μ_0 and E_A/n_L in Equation (3. 36) are $m^2\ V^{-1}\ s^{-1}$ and Td (= 10^{-21} V m^2), respectively. Since the difference of μ_0 between 5 and 6 K at E/n > 6 Td is sufficiently small (< 2%) and the temperatures in our experiments were within this range, we used the values at 5 K in this paper. The error of μ_0 calculated by Equation (3. 36) relative to the values in Ref. [68] are within 1% for an electric field between 10 and 26 Td. All values of E/n_L in our calculation were >10 Td. Although there were no available data above 26 Td in Ref. [68], we used extrapolated values calculated by Equation (3. 36).

3.5.3 Comparison of model calculations with experiments in He

First, we evaluated the fitting parameter β by ignoring the effect of the density fluctuations. In the calculation, we set $F_D = 1$, which is the value for an ideal gas and similar to that for helium except near the critical point, and $x = -3$, which is the most appropriate value as will be discussed later. A large value of β indicates a large concentration of the

electric field in the vicinity of protrusions on the cathode. The calculated U_B and the experimental results at 5.30 K are shown in Figure 3.25 as functions of P [Figure 3.25 (a)] and n_{ave} [Figure 3.25 (b)]. The calculated and measured values of U_B in Figure 3.25 (a) and (b) were the same. For the horizontal axis, n_{ave} is a more important parameter than P for electric discharges in the gas phase (especially when the experimental conditions do not ensure proportionality between P and n), while the critical anomaly of U_B becomes more apparent when P is plotted on the x-axis. Therefore, we show graphs plotted against both P and n_{ave} in the evaluation of the fitting parameters (Figure 3.25 and Figure 3.26). After that, we show the values of U_B and other parameters only as a function of P (Figure 3.28 – Figure 3.32). Figure 3.25 shows that the deviation of U_B from Paschen's curve starts at a lower pressure (density) at higher β and that β between 20 and 30 appears to be the most appropriate value for our experiments. This value is reasonable for IEFE as mentioned in section 3.5.2. Actually, we adopted $\beta = 22$ because the most accurate calculation results were obtained with this value, as discussed in the following.

Next, the evaluation of the other fitting parameter x was conducted. The parameter F_D corresponding to the given thermophysical conditions was included in this calculation, with β set to 22. The calculation results at 5.30 K as functions of P and n_{ave} are shown in Figure 3.26 (a) and Figure 3.26(b), respectively, where the indicated experimental results are the same as those in Figure 3.25. Figure 3.26 shows that the U_B calculated by our model is in good agreement with the experimental results. The modification of U_B due to the density fluctuations was strongly emphasized near the pressure (density) on the Widom line and U_B has a local minimum when x is less than −2. As mentioned in the introduction, since our electrical breakdown model is based on the electrical breakdown model for the gas phase, the breakdown model starts to deviate from the experimental results when the fluid state becomes a liquid-like SCF. The figure implies that $x \sim -3$ is the most appropriate value for this condition. A large absolute value of x indicates that the local volume n_L and the volume contributing to the initiation of the electrical breakdown are small. The value of −3 implies that the electron acceleration in 0.1% of the total volume, where the gas particle density is less than $n_{ave} - 3n_s$, contributes to the discharge ignition.

Figure 3.27(a) and (b) show the contour plots of the local decrease of U_B due to the density fluctuation and the value of F_D, respectively, on the phase diagram of He. The size of cells in Figure 3.27(a) are 0.5 K and 5 kPa. The local decrease of U_B was calculated by subtracting the calculated U_B values with $\beta = 22$ and $x = 0$ from the measured values in Figure 3.15. The conditions, where the absolute values of the decrease of U_B were high, were on a line corresponding to the Widom line on which F_D shows local maxima in isobaric line.

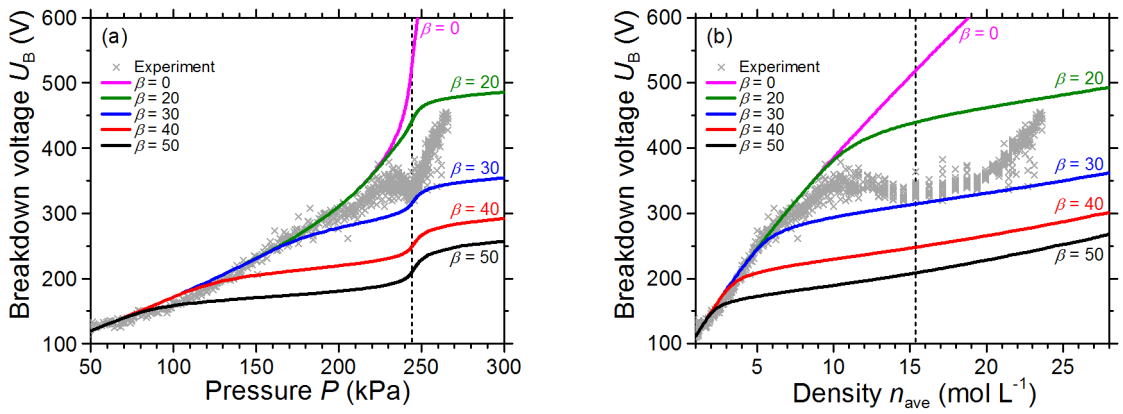

Figure 3.25 Variation of experimentally measured and numerically calculated U_B with β at T = 5.30 K (T/T_c = 1.02) as a function of (a) pressure P and (b) density n_{ave} for He. A large β indicates a strong concentration of the electric field in the vicinity of protrusions on the cathode. The parameter x was set at −3 and the vertical dashed lines indicate the pressure or density on the Widom line at T = 5.30 K. The gap distance d was set at 2.7 μm. An ideal gas (F_D = 1) was assumed in the estimation of β without taking density fluctuations into account. The curve at β = 0 corresponds to the classical Paschen's curve.

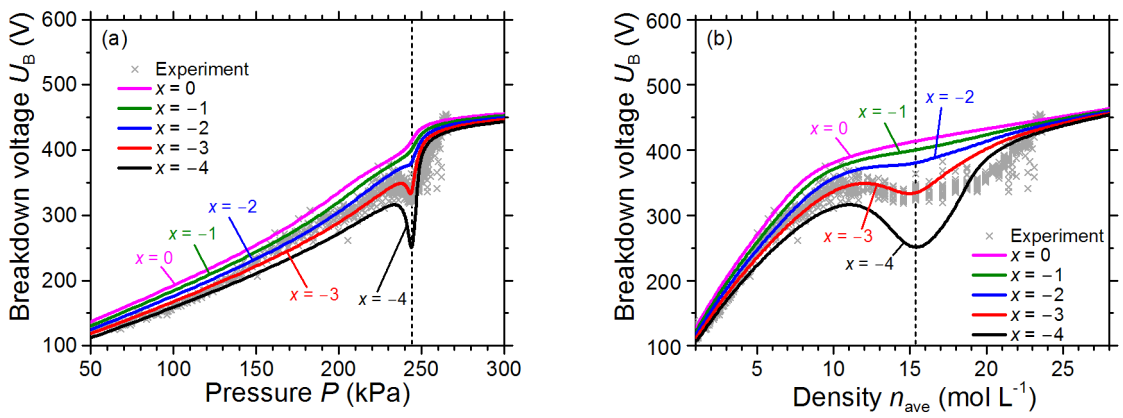

Figure 3.26 Variation of experimentally measured and numerically calculated U_B with different values of x at T = 5.30 K (T/T_c = 1.02) in He as a function of (a) pressure P and (b) density n_{ave}. A small x (a large absolute value of x) indicates that the local volume n_L and the volume contributing to the initiation of electrical breakdown are small. β was set at 22 and the vertical dashed lines indicate the pressure or density on the Widom line at T = 5.30 K. The gap distance d was set at 2.7 μm. The experimental results are the same as those in Figure 3.25.

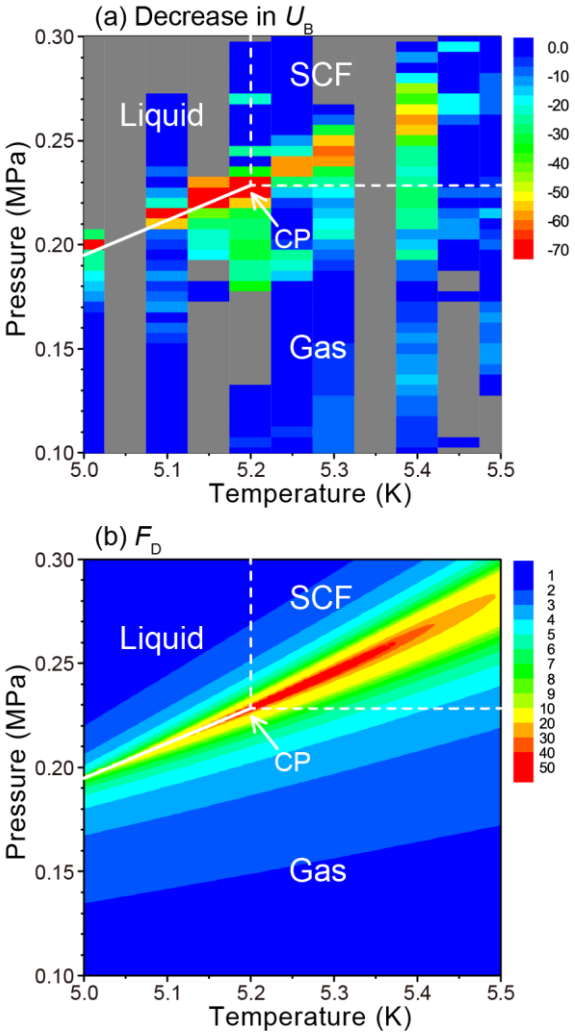

Figure 3.27 (a) The color plot of the decrease of U_B compared to the simulated U_B values from modified Paschen's curve considering the effect of the ion-enhanced field emission (IEFE) and not considering the effect of the density fluctuations. The cell size is 0.5 K and 5 kPa. The value of U_B decrease in each cell was an averaged value at the condition within the cell. The gray cell indicates that there is no measured point in the cell. Reddish colors indicate the absolute values of the decrease of U_B were high, which means that the effect of the density fluctuations were large. (b) The contour plot of F_D on the phase diagram of He. Reddish colors indicate high F_D.

By comparing the results obtained at different temperatures, the dependence of the validity of our model on the thermophysical conditions can be discussed. Figure 3.28 shows the calculation results and experimental results at (a) 5.25 K (T/T_c = 1.01) and (b) 5.50 K (T/T_c = 1.06). The experimental results at 5.25 K are the values reported in Ref. [144], and those at 5.50 K were obtained in this study. The four lines shown in each graph in Figure 3.28 are two fitting curves obtained by our model with x = −3 [line (A)] and −2.3 [line (B)], the modified Paschen's curve without

the effect of the density fluctuations [line (C)], and the conventional Paschen's curve [line (D)]. The parameters for each line are indicated in the legends in Figure 3.28. The calculation results in Figure 3.28 reproduce the critical anomaly of U_B, in common with Figure 3.26, and the critical anomaly is largest in the experimental results at 5.25 K, which is the value of T closest to T_c in this study. While Figure 3.26 and Figure 3.28 (b) show that the fitting curve with $x = -3$ exhibits good agreement, in Figure 3.28 (a), the fitting curve with $x = -2.3$ has better agreement than that with $x = -3$. These results imply that the effect of the density fluctuations on U_B in our model is slightly overestimated or underestimated, although our breakdown model allows us to qualitatively simulate the U_B values well. It is expected that a more quantitative discussion will be possible once a more sophisticated analytical model that includes other clustering effects in high-density gases, such as the changes in ionization potential and ion mobility, has been proposed. An electrical breakdown model for the condensed phase that takes into account the density fluctuations will also be necessary for a more quantitative discussion.

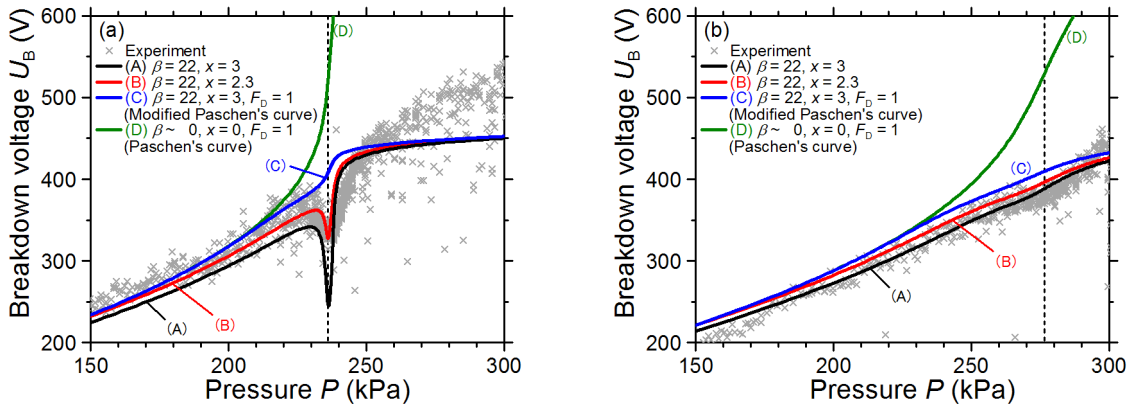

Figure 3.28 Experimentally measured and numerically calculated U_B as a function of P at (a) T = 5.25 K (T/T_c = 1.01) and (b) T = 5.50 K (T/T_c = 1.06) in He. The lines (A) and (B) indicate the results calculated by our model. The gap distance d was set at 2.7 μm. The line (C) is the modified Paschen's curve at β = 22 without taking into account the effect of the density fluctuations. The line (D) is the classical Paschen's curve. The vertical dashed lines indicate the pressures on the Widom line at T = 5.25 K in (a) and 5.50 K in (b).

3.5.4 Discussion on dependency on gap distance

We also calculated U_B using the breakdown model to investigate the dependence of the critical anomaly on d. Figure 3.29 shows the calculation results of U_B for gap distances d = 2, 3, 5, 7, and 10 μm at a fixed temperature of 5.30 K. We did not calculate U_B for d = 1 μm because T_e exceeds 20 eV near the CP. As shown in the figure, the local minimum of U_B near the CP becomes evident with decreasing d, and the local decrease can be observed when d is less than approximately 5 μm. This result is in good agreement with the tendency of U_B measurements in high-density

CO_2 near its CP with 1, 5, and 10 μm gap distances [142], and it is also consistent with the fact that no critical anomaly of U_B has been observed in studies with longer gap distances [133,134,136,178–181]. When d decreases, the volume of the locally low-density domain V at the breakdown decreases because of the smaller length L due to the assumption of $L \approx d$ in the breakdown model. As a result, n_s/n_{ave} increases when d decreases because n_s/n_{ave} is proportional to $V^{-0.5}$ [Equation (3. 28)]. In other words, as shown in Figure 3.21, the effect of the density fluctuations on electron motion increases when V decreases. Our model has successfully included this nature of the density fluctuations, which is why the effect of the density fluctuations on U_B becomes significant with decreasing gap distance d.

As shown in Figure 3.28 (b), the calculated values of U_B [lines (A) and (B)] are smaller than those obtained by the modified Paschen's curve [line (C)], even for conditions relatively far from the critical point where the value of F_D is similar to that of an ideal gas (for example, $F_D < 2$). In other words, the effect of the density fluctuations on U_B emerges even under conditions far from the CP. This is due to the presence of the term xn_s/n_{ave} in Equation (3. 32). In contrast, the effect of the density fluctuations on U_B was not included in previous electrical breakdown models such as the conventional Townsend model [182] and the models for the modified Paschen's curve [153–155], although density fluctuations exist even in an ideal gas where $F_D = 1$. This is because in electrical discharges with macroscopic gap distances, the magnitude of n_s/n_{ave} and its change as a function of pressure are negligible. This is shown in Figure 3.30, which displays the variation of n_s/n_{ave} for He as a function of pressure for gap distances between 1 μm and 1 mm, where the effect of the density fluctuations do not appear for gap distances larger than a few microns. Therefore, even if in principle, the effect of the density fluctuations should be included in gaseous electrical breakdown models, it can be ignored for macroscopic gap distances.

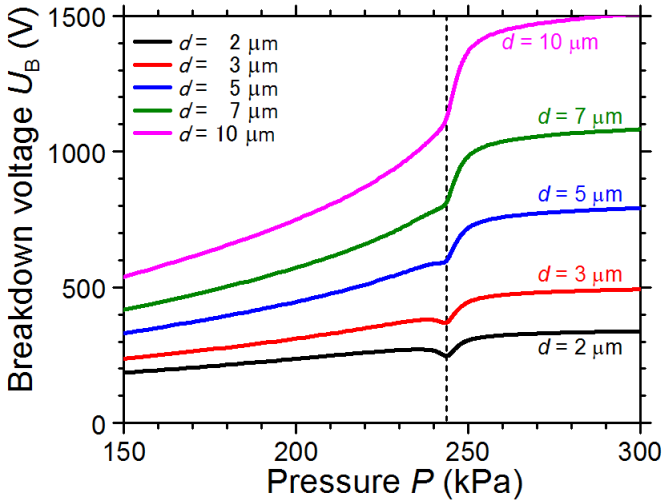

Figure 3.29 Calculated breakdown voltage U_B curves for different discharge gaps d as a function of He fluid pressure P. The temperature of the He fluid was fixed at 5.30 K and the fitting parameters β and x were 22 and −3, respectively, which were the best-fitted values in Figure 3.25 and Figure 3.26. The vertical dashed line indicates the pressure on the Widom line at T = 5.30 K. The local minimum of U_B near the pressure on the Widom line can be confirmed at $d \leq 5$ μm.

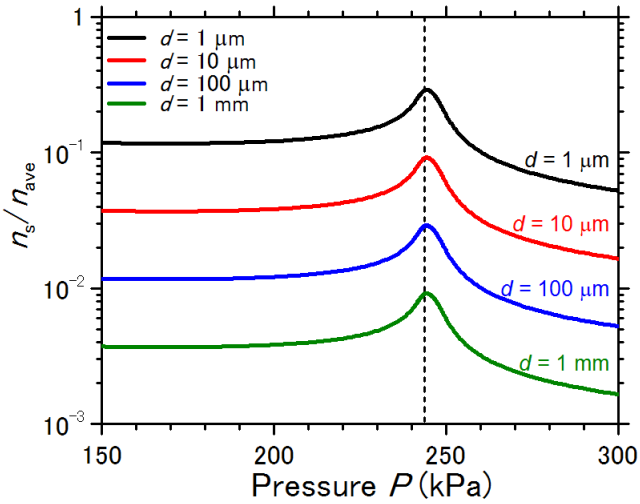

Figure 3.30 Ratio of the standard deviation n_s to the average number density n_{ave} for different gap distances d as a function of pressure P, calculated by Equation (3. 28). The temperature T, the cross section of a given volume A, and the parameter x were fixed at T = 5.30 K, $A = 5 \times 10^{-20}$ m^{-2}, and $x = -3$, respectively. Note that $x = -3$ was the best-fitted value in Figure 3.26. The vertical dashed line indicates the pressure on the Widom line at T = 5.30 K.

3.5.5 Discussion on the effects of density fluctuations on λ_{fluc}, α, and γ

To discuss the electron motion in fluids using our model, we calculated the effective mean free path of an electron in a cylindrical spatial domain λ_{fluc} that can be expressed as follows:

$$\lambda_{\mathrm{fluc}} = \frac{1}{n_L \sigma}. \tag{3. 37}$$

Figure 3.31 shows the dependence of λ_{fluc} on d near the CP when breakdown occurs. The value of λ_{fluc} has a local maximum near the CP, which is due to the low n_{L} at high F_{D}, and this tendency corresponds to the concept shown in Figure 3.22. Regarding the dependence of λ_{fluc} on d, both the value of λ_{fluc} and its increment near the CP are larger at smaller d. This is simply due to the dependence of n_{L} on d. Thus, the dependence of n_{L} on F_{D} is amplified with decreasing d.

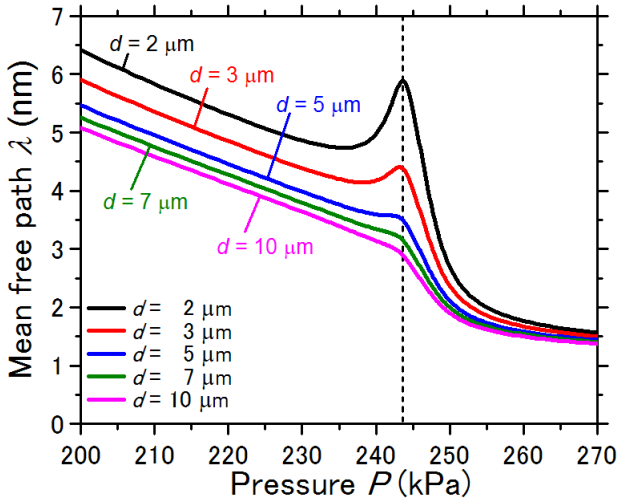

Figure 3.31 Calculated electron mean free path λ_{fluc} for different discharge gaps d as a function of He fluid pressure P when breakdown occurs. The temperature of the He fluid and the parameter x were fixed at 5.30 K and −3, respectively, where x = −3 was the best fitted value in Figure 3.26. The local maximum of λ_{fluc} near the pressure on the Widom line can be confirmed at $d \leq 5$ μm. The vertical dashed line indicates the pressure on the Widom line at T = 5.30 K.

In the following, the effects of the density fluctuations on the two coefficients α and γ in the discharge models are discussed. Figure 3.32(a) and (b) show the variation of the calculated values of α and γ' with different values of d as a function of P, respectively. The values in Figure 3.32 are calculated for T = 5.30 K at a constant electric field of E = 125 V μm^{-1}, which is similar to the value of E when breakdown occurs near the CP in this study. As indicated in Figure 3.32(a), the magnitude of α increases with decreasing d, and the value of α increases near the CP. Following

equation (3. 30), α can be expressed as the product of a linearly increasing component and a component that decreases exponentially with increasing n. Therefore, small values of n_L lead to large α. In other words, since electrons can easily be accelerated in the case of a large λ_{fluc} owing to the large F_D, α is larger near the CP. Thus, the density fluctuations affect α by changing λ_{fluc}.

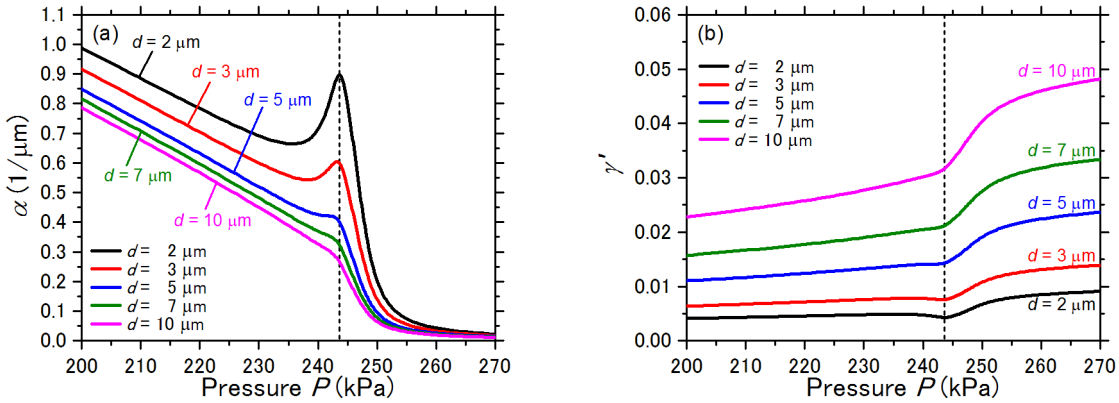

Figure 3.32 Calculated (a) first Townsend coefficient α and (b) secondary electron emission coefficient due to the IEFE γ', for different discharge gaps d as a function of He fluid pressure P at an electric field of E = 125 V μm^{-1}, which was similar to the value of E when breakdown occurs. The temperature of the He fluid was fixed at 5.30 K and the parameters β and x are 22 and −3, respectively, which were the best-fitted values in Figure 3.25 and Figure 3.26. The vertical dashed lines indicate the pressure on the Widom line at T = 5.30 K.

The value of γ' decreases with decreasing P, except for conditions near the CP and small values of d (<5 μm), as shown in Figure 3.32(b). This can be explained as follows: since the IEFE is a probabilistic event, the long residence time of positive ions near the cathode due to high-P condition leads to a decrease in the probability of IEFE. In other words, the decrease in the number density n due to decreasing P leads to a larger μ [Equations (3. 35) and (3. 36)], then the large μ causes a small K [Equation (3. 9)], and finally γ' decreases [Equation (3. 8)]. As shown in Figure 3.32(b), γ' increases with increasing d, and this is caused by the proportional relationships between γ' and K, and between K and d [Equations (3. 8) and (3. 9)]. Figure 3.32(b) also indicates that γ' decreases slightly near the CP. This means that the effect of IEFE on U_B is suppressed when it is coupled to the density fluctuations, and U_B would increase by the variation of γ' near the CP, if there would be no effect of the density fluctuations on α. The reason for this is proposed to be as follows. The decrease in the local number density n_L due to the density fluctuations leads to a higher μ, and the high μ causes a small γ', as derived from the same discussion as P-dependency of γ' (cf. the explanation further above). The magnitude of the decrease in γ' near the CP becomes smaller with increasing d, and this is also because the effect of the density fluctuations is enhanced in small volumes.

Next, we discuss the relation between the density fluctuations and the IEFE near the CP, which both affect U_B. As mentioned in above, while the variation of α near the CP in Figure 3.32(a) tends to raise U_B, that of γ near the CP in Figure 3.32(b) tends to drop U_B. However, the actual increase in U_B due to the decrease of γ' was not significant: the difference in U_B between the cases of considering and not considering the variation of γ' due to the density fluctuations was less than 0.5%. This is because the variation of γ' due to the density fluctuations was small and γ' is smaller than γ_i in this case. Moreover, as shown in Equation (3. 4), γ affects the Townsend criterion linearly, while α affects it exponentially. To summarize these points, a small n_L due to the density fluctuations leads to a larger α and smaller γ, but the variation of U_B near the CP is dominated by the effect of the variation of α owing to the density fluctuations, rather than γ.

3.5.6 Conclusion

We discussed two characteristics of electrical breakdown near the CP, i.e., the critical anomaly itself, evidenced by a local minimum, and its dependence on d. We developed an electrical breakdown model based on an extension of the gas discharge theory (Townsend theory) with modifications of α due to the density fluctuations and γ due to the IEFE. For the modification of α, we developed a model based on the concept that the breakdown occurs in a locally low-density spatial domain resulting from the density fluctuations. The results of the model suggested that increasing F_D leads to an increase in the effective mean free electron path λ_{fluc}, leading to an increase of the first Townsend coefficient α in locally low-density spatial domains. Consequently, the enhanced electron acceleration causes the critical anomaly of U_B. Moreover, we reproduced the gap limitation of the critical anomaly of U_B by incorporating the nature of the density fluctuations in terms of their dependence on the characteristic volume in the model. Concerning the modification of γ due to IEFE, we confirmed that the mathematical expression for the modified Paschen's curve [153,158,159] can be used to derive the deviation of U_B from the right branch of the conventional Paschen's curve. We also found that, while the effect of IEFE is important for electrical discharges under high-pressure conditions, the modification of γ by the density fluctuations near the CP is negligible. These results and the discussion suggest that our breakdown model describes the microscopic relationship between electron acceleration and the density fluctuations well, and therefore allows the microscopic density fluctuations to be linked to the macroscopic behavior of U_B. We believe that the discharge model presented in this work will not only improve studies on breakdown phenomena and electrical properties in high-pressure gases and SCFs including fluids near the CP, but also allow the investigation of other critical anomalies that involve fluctuations, particularly in the field of electric discharges.

3.6 Summary of chapter 3

In this chapter, we focused on the critical anomaly of the breakdown voltages in micrometer gap. Helium has advantages to model the electrical breakdown, such as monatomic simple fluid, low damage to electrodes, and extremely pure condition which is obtained automatically. The experiments in He were enabled by using the temperature controllability of cryoplasma technology.

By the improvements of experimental methods, the critical anomaly of U_B was clearly confirmed, and the number and the dispersion of the measured values of U_B were improved sufficiently to be able to discuss the discharge models developed in this study by fitting analyses.

Three models for reproducing the electrical discharge behavior near the CP were developed. In the first, the power law of a parameter of F_D, which indicates the magnitude of the density fluctuations and proposed in the previous studies [140–142], was extended to the liquid phase. For this, a bubble model considering electron bubbles generated in liquid He was modified by multiplying the power law of F_D. While further improvement of the electrical discharge model will be necessary for further physical discussions, the existence of the threshold density between gas-like and liquid-like breakdown mechanisms, and the validity of the power law of F_D were confirmed.

The second model developed was a hard-sphere cluster model. A method to estimate the effective mean free path of electrons in density fluctuating fluids (λ_{fluc}) was proposed. The model is based on assuming that the gas-like local structure of the density-fluctuating fluid consists of artificial "super" atoms whose radius are proportional to the correlation length ξ. The λ_{fluc} estimated by this model and the measured U_B indicated a strong negative correlation. This implied that λ_{fluc} is one of key parameters to describe the electrical breakdown in the density-fluctuating fluids. However, the main drawback of this model was that it could not reproduce U_B quantitatively.

Finally, a local void model was proposed. In this model, instead of focusing on individual clusters, the cylindrical local low-density domains (voids) created by the density fluctuations were assumed to estimate λ_{fluc}. This model was based on the conventional Townsend discharge theory with modifications of the first Townsend coefficient α due to the variation of λ_{fluc}. In addition, the secondary emission coefficient γ was also modified in the model, to include the effect of ion-enhanced field emission (IEFE). The main characteristic of this model was that it included the size effect of the density fluctuations. The simulation results were in good agreement with the measured dependency of U_B on d, and the dependency was suggested to be caused by the behavior of λ_{fluc}. Moreover, the roles of the density fluctuation and the high-density conditions on α and γ coefficients were discussed. The concepts of this model, such as the size effect of the density fluctuation and the evaluation of the electron motion, may enable a better reaction model in fluctuating fluids.

Chapter 4

Conclusion

In this thesis, “cryoplasmas”, whose plasma gas temperature (i.e. the temperature of neutral species in plasmas, T_g) are controlled continuously at lower than room temperature (5 – 300 K), were investigated (Figure 1.15). T_g is one of the most important parameters in plasma science and technology, because T_g affects the plasma chemistry and transportation of heavy neutral species including excited species and radicals, and their interaction with condensed-phase materials. However, up to now, the role of T_g in high-pressure plasmas has not been studied sufficiently, and therefore, T_g can be considered as a kind of a “new” parameter in non-equilibrium plasmas. In the new and exotic T_g region of cryogenic temperatures, both phenomena —peculiar to cryogenic temperatures and showing a continuous variation from conventional temperatures higher than room temperature— are expected to appear. Using the advantageous characteristics of cryoplasmas, the role of T_g in high-pressure non-equilibrium plasmas and the roles of high-density condition and density fluctuations in electrical breakdown were discussed.

To investigate the role of T_g in plasma chemistry, fundamental diagnostics of He cryoplasmas and discussion using my developed reaction model were conducted. At first, T_g was evaluated by laser interferometry and thermal simulation, and as a result, the increment of T_g in the cryoplasmas generated in this thesis was estimated to be suppressed below around 10 K. Then, for the phenomena peculiar to cryogenic temperatures measured by OES and LAS in this study, such as the temporal behavior of optical emission intensities and the density and the lifetime of metastable He atom, the reaction model for He with small amount of impurities (N_2, O_2, and H_2O) were developed. The most striking feature of the model was that the dependencies of the reaction rate constants of elemental reactions and the diffusion constants of the species on T_g were taken into account. By using the model, the experimental results of OES and LAS were reproduced quasi-quantitatively or qualitatively, and the contributions and the ratio of impurity species were evaluated. As a result of the reaction simulation, both the drastic variation of plasma chemistry due to phase changes and the gradual variation due to continuous variation of collision parameters (collision frequency, collision cross section, etc.) were confirmed. The dominant species and the elemental reactions transformed with decreasing T_g. Thus, how the plasma chemistry depend on T_g were clarified. In addition, even in the T_g range in which the drastic variation of plasma chemistry do not appear, quench frequency and ratio of quench rates of reactions and diffusion were affected by the variation of T_g. Therefore, it was suggested that the dependency of plasma reaction should not be ignored not only at cryogenic temperatures but also above room temperature.

Thus, the role of the new parameter of T_g for non-equilibrium plasmas was discussed and the importance of T_g was clarified. In He gas, the three-body reaction of He^m with He atoms (R6), which needs a low activation energy comparable to the energy of room temperature, was the most important elemental reaction. In addition, other reactions show a variety of T_g dependencies. By the combination of the variations of elemental reactions and phase changes, dynamic variation of plasma chemistry was caused. For other gas systems, although T_g might not be always as important as for He plasma chemistry, the discussion about T_g should be inevitable to understand plasma chemistry and control plasma reactions precisely.

Next, the roles of high-density condition and density fluctuations in electrical breakdown were discussed. By the improvements of experimental methods, the number and the dispersion of the measured values of U_B were improved enough to be able to discuss my developed discharge models by fitting analysis. Three electrical breakdown models were proposed (Bubble mode, Hard sphere cluster model, and Local voids model). Bubble model was the expansion from liquid(-like) states and the other models were based on gaseous discharge models. The effective mean free path of electron in density fluctuating fluids (λ_{fluc}) was proposed and it was suggested that λ_{fluc} was one of the key parameters to describe the electrical breakdown in the density-fluctuating fluids from the hard sphere cluster model. In the local void model, the cylindrical local low-density domains (voids) created by the density fluctuation were assumed to estimate λ_{fluc}. The main characteristic of this model was that it included the size effect of the density fluctuation. In addition, the effect of electron supply due to IEFE from cathode was considered. The calculation results of U_B were in good agreement with the dependency of U_B on d, and the dependency was suggested to be caused by the behavior of λ_{fluc}. The concepts of this model, such as the size effect of the density fluctuation and the evaluation of the electron motion, may enable a better reaction model in fluctuating fluids.

Thus, the role and importance of the “new” parameter in high-pressure non-equilibrium plasmas, T_g, was clearly demonstrated and, by focusing on and controlling T_g, the role and importance of the local fluid structure in discharge physics in high-pressure (and close to condensed) conditions were revealed. The results presented in this thesis are expected to allow a more accurate control of the generation and the plasma chemistry in high-pressure non-equilibrium plasmas, such as atmospheric pressure plasmas and SCF plasmas, which may lead to novel applications of plasma-based materials processing.

Bibliography

[1] D. Ishihara, Y. Noma, S. Stauss, M. Sai, T. Tomai, and K. Terashima, Plasma Sources Sci. Technol. **17**, 035008 (2008).

[2] Y. Noma, J. H. Choi, S. Stauss, T. Tomai, and K. Terashima, Appl. Phys. Express **1**, 046001 (2008).

[3] Y. Noma, J. H. Choi, T. Tomai, and K. Terashima, Appl. Phys. Lett. **93**, 101503 (2008).

[4] J. H. Choi, Y. Noma, T. Tomai, and K. Terashima, Appl. Phys. Lett. **93**, 081504 (2008).

[5] J. H. Choi, Y. Noma, and K. Terashima, Plasma Sources Sci. Technol. **18**, 025023 (2009).

[6] J. H. Choi, Y. Noma, M. Sano, and K. Terashima, J. Phys. D. Appl. Phys. **43**, 072001 (2010).

[7] Y. Noma, J. Hyuk Choi, H. Muneoka, and K. Terashima, J. Appl. Phys. **109**, 053303 (2011).

[8] F. Iacopi, J. H. Choi, K. Terashima, P. M. Rice, and G. Dubois, Phys. Chem. Chem. Phys. **13**, 3634 (2011).

[9] S. Stauss, N. Ebato, F. Oshima, H. Muneoka, D. Z. Pai, and K. Terashima, IEEE Trans. Plasma Sci. **39**, 2184 (2011).

[10] S. Stauss, S. Mori, H. Muneoka, K. Terashima, and F. Iacopi, J. Vac. Sci. Technol. B Microelectron. Nanom. Struct. **31**, 061202 (2013).

[11] S. Stauss, H. Muneoka, N. Ebato, F. Oshima, D. Z. Pai, and K. Terashima, Plasma Sources Sci. Technol. **22**, 025021 (2013).

[12] K. Itoh, A. Muraoka, K. Watanabe, T. Nagata, M. Nishikawa, and R. A. Holroyd, J. Phys. Chem. B **108**, 10177 (2004).

[13] O. Takai, Pure Appl. Chem. **80**, 2003 (2008).

[14] S. Stauss, H. Muneoka, K. Urabe, K. Terashima, S. Stauss, H. Muneoka, K. Urabe, and K. Terashima, Phys. Plasmas **22**, 057103 (2015).

[15] T. C. Killian, Science **316**, 705 (2007).

[16] M. N. Hirsh and H. J. Oskam, editors , in *Gaseous Electron. Electr. Discharges* (Academic Press, New York, 1978), pp. 291–398.

[17] "Recommended data for electron collision cross section of atoms and molecules", compiled by a technical society of The Institute of Electrical Engineers of Japan [in Japanese Report 3853, Sep. 2001]. http://www.bookpark.ne.jp/cm/ieej/detail.asp?content_id, retrived date 20 May 2015.

[18] 結城和久，プラズマ核融合学会誌 **85**, 558 (2009).

[19] 山田哲哉，安部隆士，プラズマ核融合学会誌 **82**, 368 (2006).

[20] R. Foest, M. Schmidt, and K. Becker, Int. J. Mass Spectrom. **248**, 87 (2006).

[21] M. Nagai, M. Hori, and T. Goto, J. Vac. Sci. Technol. A Vacuum, Surfaces, Film. **23**, 221 (2005).

[22] N. K. Bibinov, A. A. Fateev, and K. Wiesemann, J. Phys. D Appl. Phys. **34**, 1819 (2001).

[23] J. S. Chang, R. M. Hobson, Y. Ichikawa, and T. Kaneda, *Atomic and Molecular Processes in an Ionized Gas* (Tokyo Denki University Press, Tokyo, 1983).

[24] 宗岡均，寺嶋和夫，化学工学誌 **75**, 359 (2011).

[25] 野間由里，崔宰赫，佐野正樹，寺嶋和夫，プラズマ核融合学会誌 **85**, 526 (2009).

[26] E. Lemmon, M. McLinden, and D. Friend, *NIST Standard Reference Database 23: Reference Fluid Thermodynamic and Transport Properties- REFPROP, Version 9.0* (National Institute of Standards and Technology, Standard Reference Data Program, Gaithersburg, 2012).

[27] K. Urabe, H. Muneoka, S. Stauss, and K. Terashima, Plasma Sources Sci. Technol. **23**, 064007 (2014).

[28] "Properties of Upilex(R)-S, UBE INDUSTRIES, LTD.", http://www.ube-ind.co.jp/english/products/chemical/chemical_11_01.htm, retrieved date 26 May 2015.

[29] AIST Thermophysical Properties Database System TPDS-web, http://tpds.db.aist.go.jp/tpds-web/, retrieved date 30 January 2014.

[30] S. Nishio ed., *JSME Data Book: Heat Transfer 5th Edition* (The Japan Society of Mechanical Engineers, Tokyo, 2009).

[31] C. W. Allen, *Astrophysical Quantities*, 3rd ed. (Athlon Press, London, 1973).

[32] A. Kramida, Y. Ralchenko, J. Reader, and NIST ASD Team, *NIST Atomic Spectra Database* (version 5.2, 2014) [http://physics.nist.gov/ asd].

[33] R. W. B. Pearse and A. G. Gaydon, *The Identification of Molecular Spectra* (Chapman and Hall, London, 1976).

[34] P. J. Linstrom and W. G. Mallard, *NIST Chemistry WebBook, NIST Standard Reference Database* (No. 69, 2014) [http://webbook.nist.gov/chemistry].

[35] K. Tachibana, Y. Kishimoto, and O. Sakai, J. Appl. Phys. **97**, 123301 (2005).

[36] K. Urabe, T. Morita, K. Tachibana, and B. N. Ganguly, J. Phys. D. Appl. Phys. **43**, 095201 (2010).

[37] W. Demtröder, *Laser Spectroscopy*, 4th ed. (Springer, Berlin, 2008).

[38] A. V. Phelps and J. P. Molnar, Phys. Rev. **89**, 1202 (1953).

[39] A. V Phelps and S. C. Brown, Phys. Rev. **86**, 102 (1952).

[40] K. H. Ludlum, L. P. Larson, and J. M. Caffrey, J. Chem. Phys. **46**, 127 (1967).

[41] A. Köymen, F.-C. Tang, X. Zhao, F. B. Dunning, and G. K. Walters, Chem. Phys. Lett. **168**, 405 (1990).

[42] E. E. Ferguson, Annu. Rev. Phys. Chem. **26**, 17 (1975).

[43] R. A. Gerber and M. A. Gusinow, Phys. Rev. A **4**, 2027 (1971).

[44] J. B. Gerardo and M. A. Gusinow, Phys. Rev. A **3**, 255 (1971).

[45] J.-F. Delpech and J.-C. Gauthier, Phys. Rev. A **6**, 1932 (1972).

[46] I. Y. Fugol and P. L. Pakhomov, JETP Lett. **3**, 254 (1966).

[47] I. Y. Fugol, O. N. Grigorashchenko, and D. A. Myshkis, Sov. Phys. JETP **33**, 227 (1971).

[48] W. A. Fitzsimmons, N. F. Lane, and G. K. Walters, Phys. Rev. **174**, 193 (1968).

[49] R. Deloche, P. Monchicourt, M. Cheret, and F. Lambert, Phys. Rev. A **13**, 1140 (1976).

[50] M. L. Ginter, J. Chem. Phys. **52**, 4469 (1970).

[51] K. Niemi, J. Waskoenig, N. Sadeghi, T. Gans, and D. O'Connell, Plasma Sources Sci. Technol. **20**, 055005 (2011).

[52] S. Chapman and T. G. Cowling, *The Mathematical Theory of Non-Uniform Gases*, Third edit (Cambridge University Press, Cambridge, 1970).

[53] K. Nanbu, J. Phys. Soc. Japan **59**, 4331 (1990).

[54] K. Minami, Y. Yamanishi, C. Kojima, M. Shindo, and O. Ishihara, IEEE Trans. Plasma Sci. **31**, 429 (2003).

[55] A. B. Callear and R. E. M. Hedges, Nature **215**, 1267 (1967).

[56] A. B. Callear and R. E. M. Hedges, Trans. Faraday Soc. **66**, 2921 (1970).

[57] J. W. Shon and M. J. Kushner, J. Appl. Phys. **75**, 1883 (1994).

[58] D. W. Tokaryk, R. L. Brooks, and J. L. Hunt, Phys. Rev. A **48**, 364 (1993).

[59] B. M. Smirnov, Sov. Phys. Jetp **24**, 1180 (1967).

[60] Y. B. Golubovskii, V. a Maiorov, J. Behnke, and J. F. Behnke, J. Phys. D. Appl. Phys. **36**, 39 (2003).

[61] I. A. Kossyi, A. Y. Kostinsky, A. A. Matveyev, and V. P. Silakov, Plasma Sources Sci. Technol. **1**, 207 (1992).

[62] M. H. Bortner and T. Baurer, in *Def. Nucl. AGENCY React. RATE Handb.*, Second Edi (1972).

[63] R. J. Vidmar and K. R. Stalder, *Final Performance Report. (Computations of the Power to Sustain Plasma in Air with Relevance to Aerospace Technology. Final Report Prepared for Air Force Office of Scientific Research.* (2004).

[64] R. J. Vidmar, IEEE Trans. Plasma Sci. **18**, 733 (1990).

[65] Y. Sakiyama and D. B. Graves, J. Appl. Phys. **101**, 073306 (2007).

[66] J. M. Pouvesle, J. Stevefelt, and C. B. Collins, J. Chem. Phys. **88**, 3061 (1988).

[67] T. M. Kojima, N. Saito, N. Kobayashi, and Y. Kaneko, J. Phys. Soc. Jpn. **61**, 6 (1992).

[68] A. S. Dickinson, M. S. Lee, and L. A. Viehland, J. Phys. B At. Mol. Opt. Phys. **32**, 4919 (1999).

[69] P. L. Patterson, J. Chem. Phys. **48**, 3625 (1968).

[70] J. Sanderson, H. Tanuma, N. Kobayashi, and Y. Kaneko, J. Phys. B At. Mol. Opt. Phys. **26**, L465 (1993).

[71] A. V. Phelps, Phys. Rev. **99**, 1307 (1955).

[72] M. A. Gusinow, R. A. Gerber, and J. B. Gerardo, Phys. Rev. Lett. **25**, 1248 (1970).

[73] W. Koch, G. Frenking, J. Gauss, D. Cremer, and J. R. Collins, J. Am. Chem. Soc. **109**, 5917 (1987).

[74] D. Smith, Chem. Rev. **92**, 1473 (1992).

[75] A. G. G. M. Tielens, *The Physics and Chemistry of the Interstellar Medium* (Cambridge University Press, Cambridge, 2010).

[76] T. Murakami, K. Niemi, T. Gans, D. O'Connell, and W. G. Graham, Plasma Sources Sci. Technol. **22**, 015003 (2013).

[77] T. Murakami, K. Niemi, T. Gans, D. O'Connell, and W. G. Graham, Plasma Sources Sci. Technol. **22**, 045010 (2013).

[78] D. Breden, K. Miki, and L. L. Raja, Appl. Phys. Lett. **99**, 111501 (2011).

[79] K. R. Stalder, R. J. Vidmar, G. Nersisyan, and W. G. Graham, J. Appl. Phys. **99**, 093301 (2006).

[80] G. V Naidis, J. Phys. D. Appl. Phys. **44**, 215203 (2011).

[81] A. L. Schmeltekopf, E. E. Ferguson, and F. C. Fehsenfeld, J. Chem. Phys. **48**, 2966 (1968).

[82] B. J. Garrison, W. H. Miller, and H. F. Schaefer, J. Chem. Phys. **59**, 3193 (1973).

[83] G. J. M. Hagelaar and L. C. Pitchford, Plasma Sources Sci. Technol. **14**, 722 (2005).

[84] PHELPS database, www.lxcat.laplace.univ-tlse.fr, retrieved date 4 June 2013.

[85] SIGLO database, www.lxcat.laplace.univ-tlse.fr, retrieved date 4 June 2013.

[86] A. V. Phelps and L. C. Pitchford, Phys. Rev. A **31**, 2932 (1985).

[87] A. W. Johnson and J. B. Gerardo, Phys. Rev. A **7**, 807 (1973).

[88] J. E. Lawler, J. W. Parker, and L. W. Anderson, Phys. Lett. A **69**, 408 (1979).

[89] J. Stevefelt, Phys. Rev. A **8**, 2507 (1973).

[90] J. Dubau and S. Volonté, Rep. Prog. Phys. **43**, 199 (1980).

[91] P. A. Shaver, Astron. Astrophys. **46**, 127 (1976).

[92] K. J. Lagattuta, Nucl. Instruments Methods Phys. Res. A **240**, 549 (1985).

[93] R. J. Gould and R. K. Thakur, Ann. Phys. (N. Y). **61**, 351 (1970).

[94] A. Burgess and H. P. Summers, Astrophys. J. **157**, 1007 (1969).

[95] K. Takaki, H. Kirihara, C. Noda, S. Mukaigawa, and T. Fujiwara, Jpn. J. Appl. Phys. **45**, 8241 (2006).

[96] K. Urabe, Y. Ito, K. Tachibana, and B. N. Ganguly, Appl. Phys. Express **1**, 066004 (2008).

[97] T. Murakami, K. Niemi, T. Gans, D. O. Connell, and W. G. Graham, Plasma Sources Sci. Technol. **23**, 025005 (2014).

[98] K. Nishikawa and I. Tanaka, Chem. Phys. Lett. **244**, 149 (1995).

[99] K. Nishikawa and T. Morita, J. Supercrit. Fluids **13**, 143 (1998).

[100] G. G. Simeoni, T. Bryk, F. A. Gorelli, M. Krisch, G. Ruocco, M. Santoro, and T. Scopigno, Nat. Phys. **6**, 503 (2010).

[101] C. A. Eckert, B. L. Knutson, and P. G. Debenedetti, Nature **383**, 313 (1996).

[102] P. E. Savage, Chem. Rev. **99**, 603 (1999).

[103] M. Herrero, a Cifuentes, and E. Ibanez, Food Chem. **98**, 136 (2006).

[104] T. L. Chester, J. D. Pinkston, and D. E. Raynie, Anal. Chem. **66**, 106R (1994).

[105] H. Namatsu, J. Vac. Sci. Technol. B Microelectron. Nanom. Struct. **18**, 3308 (2000).

[106] F. Cansell and C. Aymonier, J. Supercrit. Fluids **47**, 508 (2009).

[107] E. Reverchon and R. Adami, J. Supercrit. Fluids **37**, 1 (2006).

[108] H. E. Stanley, *Introduction to Phase Transitions and Critical Phenomena* (Oxford University Press, Oxford, 1971).

[109] L. H. Cohen, M. L. Dingus, and H. Meyer, J. Low Temp. Phys. **49**, 545 (1982).

[110] A. Acton and K. Kellner, Phys. B+C **103**, 212 (1981).

[111] L. P. Kadanoff and J. Swift, Phys. Rev. **166**, 89 (1968).

[112] A. Onuki, Phys. Rev. E **55**, 403 (1997).

[113] B. J. Bailey and K. Kellner, Brit. J. Appl. Phys. **18**, 1645 (1967).

[114] J. V. Sengers and J. M. H. L. Sengers, Ann. Rev. Phys. Chem. **37**, 189 (1986).

[115] C. A. Eckert, D. H. Ziger, K. P. Johnston, and S. Kim, J. Chem. Phys. **90**, 2738 (1986).

[116] I. B. Petsche and P. G. Debenedetti, J. Chem. Phys. **91**, 7075 (1989).

[117] A. Tominaga, J. Low Temp. Phys. **16**, 571 (1974).

[118] H. D. Bale, B. C. Dobbs, S. Lin, and P. W. Schmidt, Phys. Rev. Lett. **25**, 1556 (1970).

[119] K. P. Johnston and C. Haynes, AIChE J. **33**, 2017 (1987).

[120] M. E. Paulaitis and G. C. Alexander, Pure Appl. Chem. **59**, 61 (1987).

[121] J. B. Ellington, K. M. Park, and J. F. Brennecke, Ind. Eng. Chem. Res. **33**, 965 (1994).

[122] T. Koga, Y.-S. Seo, Y. Zhang, K. Shin, K. Kusano, K. Nishikawa, M. Rafailovich, J. Sokolov, B. Chu, D. Peiffer, R. Occhiogrosso, and S. Satija, Phys. Rev. Lett. **89**, 125506 (2002).

[123] T. Koga, E. Akashige, a. Reinstein, M. Bronner, Y.-S. Seo, K. Shin, M. H. Rafailovich, J. C. Sokolov, B. Chu, and S. K. Satija, Phys. B **357**, 73 (2005).

[124] A. A. Arai, T. Morita, and K. Nishikawa, J. Chem. Phys. **119**, 1502 (2003).

[125] C. C. Liew, H. Inomata, and S. Saito, Fluid Phase Equilib. **104**, 317 (1995).

[126] N. Yoshii and S. Okazaki, J. Chem. Phys. **107**, 2020 (1997).

[127] K. H. Becker, U. Kogelschatz, K. H. Schoenbach, and R. J. Barker, editors , *NON-EQUILIBRIUM AIR PLAMSA AT ATMOSPHERIC PRESSURE* (Institute of Physics Publishing, Bristol, 2005).

[128] M. Kogoma, M. Kusano, and Y. Kusano, editors , *Generation and Applications of Atmospheric Pressure Plasmas* (Nova Science Publishers, Inc., New York, 2011).

[129] P. Bruggeman and C. Leys, J. Phys. D. Appl. Phys. **42**, 053001 (2009).

[130] T. Nozaki, A. Ağıral, S. Yuzawa, J. G. E. Han Gardeniers, and K. Okazaki, Chem. Eng. J. **166**, 288 (2011).

[131] W. J. Humphreys, Astrophys. J. **26**, 18 (1907).

[132] D. R. Young, J. Appl. Phys. **21**, 222 (1950).

[133] R. Meats, Proc. Inst. Electr. Eng. **119**, 760 (1972).

[134] I. Ishii and T. Noguchi, Proc. Inst. Electr. Eng. **126**, 532 (1979).

[135] C. H. Zhang, T. Kiyan, T. Namihira, A. Uemura, S. Katsuki, H. Akiyama, T. Fang, M. Sasaki, and M. Goto, IAS **3**, 1845 (2005).

[136] T. Kiyan, A. Uemura, B. C. Roy, T. Namihira, M. Hara, M. Sasaki, M. Goto, and H. Akiyama, IEEE Trans. Plasma Sci. **35**, 656 (2007).

[137] T. Tomai, H. Yui, and K. Terashima, Appl. Phys. Lett. **94**, 151501 (2009).

[138] T. Tomai, K. Katahira, H. Kubo, Y. Shimizu, T. Sasaki, N. Koshizaki, and K. Terashima, J. Supercrit. Fluids **41**, 404 (2007).

[139] K. Saitow and T. Yamamura, J. Phys. Chem. C **113**, 8465 (2009).

[140] T. Ito and K. Terashima, Appl. Phys. Lett. **80**, 2854 (2002).

[141] T. Ito, H. Fujiwara, and K. Terashima, J. Appl. Phys. **94**, 5411 (2003).

[142] M. Sawada, T. Tomai, T. Ito, H. Fujiwara, and K. Terashima, J. Appl. Phys. **100**, 123304 (2006).

[143] D. A. Lacoste, H. Muneoka, D. Z. Pai, S. Stauss, and K. Terashima, Plasma Sources Sci. Technol. **21**, 052003 (2012).

[144] H. Muneoka, K. Urabe, S. Stauss, and K. Terashima, Appl. Phys. Express **6**, 086201 (2013).

[145] T. Kato, S. Stauss, S. Kato, K. Urabe, M. Baba, T. Suemoto, and K. Terashima, Appl. Phys. Lett. **101**, 224103 (2012).

[146] K. Urabe, T. Kato, S. Stauss, S. Himeno, S. Kato, H. Muneoka, M. Baba, T. Suemoto, and K. Terashima, J. Appl. Phys. **114**, 143303 (2013).

[147] H. Kikuchi, S. Stauss, S. Nakahara, F. Matsubara, T. Tomai, T. Sasaki, and K. Terashima, J. Supercrit. Fluids **55**, 325 (2010).

[148] S. Stauss, H. Miyazoe, T. Shizuno, K. Saito, T. Sasaki, and K. Terashima, Jpn. J. Appl. Phys. **49**, 070213 (2010).

[149] T. Shizuno, H. Miyazoe, K. Saito, S. Stauss, M. Suzuki, T. Sasaki, and K. Terashima, Jpn. J. Appl. Phys. **50**, 030207 (2011).

[150] Y. P. Raizer, *Gas Discharge Physics* (Springer-Verlag, Berlin, 1991).

[151] M. J. Druyvesteyn and F. M. Penning, Rev. Mod. Phys. **12**, 87 (1940).

[152] W. S. Boyle and P. Kisliuk, Phys. Rev. **97**, 255 (1955).

[153] D. B. Go and D. A. Pohlman, J. Appl. Phys. **107**, 103303 (2010).

[154] R.-T. Lee, H.-H. Chung, and Y.-C. Chiou, IEE Proc. -Sci. Meas. Technol. **148**, 8 (2001).

[155] A. Wallash and L. Levitb, Proc. SPIE **4980**, 87 (2003).

[156] M. Radmilović-Radjenović and B. Radjenović, IEEE Trans. Plasma Sci. **35**, 1223 (2007).

[157] M. Radmilović-Radjenović and B. Radjenović, Plasma Sources Sci. Technol. **17**, 024005 (2008).

[158] R. Tirumala and D. B. Go, Appl. Phys. Lett. **97**, 151502 (2010).

[159] P. Rumbach and D. B. Go, J. Appl. Phys. **112**, 103302 (2012).

[160] A. Venkattraman and A. A. Alexeenko, Phys. Plasmas **19**, 123515 (2012).

[161] D. B. Go and A. Venkattraman, J. Phys. D. Appl. Phys. **47**, 503001 (2014).

[162] J.-M. Torres and R. S. Dhariwal, Nanotechnology **10**, 102 (1999).

[163] P. G. Slade and E. D. Taylor, IEEE Trans. Components Packag. Technol. **25**, 390 (2002).

[164] E. Hourdakis, G. W. Bryant, and N. M. Zimmerman, J. Appl. Phys. **100**, 123306 (2006).

[165] Y. Li and D. B. Go, J. Appl. Phys. **116**, 103306 (2014).

[166] R. H. Fowler and L. Nordheim, Proc. R. Soc. London. Ser. A, Contain. Pap. a Math. Phys. Character **119**, 173 (1928).

[167] W. W. Dolan, Phys. Rev. **91**, 510 (1953).

[168] R. Good and E. Müller, in *Encycl. Phys. vol.21 Electron-Emission, Gas Disch. I* (Springer, Berlin, 1956), pp. 176–231.

[169] A. H. Cookson, Proc. Inst. Electr. Eng. **128**, 303 (1981).

[170] D. Z. Pai, S. Stauss, and K. Terashima, Plasma Sources Sci. Technol. **23**, 025019 (2014).

[171] A. H. Cookson, Proc. Inst. Electr. Eng. **117**, 269 (1970).

[172] D. Z. Pai, S. Stauss, and K. Terashima, Plasma Sources Sci. Technol. **24**, 025021 (2015).

[173] C. Bréchignac, M. Broyer, P. Cahuzac, G. Delacretaz, P. Labastie, J. P. Wolf, and L. Wöste, Phys. Rev. Lett. **60**, 275 (1988).

[174] C. Y. Ng, Adv. Chem. Phys. **52**, 263 (1983).

[175] W. D. Knight, W. A. de Heer, and W. A. Saunders, Z. Phys. D - Atoms, Mol. Clust. **3**, 109 (1986).

[176] V. Giraud and P. Krebs, Chem. Phys. Lett. **86**, 85 (1982).

[177] S. S.-S. Huang and G. R. Freeman, J. Chem. Phys. **68**, 1355 (1978).

[178] J. Gerhold, IEEE Trans. Electr. Insul. **23**, 765 (1988).

[179] T. Furusato, T. Ihara, T. Kiyan, S. Katsuki, M. Hara, and H. Akiyama, IEEE Trans. Plasma Sci. **40**, 3105 (2012).

[180] T. Ihara, T. Furusato, S. Kameda, T. Kiyan, S. Katsuki, M. Hara, and H. Akiyama, J. Phys. D. Appl. Phys. **45**, 075204 (2012).

[181] K. Horii, M. Kosaki, A. J. Pearmain, and A. J. McNerney, Cryogenics (Guildf). **23**, 102 (1983).

[182] F. Paschen, Ann. Phys. **273**, 69 (1889).

[183] B. K. P. Scaife, *Principles of Dielectrics* (Oxford University Press, Oxford, 1998).

[184] K. Akiyama, T. Eguchi, T. An, Y. Hasegawa, T. Okuda, a. Harasawa, and T. Kinoshita, Rev. Sci. Instrum. **76**, 083711 (2005).

[185] J. Gerhold, IEEE Trans. Electr. Insul. **24**, 155 (1989).

[186] Z. -l. Li, N. Bonifaci, F. Aitken, a. Denat, K. Haeften, V. Atrazhev, and V. Shakhatov, IEEE Trans. Dielectr. Electr. Insul. **16**, 742 (2009).

[187] Z. Krasucki, Proc. R. Soc. A **294**, 393 (1966).

[188] A. Bondi, J. Phys. Chem. **68**, 441 (1964).

[189] M. Iino, M. Suzuki, and A. J. Ikushima, J. Low Temp. Phys. **63**, 495 (1986).

[190] N. Yoshii and S. Okazaki, Fluid Phase Equilib. **144**, 225 (1998).

[191] S. Nakayama and D. Ito, Cryogenics (Guildf). **26**, 12 (1986).

[192] T. Sato, M. Sugiyama, K. Itoh, K. Mori, T. Fukunaga, M. Misawa, T. Otomo, and S. Takata, Phys. Rev. E **78**, 051503 (2008).

[193] D. Andrick and A. Bitsch, J. Phys. B At. Mol. Phys. **8**, 393 (1975).

[194] Y. Li, R. Tirumala, P. Rumbach, and D. B. Go, IEEE Trans. Plasma Sci. **41**, 24 (2013).

Acknowledgement

This work was carried out between October 2012 and September 2015 in Terashima laboratory, the University of Tokyo. Over the last 3 years I had an exciting and interesting life in this laboratory. My work was supported by many people and great environment.

Now I would like to thank,

Prof. Dr. Kazuo Terashima, director of this thesis;

for giving me an opportunity to have the great 3-years period through the Ph.D course and also the 3.5-years of undergraduate and master courses before starting the Ph.D course, fruitful scientific discussions, directing the topics of this work, great environment for studying, tasks necessary for me to grow up my skill as a researcher and human being, encouragements based on wide and deep visions.

Prof. Dr. Kaoru Kimura, Prof. Dr. Fumitaka Tsukihashi, Assoc. Prof. Dr. Makoto Kambara, and Assoc. Prof. Dr. Yusuke Tokunaga;

for many scientific suggestions and discussions for this thesis.

Dr. Sven Stauss;

for many discussions, kind comments and helps for this thesis, teaching me a lot of things as a researcher.

Dr. Keiichiro Urabe;

for many and many scientific suggestions and discussions for this thesis, suggestionable advices for my research life, and supports in many fields. If I had not collaborated with you, I could not have obtained such many achievements in this study.

Dr. Jai Hyuk Choi:

for many discussions, cooperation, and great teaching the introduction of this study for me at the beginning of my research life.

Dr. David Pai and Dr. Deanna Lacoste;

for fruitful suggestions to my work and teaching me an attitude for research.

Mr. Fumito Oshima, Mr. Toru Kato, Mr. Yasuhito Matsubayashi, Mr. Ryoma Yasui and Mr. Noritaka Sakakibara;

for collaboration, a lot of supports, assistance, efforts, contributions, discussions to my work, and everyday life.

All my colleagues in Terashima Laboratory;

for the excited life, discussions and many supports.

My family, father, mother, and brother;

for many encouragements and supports.

My wife, Hiroko;

for everything in my life.

June 2015

Publication and presentation lists

1. Journal papers

Articles related to this thesis are **1**, **2**, **3**, **5**, and **13**.

1. H. Muneoka, K. Urabe, S. Stauss, and K. Terashima
"Laser diagnostics of quasi-atmospheric-pressure cryoplasmas in self-limited discharges"
Plasma Sources Science and Technology, in preparation.

2. K. Urabe, **H. Muneoka**, S. Stauss, and K. Terashima
"Laser absorption spectroscopy diagnostics of helium metastable atoms generated in dielectric barrier discharge cryoplasmas"
Japanese Journal of Applied Physics, submitted.

3. **H. Muneoka**, K. Urabe, S. Stauss, and K. Terashima
"Micrometer-scale electrical breakdown in high-density fluids with large density fluctuations: Numerical model and experimental assessment"
Physical Review E **91** (2015) 042316 (11 pages).

4. S. Stauss, **H. Muneoka**, K. Urabe, and K. Terashima
"Review of electric discharge microplasmas generated in highly fluctuating fluids: Characteristics and application to nanomaterials synthesis"
Physics of Plasmas **22** (2015) 057103 (14 pages).

5. **H. Muneoka**, K. Urabe, S. Stauss, and K. Terashima
"Experimental and Numerical Investigation of Time-Evolution of Discharge Current and Optical Emission in Helium-Nitrogen Cryoplasmas"
Plasma Sources Science and Technology **23** (2014) 065038 (11 pages).

6. S. Himeno, T. Kato, K. Urabe, S. Stauss, S. Kato, **H. Muneoka**, M. Baba, T. Suemoto, and K. Terashima
"Anomalous behavior of the cavitation bubble observed in pulsed laser ablation of Ni in liquid CO_2 near the critical point"
IEEE Transactions on Plasma Science **42** (2014) 2630-2631 (2 pages).

7. K. Urabe, **H. Muneoka**, S. Stauss, and K. Terashima
"Microscopic heterodyne interferometry for determination of electron density in high-pressure microplasma"
Plasma Sources Science and Technology **23** (2014) 064007 (9 pages) [Selected to "Highlights of 2014"].

8. **H. Muneoka** and K. Terashima
"Breakdown Phenomena and Nanomaterial Syntheses in Supercritical Fluid Plasmas"
Journal of Plasma and Fusion Research **90** (2014) 384-391 (8 pages). (in Japanese)
宗岡均、寺嶋和夫
『小特集「プラズマとナノ界面の相互作用」 3.超臨界流体プラズマの絶縁破壊・ナノ物質合成と密度揺らぎ』
プラズマ核融合学会誌 **90** (2014) 384-391.

9. D. A. Lacoste, **H. Muneoka**, T. F. Guiberti, D. Z. Pai, K. Urabe, S. Stauss, and K. Terashima
"Effect of light irradiation on Townsend breakdown in gaseous and supercritical helium at 5.2 K"
Plasma Sources Science and Technology **22** (2014) 012002 (5 pages).

10. K. Urabe, **H. Muneoka**, S. Stauss, and K. Terashima
"Development of Near-Infrared Laser Heterodyne Interferometry for Diagnostics of Electron and Gas Number Densities in Microplasmas"
Applied Physics Express **6** (2013) 1261018 (4 pages).

11. S. Stauss, S. Mori, **H. Muneoka**, K. Terashima, and F. Iacopi
"Ashing of photoresists using dielectric barrier discharge cryoplasmas"
Journal of Vacuum Science and Technology B **31** (2013) 061202 (8 pages).

12. K. Urabe, T. Kato, S. Stauss, S. Himeno, S. Kato, **H. Muneoka**, M. Baba, T. Suemoto, and K. Terashima
"Dynamics of pulsed laser ablation in high-density carbon dioxide including supercritical fluid state"
Journal of Applied Physics **114** (2013) 143303 (7 pages).

13. **H. Muneoka**, K. Urabe, S. Stauss, and K. Terashima
"Breakdown Characteristics of Electrical Discharges in High-Density Helium near the Critical Point"
Applied Physics Express **6** (2013) 086201 (4 pages).

14. S. Stauss, **H. Muneoka**, N. Ebato, F. Oshima, D. Z. Pai, and K. Terashima
"Self-organized pattern formation in helium dielectric barrier discharge cryoplasmas"
Plasma Sources Sci. Techonol., **22** (2013) 025021 (9 pages).

15. D. A. Lacoste, **H. Muneoka**, D. Z. Pai, S. Stauss, and K. Terashima
"Breakdown characteristics of a nanosecond-pulsed plasma discharge in supercritical air"
Plasma Sources Science and Technology **21** (2012) 052003 (4 pages).

16. S. Stauss, N. Ebato, F. Oshima, **H. Muneoka**, D. Pai, and K. Terashima
"Uniform, filamentary and striped dielectric barrier discharge cryoplasmas generated in helium at atmospheric pressure"
IEEE Plasma Science and Technology **39** (2011) 2184-2185 (2 pages).

17. Y. Noma, J. H. Choi, **H. Muneoka**, and K. Terashima
"Electron density and temperature of gas-temperature dependent cryoplasma jet",
Journal of Applied Physics **109** (2011) 053303 (6 pages).

18. **H. Muneoka** and K. Terashima
"Part 4, Chapter 6, Gas-temperature-controlled plasma in advanced material processes" in "Atmospheric Plasma its Technology and Process Development"
A. Okino ed, (CMC, Tokyo, 2011) pp. 220-228 (9 pages). (in Japanese)
宗岡均、寺嶋和夫
『第Ⅳ編　第6章　先進材料プロセスにおけるガス温度制御型プラズマ —クライオプラズマを例として—』
沖野晃俊監修『大気圧プラズマの技術とプロセス開発』CMC 出版 (2011) 220-228.

19. **H. Muneoka** and K. Terashima
"Novel nanoporous material processing developed by cryoplasma"
Monthly Journal of Society for Chemical Engineers Japan **75** (2011) 359-361 (3 pages). (in Japanese)
宗岡均、寺嶋和夫
『特集「大気圧プラズマが拓くあたらしい技術」 クライオプラズマが切り開くナノポーラスマテリアルプロセシングの新展開』
化学工学誌 **75** (2011) 359-361.

2. Presentations

International

1. °**H. Muneoka**, K. Urabe, S. Stauss, and K. Terashima
"Dependency of Reaction Dynamics on Plasma Gas Temperature in He/N_2 Cryoplasmas"
Plasma Conference 2014, Niigata, Japan, November 18 – 21, 2014, 20pF-8.

2. °**H. Muneoka**, K. Urabe, S. Stauss, and K. Terashima
"Experimental and Numerical Investigation of the Dependency of Reaction Dynamics on the Plasma Gas Temperature in He/N_2 Cryoplasmas"
67th Gaseous Electronics Conference, Raleigh, NC, USA, November 3 – 7, 2014, MW1.00038.

3. °**H. Muneoka**, K. Urabe, S. Stauss, and K. Terashima
"Dependency of Reaction Dynamics on Plasma Gas Temperature in He/N_2 Cryoplasmas"
12th Asia Pacific Conference on Plasma Science and Technology and 27th Symposium on Plasma Science for Materials, Adelaide, Australia, August 31 – September 5, 2014, p.47.

4. °**H. Muneoka**, K. Urabe, S. Stauss, and K. Terashima
"Electric breakdown model for micrometer gap discharges in fluctuating fluids near the critical point"
The International Union of Materials Research Society – International Conference in Asia 2014, Fukuoka, Japan, August 24 - 29, 2014, D2-O26-011.
Award: "The Award for Encouragement of Research".

5. °K. Urabe, **H. Muneoka**, S. Stauss, and K. Terashima
"Production and Relaxation Processes of Metastable Helium Atoms in Cryoplasmas between 5 K and Room Temperature"
6th International Symposium on Advanced Plasma Science and its Applications for Nitrides and Nanomaterials and 7th International Conference on Plasma-Nano Technology & Science, Aichi, Japan, March 2 - 6, 2014, 03pB07O.
Award: "Best Presentation Award in Plasma Science".

6. °**H. Muneoka**, K. Urabe, J. H. Choi, S. Stauss, and K. Terashima,
"Characterization of helium cryoplasmas below 60 K with continuous gas temperature control"
8th International Conference on Reactive Plasmas and 31st Symposium on Plasma Processing, Fukuoka, Japan, February 4- 7, 2014, 6P-PM-S09-P20.
Award: "Young Scientist Award: Silver Award".

7. °**H. Muneoka**, K. Urabe, S. Stauss, and K. Terashima
"Electrical Breakdown Characteristics in Fluctuating Fluids near Gas-liquid Critical Point of Helium"
The 66th Gaseous Electronic Conference, Princeton, NJ, USA, September 30- Octobar 4, 2013, ET2 1.

8. °**H. Muneoka**, K. Urabe, S. Stauss, and K. Terashima
"Electrical discharges in a fluctuating helium fluid near the critical point"
The 12th Asia Pacific Physics Conference, Makuhari, Japan, July 14-19, 2013, Abstract p. 80.

9. **H. Muneoka**, K. Urabe, °S. Stauss, and K. Terashima
"Microplasma breakdown voltages in helium in the vicinity of the critical point"
The 7th international Workshop on Microplasmas (IWM-7th), Beijing, China, May 20-23, 2013, Abstract p. 36.

10. **H. Muneoka**, °S. Stauss, N. Ebato, and K. Terashima
"Gas-temperature-dependent self-organized pattern formation in helium dielectric barrier discharge cryo-microplasmas"
The 7th International Workshop on Microplasmas (IWM-7th), Beijing, China, May 20-23, 2013, Abst p. 64.

11. °**H. Muneoka**, J. H. Choi, and K. Terashima
"Characteristics of cryoplasma below boiling temperature of N_2"
63rd Annual Gaseous Electronics Conference and 7th International Conference on Reactive Plasmas, Paris, France, October 4-8, 2010, DTP-229.

Domestic

1. °**H. Muneoka**, K. Urabe, S. Stauss, and K. Terashima
"Development of Electrical Discharge Model for High-pressure Gases and Supercritical Fluids Taking into Account Dependence of Density Fluctuation on Considered Volume"
62nd Japan Society of Applied Physics Spring Meeting, Hiratsuka, Japan, March 11-14, 2015, 14a-A28-4.
宗岡 均、占部 継一郎、シュタウス スヴェン、寺嶋 和夫
「高圧気体・超臨界流体中における密度揺らぎのスケール依存性を考慮した放電モデルの構築」
第 62 回応用物理学会春季学術講演会，平塚，日本, 3 月 11 日-14 日, 2015 年, 14a-A28-4.

2. °**H. Muneoka**, K. Urabe, S. Stauss, and K. Terashima
"Cryoplasma Chemistry in He/N_2 Gas below Temperature of Liquid Nitrogen (77 K)"
61st Japan Society of Applied Physics Spring Meeting, Sagamihara, Japan, March 17-20, 2014, 17p-F3-15.
宗岡 均、占部 継一郎、シュタウス スヴェン、寺嶋 和夫
「液体窒素温度(77 K)以下のヘリウム/窒素混合ガス中におけるクライオプラズマ反応機構」
第 61 回応用物理学会春季学術講演会，相模原，日本, 3 月 17 日-20 日, 2014 年, 17p-F3-15.

3. °**H. Muneoka**, K. Urabe, S. Stauss, and K. Terashima
"Breakdown behavior in helium fluids including in the vicinity of the critical point"
60th Japan Society of Applied Physics Spring Meeting, Sagamihara, Japan, March 27-30, 2013, 29a-B9-4.
宗岡 均、占部 継一郎、シュタウス スヴェン、寺嶋 和夫
「臨界点近傍を含むヘリウム流体中のプラズマ発生プロセス」
第 60 回応用物理学会春季学術講演会，相模原，日本, 3 月 27 日-30 日, 2013 年, 29a-B9-4.

4. °**H. Muneoka**, K. Urabe, S. Stauss, and K. Terashima
"Breakdown Characteristics of He Cryoplasmas Generated in High Density Conditions Including near the Critical Point"
30th Symposium on Plasma Processing, Hamamatsu, Japan, January 21-23, 2013, A2-02.
宗岡 均、占部 継一郎、シュタウス スヴェン、寺嶋 和夫
「超臨界流体を含む高圧環境下におけるクライオプラズマの発生プロセス」
第 30 回プラズマプロセシング研究会（SPP-30），浜松，日本, 1 月 21 日-23 日,2013 年, A2-02.

Seminars

1. °**H. Muneoka**, S. Stauss, and K. Terashima
"Cryoplasmas and plasmas in supercritical fluids: Generation, characteristics, and application for materials processing"
IBM T. J. Watson Research Laboratory, NY, USA, October 7, 2013.

2. °**H. Muneoka**, K. Urabe, S. Stauss, and K. Terashima
"Cryoplasmas and plasmas in supercritical fluids: Generation and characteristics"
Poitiers University, Poitiers, France, September 9, 2014.

3. °**H. Muneoka**, K. Urabe, S. Stauss, and K. Terashima
"Cryoplasmas: Generation, characteristics, and application for materials processing"
Ecole polytechnique fédérale de Lausanne, Neuchâtel, Switzerland, September 11, 2014.

3. Awards

1. "The Award for Encouragement of Research" in The International Union of Materials Research Society – International Conference in Asia 2014. (No. 4 in the list of international conferences)
2. "Best Presentation Award in Plasma Science" in 6th International Symposium on Advanced Plasma Science and its Applications for Nitrides and Nanomaterials and 7th International Conference on Plasma-Nano Technology & Science. (No. 5 in the list of international conferences)
3. "Young Scientist Award: Silver Award" in 8th International Conference on Reactive Plasmas and 31st Symposium on Plasma Processing. (No. 6 in the list of international conferences)

4. Grants

2013/04-present: Research Fellowship for Young Scientists, Japan Society for the Promotion of Science.